Study of Low Gain Avalanche Diodes for the phase-II Upgrade of ATLAS High-Granularity Timing Detector

By

Sajid Ali

Department of Physics

Quaid-i-Azam University Islamabad, Pakistan

(2018-2020)

A DISSERTATION SUBMITTED IN PARTIAL FULFILLMENT OF THE REQUIREMENTS FOR THE DEGREE OF MASTERS OF PHILOSOPHY IN PHYSICS

DECLARATION

I, Mr. **Sajid Ali** Reg: No. **02181813019**, student of M.Phil, under the supervision of Dr. Ashfaq Ahmad (NCP) in the subject of physics session 2018-20, hereby declare that the matter printed in the thesis titled **"Study of Low Gain Avalanche Diodes for the phase-II Upgrade of ATLAS High-Granularity Timing Detector"** is my review work and has not been printed, published or submitted as research work, thesis or publication in any form in any University, Research Institution etc. in Pakistan.

_____

Sajid Ali

Supervised by:

_____

Dr. Ashfaq Ahmad
National Center for Physics (NCP)
Quaid-i-Azam University Islamabad

Submitted through:

_____

Prof. Dr. Nawazish Ali Khan
Chairman
Department of Physics
Quaid-i-Azam University Islamabad

Abstract

The thesis reports the performance of the low gain avalanche sensors for High Granularity Timing detector (HGTD). HGTD, based on low gain avalanche detector technology, which has been proposed for the ATLAS Phase-II upgrade. Covering the pseudorapidity region between 2.4 and 4.0, with a timing resolution of 30 ps for minimum-ionizing particles, this device will significantly improve the performance in the forward region. High-precision timing greatly improves the track-to-vertex association, leading to a performance similar to that in the central region for both jet and lepton reconstruction, as well as the tagging of heavy-flavour jets. The sensors that we analyzed were made by Hamamatsu photonics (HPK) of different wafer sizes. We analyzed the sensors for the basics requirements of the HGTD like waveform amplitude, charge and time resolution. The data were collected during March-2019 test-beam campaign at DESY. We found that those sensors which were highly irradiated with proton and neutrons shows poor performance compare to un-irradiated and low flounced sensors.

Acknowledgments

All praise to Allah Almighty, for bestowing upon me some fraction of knowledge from His infinite treasures and giving me enough strength to complete my research. Also my deepest gratitude to all who offered me helping hand in accomplishing this task. However, some names deserve explicit acknowledgment.

I would like to offer my heartiest gratitude to **Prof. Dr. Nawazish Ali Khan**, chairman of Quaid-i-Azam University, Islamabad, for providing me the opportunity to carry out this research project at National Center for Physics (NCP), Islamabad.

With the deep sense of respect, I am very grateful to my supervisor **Dr. Ashfaq Ahmad**, Director of EHEP, NCP Islamabad, who has always been very kind to me, guided me and encouraged me. His amiable and friendly nature provided me a homey environment to accomplish this research. I found him ready to take pain for my work at any time and his words of encouragement and piece of advice made my efforts fruitful.

I want to thanks Academia Sinica group for the opportunity to work with you on ATLAS detector. It was a pleasure to get an understanding of how to study and how to study particle physics in an experimental way.

I express my deep gratitude and respect to my instructor **Prof. Dr. Wang Song-Ming** for his keen interest, strong motivation and constant encouragement during my research work. I am thankful for his great patience and useful suggestion apart from invaluable guidance to me.

I am sincerely thankful to and appreciate my senior my instructor and friend, **Mr. Shahzad Ali**. He has always been so supportive during the entire period of my master research work. Mr. Shahzad Ali has provided me with valuable discussions and advice. Without his help, I could not finish my work. He has spent enormous time for teaching me and discussing data analysis with me. It was a great experience to learn many new ideas from him and solve many problems with him. It has inspired and motivated me very much.

I am also thankful to my friends and seniors Mr. Zahoor Islam, Mr. Ammad

Muhammad and my junior Misbahul Din for their insights and words of encouragement have often inspired me and renewed my hopes for completing my research work.
In addition, I would like to thank my classmates and research fellow Mr. Muhammad Jamshid and Mr. Fawad Ali Khan, Mr. Hammad malik, Mr. Muhammad farooq, Mr. Shehreyar Malik, Mr. Asad Munir, Rabia mobeen, Mr. Imadullah Tariq, Mr. Amjad Ali, Mr. Najeeb Khan, Mr. Muhammad Tayyab (PKD), I could not enjoy my master student life without them.
There are still many more people I have to thank. I am grateful to all of those friends and colleagues who helped me finish my study.
Finally, I would like to thanks my family, especially my parents for giving me moral support. They always encouraged my study and their love made me overcome any difficulties so far. I could not focus on my study without their devotion.

Sajid Ali

Dedication to

My Father

"My father gave me the greatest gift anyone could give another person, he believed in me"
"My dad has given me the best gift anyone has ever given me. He gave me wings to fly".

My Mother

"Mother is the heartbeat in the home; and without her, there seems to be no heartthrob"
"Mother's love is peace. It need not be acquired, it need not be deserved".

My Brothers

There is no other love like the love for a brother, there is no other love like the love from a brother.

My Sister

Sisters help you find important things when you've lost them. Things like your smiles, your hopes, and your courage
A sister is a special type of angel on Earth who brings out your best qualities.
.

My friends Fawad Ali Khan and Muhammad Jamshid

Your life was a blessing, your memory was treasure, you are loved beyond words and missed beyond measure.

Contents

List of Figures

List of Tables

Chapter 1

Introduction

To study the standard model of particle physics, the Large Hadron Collider (LHC) which is the largest and the most powerful particle accelerator in the world performs the job. The standard model has up until today described alot about the physics that we are observing in the universe but also predicted some of it before it had been observed [10]. The elementary particles and interactions between them can be studied at particle accelerators. The LHC at European Organization for the Nuclear Research (CERN), Geneva is a huge and most energetic particle accelerator [11]. It tries to study the predictions of different theories in the particle physics and helps to answer some open questions in physics including elementary particles and interaction between them, Higgs bosons properties, structure of space and time, extra dimensions and dark matter [10]. The detection of elementary particle called Higgs boson in two independent detectors (ATLAS) and (CMS) led to a Nobel prize in physics in 2013 [12]. However, the standard model is not the superior theory because it does not include one of the four fundamental forces, the gravitational force and unexplained phenomena like dark matter.

To continue the research for physics beyond the standard model, the upgrade of LHC is needed for increasing rate of gathering more data [13]. This upgrade of the detector aims to increase its luminosity (4000 fb^{-1}) by factor of 10 to 35 that will provide a better chance to detect rare process.

Therefore High-Luminosity Large Hadron Collider (HL-LHC) is going to be reconstructed and will be operational in 2026. The luminosity which is associated to the number of collisions per unit time for the HL-LHC will increase in the particle detector. HL-LHC will gather more data faster when distinct bunches of particles are crossing through LHC. The luminosity could describe that how many collisions per unit time will occur an average per bunch crossing.

In every crossing bunch, the particles interact with each other and generate a large numbers of secondary particles which can be studied. When two bunches of particles are collide, two types of scattering take place. First one is hard scattering, when two bunches of particles collide in such a way that head on collision take place and a large numbers of secondary particle are created. Second one is soft scattering are those interactions that passes without collision, where pile-up comes when the readout of a particle detector includes information from more than one primary beam interaction, or it occurs when the detector measures objects that do not come from the Primary Vertex where the hard scattering, meaning having energy scales more than a few GeV, occurs. The pile-up are those multiple interactions or the interaction that we are not interested in. The HL-LHC is designed for the large numbers of particles interactions simultaneously means the luminosity of the detector will increase that is directly related to pile up [14].

At the time of upgrade of LHC to HL-LHC, the ATLAS detector is also needed to be upgrade for the precise measurement of particles detection. The soft interaction happens which spreads in both space and time as shown in Figure 1.1 The current sub-detectors collect data and give only spatial information. When the number of events are increased in HL-LHC, the presently working sub-detectors will not be able to separate all the events from each other.

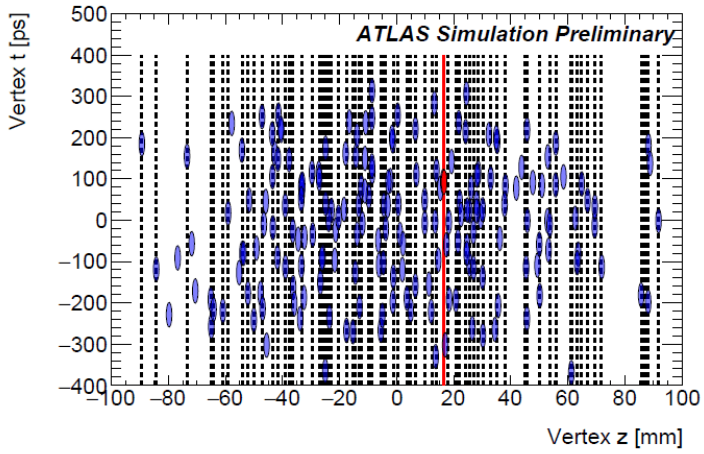

Figure 1.1: A simulation showing the spread of the collisions per bunch crossing in both spatial position and time, with one vertex of interest (in red) and approximately 200 pile-up reactions (in blue). The dotted line are the positions of the reconstructed vertices [1].

To solve such sort of problems, a new sub-detector the High-Granularity Timing Detector (HGTD) is going to be installed [1]. HGTD will offers a new and a powerful method to get overcome on pile-up interactions by picking benefits of the time spread of interaction. We can differentiate between those interactions that occurs very closed in space but will be spread in time. It will differentiate between the particles by timing information when particles are passing the detector at a very small angle from the original beam, known as the forward direction where the spatial resolution is worst. It will make easier to find the tracks created by particles inside ATLAS detector and will help to enhance the performance of detector by reduction the risk of assigning a particles tracks to wrong interaction vertex. The exact spread of interactions in time for the HL-LHC has not yet been determined but it will have a Gaussian spread of 175 ps up to 260 ps.

We need a sensor with a very good timing resolution for HGTD. The sensor technology which is going to be used for the ATLAS High Granularity Timing Detector that is recently developed and is based on silicon Low Gain Avalanche Detector (LGAD) have good time resolution of around 30 ps per

hit [15]. Because of high radiation environment inside the ATLAS detector it will be able to withstand radiation harm.

In this thesis we will use the data from HGTD test beam run in March 2019 for the performance of different types of LGAD's to determine their efficiency, gain, time resolution and radiation hardness [15]. Most studied LGADs consisted of a single pad, containing only one distinct area sensitive to charged particles with a size of the order of 1mm $\times$ 1mm. However, some sensors consisted of an array of two or more pads, each having a separate read-out to distinguish the pads. This thesis will focus on the properties in the inter-pad region, i.e. the region between pads, with three 2 $\times$ 1 pad arrangement from the test beams campaigns conducted in March 2019 at DESY. Efficiency and average charge collected by a traversing particle have been measured across the sensors using data from the test beams periods. These values were then used to acquire the minimum efficiency in the inter-pad region, and to determine inter-pad distances using several methods due to ambiguity. A thorough analysis of this kind had not yet been done on these sensors, but the results are critical for understanding the performance of the future HGTD since it will consist of arrays 15 $\times$ 30 pads [1]. The inter-pad region will, therefore, have a significant effect of the total detector time measurement efficiency which must be considered.

Chapter 2

Theoretical and Experimental Aspects of Particle Physics

This chapter begins with the brief overview of fundamental particles in nature and interactions between them through a short description of the standard model [2], followed by information about the LHC. As the understanding of the particle physics progresses with the discovery of the Higgs boson in 2012 [12], there are still unanswered questions. The standard model have several defects, for example it does not described the gravity or masses of neutrinos. Another problem with the standard model is that it represents only about 15% of the matter. Furthermore, if we look at the energy content of the universe, the standard model explains about 4%, the rest being dark matter(24%) and dark energy (72%). To further test the standard model and to look for the solutions to its problems, the ATLAS experiment and motivation of why HGTD is required. For this purpose, the detail information of HGTD and silicon LGAD sensors shall also discussed.

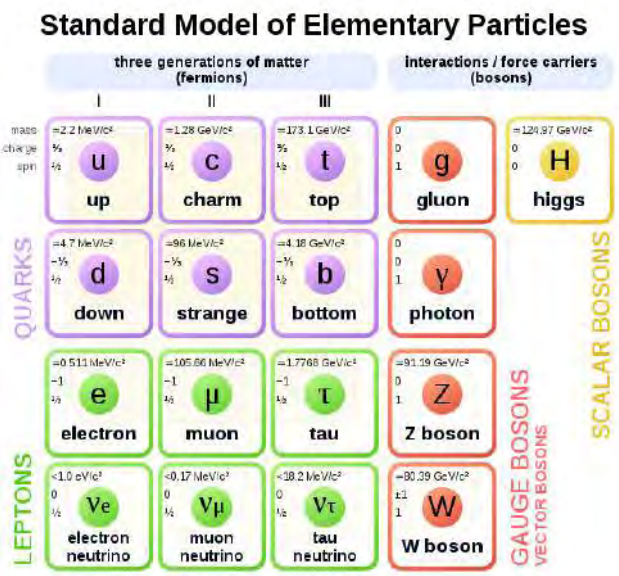

Figure 2.1: Elementary particles in standard model containing three generations of fermions, gauge bosons and on the top right corner Higgs Boson[2].

As Figure 2.1 shows the elementary particles in standard model can be divided into two groups; the fermions and bosons. All matter consists of fermions. The bosons are the force carriers. These are the particles that interact with each others and built up everything that now exits in our universe including stars and planets.

2.0.1 Fermions

The standard model of particle physics includes six types of quarks and leptons. Leptons and fermions are spin half particles and referred to as flavours called fermions. According to spin-statistical theorem, fermions obey Pauli's exclusion principle. Every fermion has an antiparticle with same mass but with opposite charge. The charges and masses of these elementary particles can be seen in Figure 2.1. Each fermion following three generations that differs from each other only by mass which is higher in each generation. The lightest flavours being in the first generation, these generations contains one up-type quark having positive charge, one down-type quark with negative charge, one charged lepton and a neutrino. If no law of conservation forbid

it, the heavier particles i.e, second and third generation particles will tend to decay to lighter one (first generation). Therefore, any stable material is generally composed of first generation particles; up quarks(u), down quarks(d), and electron(e). Just like particles can have electromagnetic charge, quarks also contain a color charges. Quark have color charge of red, green, and blue, only colorless combination may exist freely. A colorless particle could be created by the combination of three quarks. This colorless combination is called baryon, or a quark with anti-quark each with one of these color and anti-color called mesons. Baryons and mesons are combinedly called hadrons, for example protons and neutrons are include in the family of baryons which composed of quarks(uud) and (udd) quarks respectively. In mesons family pions are the lightest one containing a quark and an anti-quark. They cannot have an electrical charge ($u\bar{u}$,$d\bar{d}$), a negative charge($d\bar{u}$) or a positive charge($u\bar{d}$) [10].

Due to a phenomenon called color confinement, if a quark were to be created or force out from bound states, for example a proton in any collision, a shower of other particles containing color charges would also be created to form colorless particles. The new created particle could be studied to determine the properties of the original quark because they cannot be observed directly.

2.0.2 Bosons

The gauge bosons in standard model are the force carrier or force vectors and play a mediating role between the fundamental forces. The gauge bosons mediate three of the four fundamental forces namely, the electromagnetic force, weak force, and strong force. The mediators for the electromagnetic force which allows interactions between electrically charged particles are photons. It is through the electromagnetic force that light, electric field and magnetic field are exists. The weak force that acts on all fermions is responsible for changing flavour among the quarks and leptons. It is mediated by $W^{\pm}$ and Z boson. Strong force is responsible for the interaction between the color

charge particles and is mediated by gluons. These gluons binds together to form colorless particle just like hadrons. As gluons themselves carry a color charge, they can interact with each other [10]. The last boson discovered in the standard model is the Higgs boson. Higgs boson has no electric charge or color charge and is not at the origin of any fundamental force. Instead the Higgs bosons is manifestation of the Higgs field, that is responsible for giving it mass to other particles through the Brout-Englert-Higgs mechanism [16].

2.0.3 Physics Beyond the Standard Model

It is well known that the standard model is not a complete theory. Although this model has successfully explained and predicted many experimental observations. But one problem in this model is that it does not have any information about one of the four fundamental forces, the force of gravity or why it is so much weaker than the other three forces. Another problem with this model is the assumption that masses of neutrinos are zero, while the opposite result is presented by observations, either the standard model depict the reality that our universe is made up of more matter then anti-matter, and cosmological measurements point out that there is more mass in the universe then what can be seen directly, it means that an unknown type of matter exist, called dark matter. To explain all the physics in the universe experimentally, many new models have been proposed, but none have yet been confirmed experimentally. The research for evidence of new physics beyond the standard model that might lead us towards desired theory of everything, is still an ongoing process, especially at the Large Hadron Collider (LHC).

2.1 Experimental Background

A particle detector also known as a radiation detector, is a device used for tracking, detecting and identify ionizing particles. The aims of particle detectors is to measure momenta and observe identity of particles that penetrate through it after being produced in an event, it might be a collision that occurs in the detector resulting many particles that decay to many more particles

or a decay that occurs spontaneously. The collision point is the exact location in space where the events occur. In order to completely reconstruct an event, meaning to identify particles produced in collision, and reconstruct the paths they takes is required to measure masses and momenta of particles. Particles produced ordinarily travel in a straight line, but in the presence of magnetic fields charge particles change their primary straight line path to a curved path. The curvature of path gives us a hint about particles identity, as higher momentum particles have less curvature, and vice versa.

The ATLAS is considered from hermetic detectors [17], which are the modern large-scale detectors encompassing several tracking chambers and calorimeters that surround the interaction point completely. Modern type of particle detectors are comprised of number of sub-detectors that are used for distinct aims having different properties and design. To follow the path of particles tracking devices are used, and calorimeters are used to absorb and compute the energy of particles. The function of tracking device is to show tracks of charged particles as they pass and interact with desirable substances, as neutral particles have no charge so they are not effected by electric field or magnetic field and move in a straight line. Normally, tracking devices do not directly show us the particles paths in a visible way. They instead, record small electrical signals that particles produce as they travel, then a computer program translates the signals to recorded pattern of tracks. Calorimeters are used to measure energy of particles, that penetrate through it, it ordinarily entirely stops all particles that are coming from an event or absorbs most of its energy, as it forces particles to deposit all of its energy within the detector.

2.1.1 Accelerator

The accelerators were developed in the 1930s to provide energetic particles to look into the structure of atomic nucleus. They have been utilized for the investigation of many features of particle physics. Its function is to speed up and rise the energy of a beam of particles by producing electric fields

that accelerate particles, while the magnetic fields is used to focus them. An accelerator may be in the form of a ring (a circular accelerator), where beam of particles moves repeatedly around a loop, or in a straight line (a linear accelerator), where beam of particles moves from one end to the other end. At CERN their are different accelerators, connected together in chain to reach consecutively to higher energies. An accelerator move the charged particles, such as electrons, protons or other particles with a high speeds, approximately close to the speed of light. These particles are then smashed either onto a target or against other particles circulating in the opposite direction. At LHC protons and heavy lead ions are accelerated to collide. One might expect the LHC to require a large source of particles, but protons for beams in 27-kilometre ring come from a single bottle of hydrogen gas, replaced only twice per year to make sure that it is running at the correct pressure.

2.1.2 The Large Hadron Collider

The LHC is a huge and the most powerful particle accelerator in the world. It has contributed to many important results in particle physics throughout its active years since 2008 [11]. The Higgs boson is one of the recent important discovery of the LHC in 2012 [12]. The circular structure of the LHC contains two parallel beam pipes that are accelerating particles in opposite directions. With its 27 km in circumference, the accelerator has up until the end of 2018 been able to accelerate protons up to an energy of 6.5 TeV, corresponding to a velocity very near to the speed of light approximately (0.999 999 99 c) [13]. When collisions are desired, the paths of the two beams are brought together at interaction points located inside the four main detectors of the LHC, as shown in Figure 2.2, the energy of 13 TeV collisions create particles different from the original ones that were brought to collide, hopefully including some rare or even currently undiscovered particles. In LHC protons are the main particles that are used for the collision purpose. The protons are gathered into bunches of approximately one hundred billion protons, which typically leads to 30-40 separate collisions per bunch crossing [11]. This process is

done in every 25 ns. Some of these processes are hard scattering which are the events of our interest, but most interactions are in reality rather uninteresting so-called soft collisions.

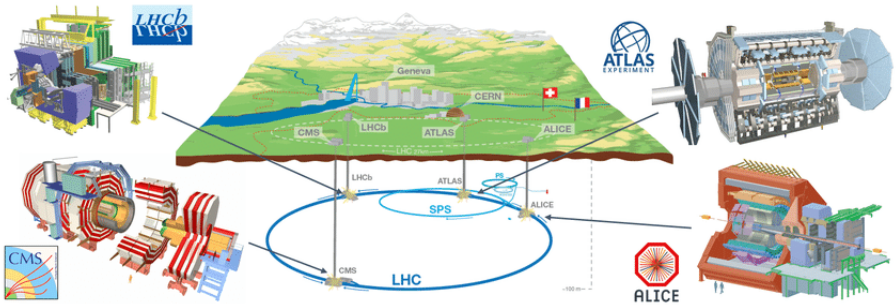

Figure 2.2: An illustration of the LHC and the locations of the four detectors. The smaller circular structure is the Super Proton Synchrotron (SPS) which is one of the pre-accelerators for the LHC [3].

For example, the Higgs bosons are the particles that are only produced in every ten billionth collision, and even then it is not always possible to detect it due to ambiguous decay modes since we can only be able to observed it indirectly through the particles it decayed into [18]. The performance of a particle accelerator can be described by the luminosity which is proportional to the number of collisions at a given time. In 2018, the instantaneous luminosity of the LHC often reached 2×10^{34} $cm^{-2}s^{-1}$ [19]. The term high luminosity implies more interactions, hence more hard scattering events (Head on Collisions), but also a larger number of pile-up. A typical value of collision density was an average of 0.24 collisions/mm due to the region of interaction having a spread of a few centimeters [19].

2.1.3 Accelerator complex chain

The Large Hadron Collider is final stair of the CERN accelerator chain, as presented in Figure 2.3. The initial proton are acquire by ionizing the hydrogen gas. This proton is then allowed to enter to Linac2 Detector, the length

of this accelerator is 30 m long and is a linear accelerator, this accelerator accelerate the proton up to 50 MeV energy. By going away from this accelerator, the proton moves toward the *PSB* (*Proton Synchrotron Booster*), a sequence of four superpose rings of synchrotron of the order of a 157cm circumference, which brought the protons up to 1.4 GeV energy.

This amount of rise in energy of protons permit for the improved shooting rate in next accelerator named the proton synchrotron (PS). This is lower limit (50 MeV) for the energy of the protons accept by the PS. It is a ring-shaped accelerator has circumference of 638 m. This will expand the protons energy of up to 25 GeV. After going away from PS accelerator the protons then inter to super proton synchrotron (SPS), this accelerator is 6 km long, before inject the proton into LHC it increase the protons energy up to 450 GeV. It not only provides protons for LHC, but for others experiments that are performed in the CERN like NA61, AWAKE, and NA62. An addition it supply particle to test the beam region used by the teams from the experiments LHC detector testing that will be used for the upgrades in future.

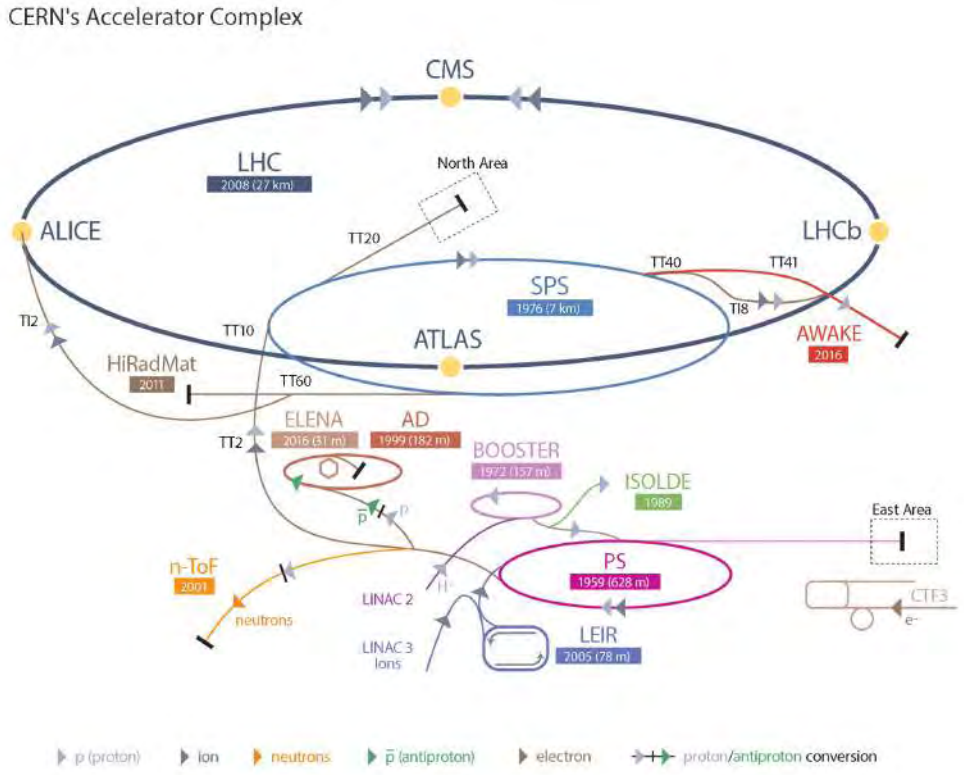

Figure 2.3: The sketch of LHC ring with the pre-accelerator components and four big experimental setup [4].

In the accelerator chain the protons are grouped into bunches with each bunch containing a large numbers of 1.15×10^{11} protons. All these bunches are separated by 25 ns the time period of collision. This whole process will roughly takes two hours to completely fill the LHC. The smaller accelerators of complex are required to fill up entirely several times to fill the LHC. As every bunch containing enormous amount of protons, the possibility of two protons interacting with one another throughout crossing bunch should be very high to notice more than one interaction per crossing bunch. That is known as the pile up, secondary collisions affair at the same time as one of regard. This influence the events restoration track in the detector.

2.1.4 Principle of the Accelerator

Like the other circular accelerator the Large Hadron Collider follow the same basic design, to keep particles in a circular orbit the magnetic fields help in circulating, and electric fields is used to accelerate particles on this orbit. The design of LHC is a bit more complicated than other classical particle-antiparticle colliders, because it collide protons with protons. LHC consists of two beam pipes in one pipe protons are moving in one side and another for protons in other side. To create the magnetic field in every ring, two-in-one of dipole magnets made of superconductive material are used. The operational temperature for these magnets is 1.9 K and it will generate 8.3 T of magnetic field. There are total of 1232 magnets are installed, each with size of 15 m long in LHC. Need for extra help to dipoles LHC is fitted out with 392 quadrupole. The purpose of using this is to focus the beam of protons before collision for increasing the resulting rate of interaction.

The magnetic set-up permits the movement of particles in circular path. To accelerate the particles an electric field is required. Which is supplied by the RF *Radio Frequency*, ACS *Accelerating System*, at LHC 16 cavities of such types are installed (8 for each ring). All these cavities are fitted out with wave-guide and klystron, to produce electric wave with frequency of 400 MHz the klystron are uses electron beams. Through the help of wave-guide this wave is then transferred to cavity, to accelerate protons. An accelerating voltage of approximately 2 MV with total of 16 MV per ring is created by every cavity. To reach the acceleration of proton from energy range 450 GeV to 6.5 TeV It takes roughly 20 minutes. For this accelerating network an energy in center of mass of the order of ps 13 TeV can be attain. Attaining a large center of mass energy of such order is very useful, bigger is this value the massive particles will be generated in collision, that qualify us to investigate higher energy range for detection or to constraint physics models.

2.2 The ATLAS experiment

To initialize collision at LHC, seven experiments have been performed. Every one of them focusing on disparate perspective of experimental particle physics:

- **ATLAS** [20]: ATLAS is a Toroidal LHC instrument. It is a general purpose experiments of physics programs measuring properties of the Higgs bosons, searches for new physics, which is used to investigate standard model of particle physics.

- **CMS** [21]: CMS *Compact Muon Solenoid* use for similar physics program like ATLAS detector, they are two indistinguishable experiments with non-identical technologies which make sure the repeatability of the calculation built by those two experiments.

- **LHCb** [22]: This experiment is used for precision measurements that carried out for the research of B-physics, such as CP violation.

- **ALICE** [23]: ALICE (A Large Ion Collider Experiment) is an experiment to study quark-gluon plasma that is generated in the heavy ions collisions.

- **LHCf** [24]: LHCf (Large Hadron Collider forward) is a special purpose experiment designed along the LHC main tunnel to study the origin of ultra high energetic cosmic rays.

- **TOTEM** [25]: TOTEM (TOTal Elastic and diffractive cross section Measurement) is also special purpose experiment lying on both sides of CMS designed to record the particles of small angles. The main goal of this experiment is to measure elastic scattering, cross-section and diffractive processes in p-p collisions at LHC.

- **MoEDAL** [26]: MoEDAL (Monopole and Exotics Detector at the LHC) is another special purpose experiment stationed on both sides

of the LHCb detector. It also records particles of low angles. The main purpose of this detector is to discover magnetic monopoles and additional long-lived exotic particle that may be generated in forward region.

The layout of LHC accelerator ring along with its all experiments is shown in Figure 2.4. Since the ATLAS detector is our main focus of research we will discuss it in more detail.

One of the major experiments at the Large Hadron Collider is ATLAS Experiment. Further descriptions and details about the detector can be found in the technical report[11]. The ATLAS detector consists of several subsystems and it is designed to detect the trajectories and energies of particles created after collisions.Different subsystems are surrounding the interaction point in varying barrel-like layers around the beam, as shown in Figure 2.4. These barrels mainly detect particles traveling at large angles with respect to beam. ATLAS also contains end-caps which detects particles traveling in the forward direction; with a small angle from the beam direction. To make the direction and position inside ATLAS easier to Apprehend, The beam direction is normally defined as the z-axis, with interaction point as the origin. The angle from z-axis is denoted by θ , but commonly, the direction is given in pseudo-rapidity (η). We define the η as,

$$\eta = -ln \tan(\theta/2) \tag{2.1}$$

large values of η therefore correspond to the forward region, and $\eta = 0$ corresponds to the direction perpendicular to the beam. The radial distance from the z-axis is denoted R.

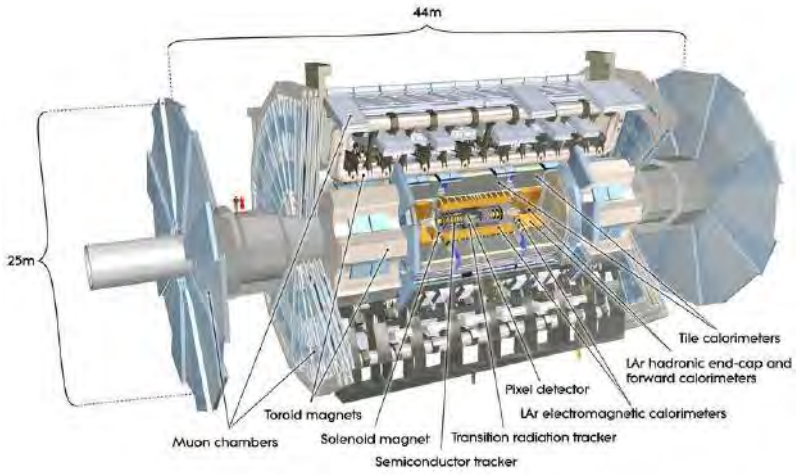

Figure 2.4: An overview of the ATLAS experiment [5].

We are only interesting in the region that are closest to the interaction point. It consists of the **Inner Detector** that tracks charged particles and measures their charge and momentum, the magnetic fields play very important role. The magnetic field makes the particles curve differently depending on their charges and momenta. The Inner Detector is necessary to know which vertex the particles came from; a vital component for later analysis of the interactions. Outside the Inner Detector, the **Electromagnetic Calorimeter** and **Hadronic Calorimeter** are located. They are built to stop and measure the total energy of particles.

As the names imply, the Electromagnetic Calorimeter mainly measures electrons, and photons, while Hadronic Calorimeter detect hadrons such as protons and neutrons. Muons and neutrinos are not stopped by the calorimeters, in fact, they are not stopped at all by the ATLAS experiment. The muons can however, be detected in the outermost detector; the Muon Spectrometer. The neutrinos go undetected, but their presence can be noticed as missing momentum when reconstructing the interactions.

2.2.1 The Inner Detector

The Inner Detector (ID) [27] Figure 2.5 is the first component of ATLAS detector that particles pass through it, it is very sensitive and compact. This tracks particles from LHC beam pipe to electromagnetic calorimeter system. The inner detector composes of three main components, the **Pixel Detector**, the **Semiconductor Tracker (SCT)** and the **Transition Radiation Tracker (TRT)**.

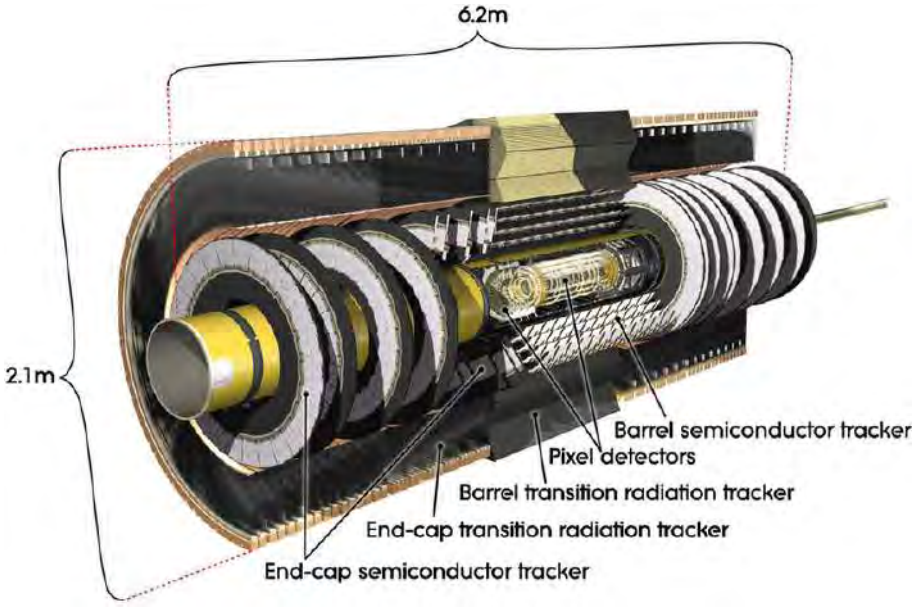

Figure 2.5: The Inner Detector of ATLAS Detector.

1. **Insertable B-Layer**
   The most central part of inner detector is the Insertable B-Layer (IBL) [28]. It was set up throughout primary long shutdown in the middle of run-1 and run-2 placed between the pixels detector. It is especially helpful for the events that contain B-hadrons whose tracks are believed to be originated from a secondary vertex because of their long decay time.

2. **Pixel Detector**: The pixel detector is the second detector of ID, which surrounds IBL and it is made of off three sub-layers of pixel detectors with containing additional discs positioned on both ends along the beam pipe which have an η-coverage less than 2.5. These layers of pixel detectors are located at different places sequentially 50.5 mm, 88.5 mm and 122.5 mm from the interaction point. The pixel detector is made of high granularity semiconductor materials. The sensors consist of anode and cathodes attached to a semiconductor materials. By passing charge particles through it creates a large numbers of electrons and holes that will travel towards anode/cathode. The current is then read out and signal is produced. It consists of four layers of pixel sensors. These four layers have 80 million pixels with a 50×400 μm. The most internal layer is placed at 3.5 cm away from the position of beam and the outermost one is at a radius of 12.5 cm. It has also 3 end-cap dics on every side with 6.6 million pixels. This part of the detector gives an output which corresponds to energy deposited in the detector by particles which passes through it, and gives us signal above the noise threshold.

3. **Semiconductor Tracker (SCT)**: The upcoming layer of the ID is Semiconductor Tracker (SCT). It utilizes the same silicon technology and works identically like the pixel detector but instead of silicon pixels it uses silicon strips. It also has forward disks and central region and provides η-coverage less than 2.5. The SCT consists four layers in the barrel region laying at 299 mm, 371 mm, 443 mm and 514 mm from the interaction point and 18 planar end-cap discs 9 on each side from interaction point. These silicon microstrips are place in cylindrical shape that covering pixel detector. The microstrip themselves are placed parallel to beam line pixed in barrel and in the end-caps they are directed radially. The semiconductor Tracker is the second closest sub-detector from beam line. It contain roughly 8 million channels and readout strips have a pitch of 80 μm with a length of 6 μm. Which

gives a positional measurement accuracy of 17 μm $\times$ 580 μm . This detector will register those hit that are above threshold value, below the threshold will not be considered.

4. **Transition Radiation Tracker (TRT)**: The third portion of inner detector is the Transition Radiation Tracker. The total module comprise 50000 tubes in the barrel and 25000 tubes along along the end-caps. The straws in the barrel are 144 cm long and the end-caps are on the other hand 39 cm long. The straw tubes are cylindrical in shape with a radius of 2 mm. Xenon gas mixture are filled and have gold plated tungsten wires of radius 0.3 mm that are placed in the centre. When charged particles are allowed to pass through the gases it gets ionized. Due to this positive and negative charge electric field is produced with in the straw, the free electrons will move towards the wire in the centre.

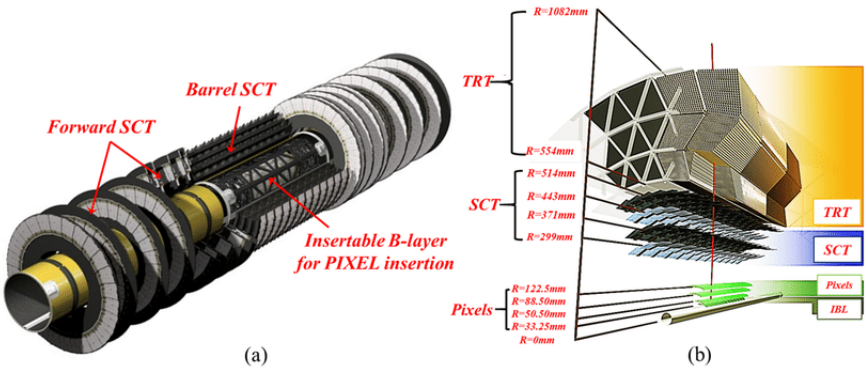

Figure 2.6: The figure showing the detector elements accrossed by a charged particle with 10 GeV pT in the barrel of the Inner Detector. The particle emerges from the interaction point and passes the beam-pipe, three pixel layers, four double layers of SCT.

As the electron move with high speed towards the centre they will accelerate so they will produced an avalanche effect and will free more

and more electrons. These free electrons will then create signal inside the wire and these signal will be readout. The straw are covered by the plastic material, that is used to induced the transition radiation. The amount of the transition radiation is proportional to the lorents boost factor (mF), so this will make able the detector able to separate the hadrons that are heavier from the electrons due to the mass differences. A view of Insertable B-Layer, pixel detector, Semiconductor tracker and Transition Radiation Tracker as shown in Figure 2.6

2.2.2 The Calorimeters

These are specialized detectors situated around the ID. The main function of calorimeters is to compute energy of particles that are losses when particles are passing through the detector. Its coverage goes up to $|\eta|< 2.5$. Basically the calorimeters are design in such a way that it will entire or "absorb" most of the particles that are coming from collision, forcing particles to deposit all of their energy within the detector. The calorimeter system of ATLAS is composed of three types of calorimeters.

1. **Electromagnetic Calorimeters** : The ATLAS electromagnetic calorimeters or (ECAL) [29] are composed of one barrel and two end-cap parts. An active material liquid argon(LAr) and lead absorber materials are used in it. The lead is used in an accordion shape, that is symmetric around the z axis, and the liquid argon is filled in between the gaps. The Figure 2.7 shows the EM barrel calorimeter, displaying three layers with differing cell granularities. The selection of the liquid argon(LAr) is an active material is for the motivation of linearity, stability and its ability to withstand high radiation doses.

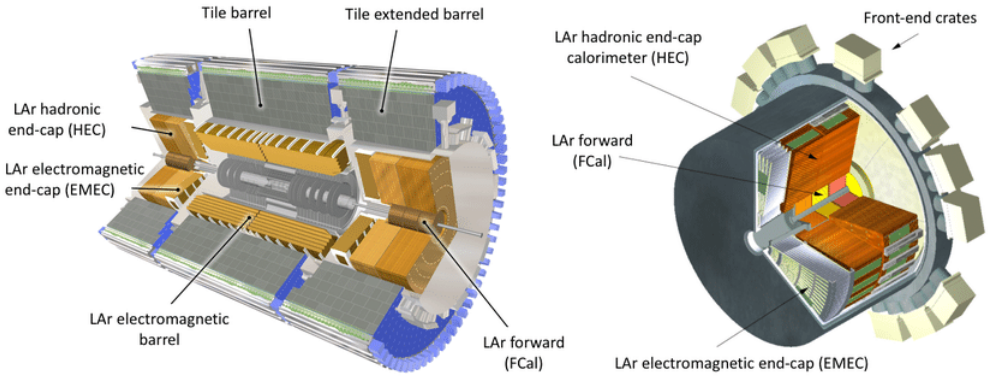

Figure 2.7: The Drawing showing the subsystems of the ATLAS calorimeter (left) and an enlarged view of the end-cap calorimeters (right).

2. **Hadronic Calorimeters** : The hadronic calorimeters [30] consists of tile central barrel, the Tile extended barrel and the hadronic LAr end caps. The Hadronic calorimeter is situated outside the Electromagnetic Calorimeters. In the Tile calorimeters the iron is used an absorber material and the plastic scintillators is used as an active materials. They are paramount to ensure proper identification and measurement of hadronic jets. The Tile Calorimeters are fitted with photo multiplier tubes to measure the light that are emitted from the scintillators. The hadronic LAr end caps are similar to the LAr electromagnetic end caps but has copper as an absorber material. Hadronic calorimeters is shown in Figure 2.8.

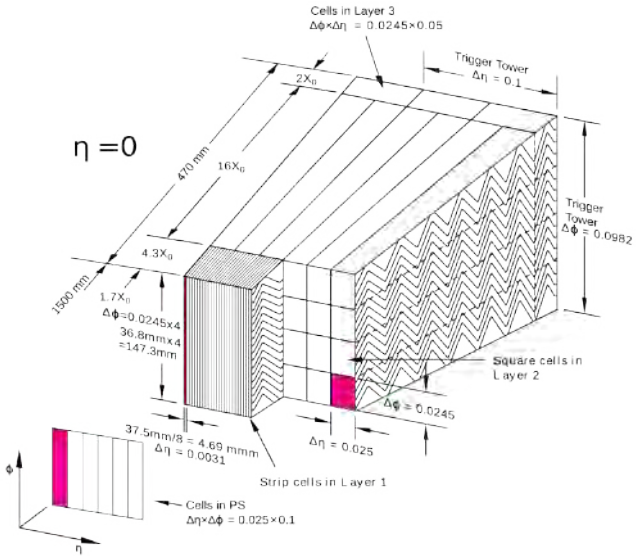

Figure 2.8: The ATLAS Hadronic Calorimeters.

3. **The forward calorimeter** : As the name indicate that it work in the forward covering region of $3.1<|\eta|<4.9$, and is LAr based forward calorimeter. It lie of 3 layers per end cap. The first one is made of copper, that is used to optimize for the electromagnetic showers. And the rest of two are made of tungsten, that are design for the hadronic showers. The face of the detector is located at 1.2 m at out side with respect to the end cap front face electromagnetic calorimeter, that is to reduce the neutron reflective power in the cavity of the inner detector. This limits the depth of the detector and it is therefore has a high-density design. The forward calorimeter depth amounts to approximately 10 interaction lengths.

4. **The Muon Spectrometer** : Just after the calorimeter only neutrinos and muons are left because they cannot be detected by the calorimeter. The neutrinos are not detected in the ATLAS detector as they interact by weak interaction. They are not detected directly, so their energy is estimated by calculating the missing transverse energy. Therefore the muons are detected in last layer of the detector so called **Muon Spectrometer** [31]. There are three spectrometer so called stations

each of these can reconstruct track from the passing particles. There is a toroidal magnetic system on both end-cap and and barrel parts, with each contains eight coils. These are able to measure the momentum by bending the trajectory of the traversing muon. A Monitor Drift Tubes (MDT) are used for $|\eta|<2.0$. It consist of an Ar-based gas which gets ionized when the muons pass through it. When an electric field is applied, the electron gets freed and accelerates to the centre of the tube towards a thin anode wire which generates a signals.

In the region $2.0<|\eta|<2.7$ Cathode Strip Chambers(CSC) are installed instead of MDTs due to the larger particle per unit area(Flux). These are also based on the same gas filled with a configuration of multiple wires. Furthermore detectors used to trigger the recording of data are installed. In the barrel region, The Resistive Plate Chambers(RPCs) are located at $|\eta|<1.05$ and in end-caps at $1.05<|\eta|<2.4$ the Thin Gap Chambers (TGCs). The RPCs are the gaseous system which gets ionized by passing muons, on the other hands the TGCs use a multi-wire technology which is adapted for the high flux for high η-Range.

5. **The Superconducting magnets** : It has given the name Barrel Toroid, Both the Central Solenoid and The End-Cap Toroids combine together with the ATLAS magnetic power system [32], that is used to controls and refrigeration plant to form the magnetic system of the ATLAS Detector, as shown in Figure 2.9. The property of the magnetic system is to provides the bending power for the charged particles paths, the particles with no charges will not be effected by the magnetic system. This will be able in making the tracks of the particles and measuring their momentum.

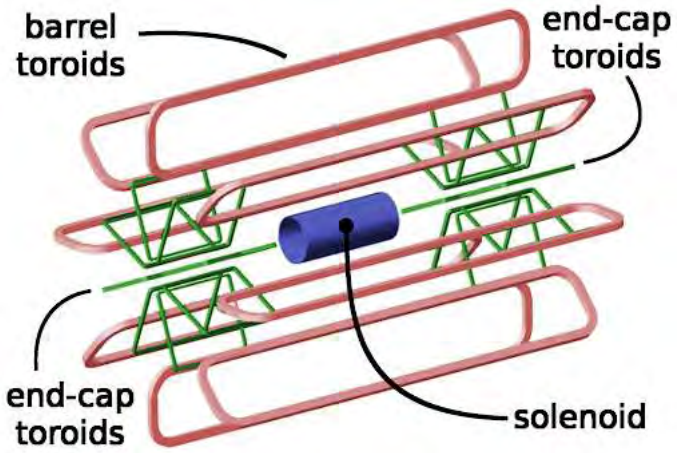

Figure 2.9: A sketch of the ATLAS magnet system with the central solenoid and the three toroids. Image: CERN

Chapter 3

Detector up-gradation for High Luminosity LHC

3.1 The HL-LHC Upgrades

The Large Hadron Collider (LHC) started fully operating in 2010, at that time it has delivered an integrated luminosity of approximately 190 fb^{-1}. About 30 fb^{-1} was recorded at center of mass energy of 7 TeV and 8 TeV was during the start of run-1. During run-2, the integrated luminosity of 160 fb^{-1} was recorded at center of mass energy of 13 TeV [33]. To gathered enough data to reduce the statistical error to that level that will give more precise measurement of rare events and to a level that could significantly increase the chances for discovering something new [7]. This is one of the reasons why the LHC was shut down at the end of the year 2018: Now the struggle for the High-Luminosity Large Hadron Collider (HL-LHC) installation that will be going to take place after run-3, in 2021-2024. It is the LHC phase-II program [6], planned to be operational in 2026. The planning of the upgrade for the LHC is presented in Figure 3.1 It will be able to deliver an integrated luminosity of up to 4000fb^{-1} . The HL-LHC will attain an instantaneous luminosity of up to 7.5 $\times$ $10^{34}cm^{-2}s^{-1}$, corresponding to pile-up of 200 proton-proton interactions on average $<\mu>$ = 200, where the $<\mu>$ is the poisson distribution define as it describing the number of interaction per

bunch crossing.

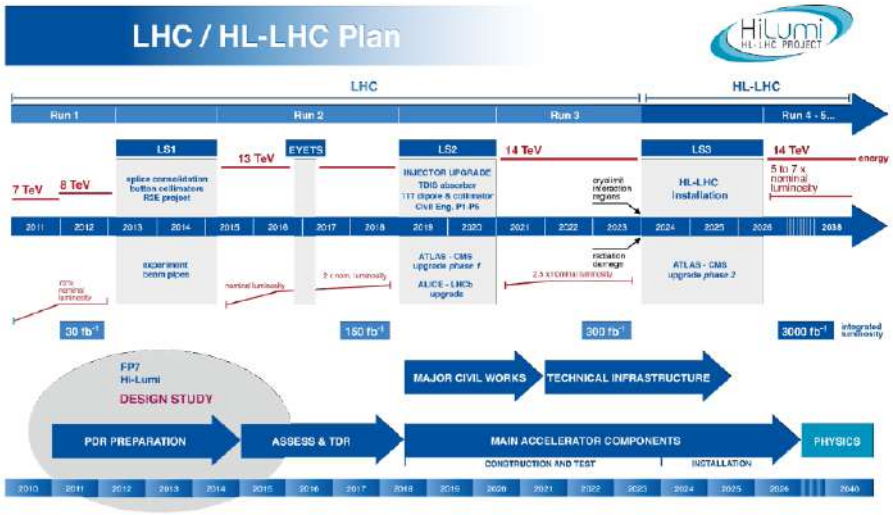

Figure 3.1: LHC up-gradation plane towards the HL-LHC [6].

This is possible only to improve the probability of forcing the beam that collision will occur. The gaussian spread of the point of interaction that is expected 30-60mm along the z-axis [1]. With a spread of 45 mm, will correspond to probably 1.8 collisions/mm on average. This is then equated with the instantaneous luminosity $2 \times 10^{34}\text{cm}^{-2}\text{s}^{-1}$ and the collision density 0.24 collision/mm from before the shutdown. Our mission is to increase luminosity for gathering more data faster, for observing rare events like Higgs bosons can also be studied in detail. Moreover, a try to run the LHC at energy 14 TeV will make it possible for the creation of those particles that need this amount of energies.

3.1.1 LHC upgrades

To get an integrated luminosity of 4×10^3 fb^{-1} and center of mass energy of 14 TeV, LHC requires that some of its feature should be upgraded that is its

various subsystems will essentially be put back to hold out against the high radiation dose to which they will be exposed. This up-gradation involves replacement of the systems with new better performant tools instead of spare ones.

The key difference between the LHC and HL-LHC parameters are the rising in protons number in every bunch and decreasing of bunch size. The development of these two parameters together lead to increase of density of proton in each bunch, which increases instantaneous luminosity as a result of bunch crossing. This improvement in particles density could be attained by replacing magnets. The quadrupole magnets that are positioned on each side of both CMS and ATLAS used for squeezing of proton bunches before the collision to reached the desire instantaneous luminosity [34]. The installation of new magnets will be based on Nb_3Sn technology that will be able to produce magnetic field up to 12 T, which will squeeze the proton bunches radially. This will result to improve instantaneous luminosity.

Later the upgrade of HL-LHC instantaneous luminosity will reach up to $7.5\times10^{34}\text{cm}^{-2}\text{s}^{-1}$ and center of mass energy of 14 TeV. It will result the a pile-up of up to $<\mu> = 200$. For the ATLAS detector to work under these situations, necessarily needs to be up-graded in order to withstand both the large radiation dose which results in increasing number of particles hitting detector and huge pile-up which further complicates the reconstruction of objects. The beam variables before and after the up-gradation are shown in the Figure 3.2.

Parameters	Nominal LHC	HL-LHC
n, number of particles per bunch [10^{11}]	1.15	2.2
N_b, number of bunches per beam	2808	2748
f, revolution frequency of the bunches [kHz]	11.25	11.25
F, luminosity reduction factor without (with) crab-cavity	0.836(0.981)	0.369(0.715)
$\sigma_{(x/y)}$, number of bunches per beam[μm]	16.7	8.2
$\mathcal{L}$, pic luminosity without (with) crab-cavity $10^{34} cm^{-2} s^{-1}$	1.00(1.18)	6.52(12.6)

Figure 3.2: The LHC and HL-LHC relevant beam parameters. [7].

3.2 Upgrades of ATLAS for the HL-LHC

The main motivation of ATLAS detector upgradation is to keep performance at least as acceptable to the one acquired at LHC, and if feasible to enhance them. The ATLAS detector will also undergo several upgrades to face the challenges of high luminosity phase. In new condition of HL-LHC pile-up will be one of the main challenges. In the nominal operation scheme, the interaction region will have a gaussian spread of 45 mm along the beam axis and a pile-up of 200 simultaneous pp interactions on average ($<\mu> = 200$), corresponding to an average interaction density of 1.8 collisions/mm as seen in Figure 3.3 (Left). The major challenges for the tracking detectors is to efficiently reconstruct charged particles created in primary interactions and correctly assign them to vertices. This requires the resolution of longitudinal track impact parameter z_0, provided by the Inner Tracker (ITk), to be much smaller than the inverse of the average pile-up density (0.6 mm). The z_0 resolution is well below this limit in the central region, but becomes very large in the forward region, reaching up to 5 mm for particles with low transverse momenta (p_T) as shown in Figure 3.3 (Right). As a result, tracks cannot be associated to the correct vertices in an unambiguous way, leading to reduced performance in terms of heavy-flavour tagging, lepton isolation and the identification of jets originating from pile-up interactions.

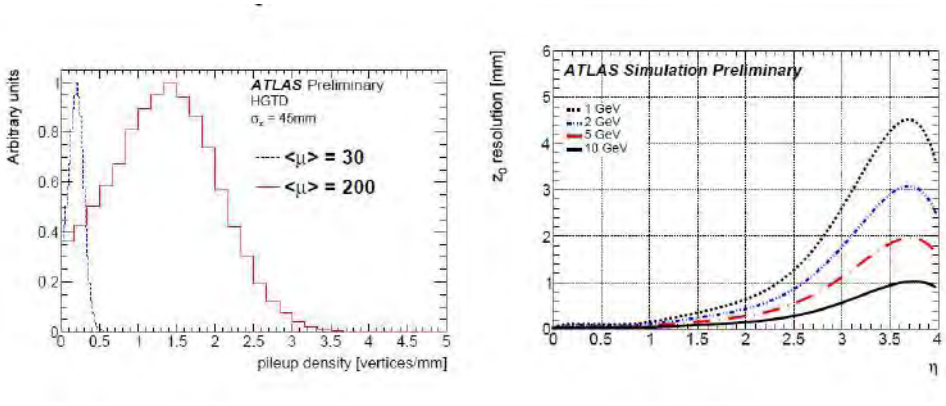

Figure 3.3: Left: Current and HL-LHC local pile-up vertex density. Right: The resolution of longitudinal track impact parameter, z_0, as a function of η for different pT values [1].

The replacement of old inner detector by a new one is the ATLAS major up-grade project. Inner Tracker (ITk) that reach the end of their life-time. The old electronic Liquid Argon (LAr) calorimeter will be replaced by a new one and the trigger system will be improved. Eventually, to reduce the pile-up interaction and improve the performance of ATLAS in forward region, an additional timing detector called High Granularity Timing Detector (HGTD), for HL-LHC Phase-II [6] up-gradation is being designed in the detector forward region.

3.2.1 ATLAS Inner Tracker

Due to high radiations level and increasing numbers of pile-up at HL-LHC the ID will be not functioning. The ID will be replaced by the Inner Tracker (ITK) and silicon detector made of both strips and pixels as shown in Figure 3.4. Due to acceptable radiation resistance of this material an all silicon pattern was chosen. It is very close to beam-pipe to the inner layer of ITk the fluence (the number of particles per area) in this area will be extraordinarily large. To keep up the performance good a replacement of modules after 2 $\times 10^3$ fb^{-1} is predicted. An enormous number of particles passing trough the detector due to larger pile-up, and thus a enormous number of hits in the trackers. The ID which has a pseudo-rapidity coverage of up to $|\eta|<$

2.5, the updated ITK will provide pseudo-rapidity coverage of up to $|\eta|<4$. This upgrade coverage reaches the one from the calorimeters, which will show superior reconstruction of forward objects as they may be reconstructed utilizing a combination of calorimeter bunches and tracks. The Internal part of ITk [6] will consist of 50 μm $\times$ 50 μm (or 25 μm $\times$ 100 μm) silicons pixels. This sub-detector is made up of five layers in the barrel region and a series of disks in the end-caps regions and provide a pseudo-rapidity coverage of up to $|\eta|<4$. As a result of its high granularity, it will allow for a better primary vertex reconstruction position of the order of 200 μm in the barrel region for low P_T tracks.

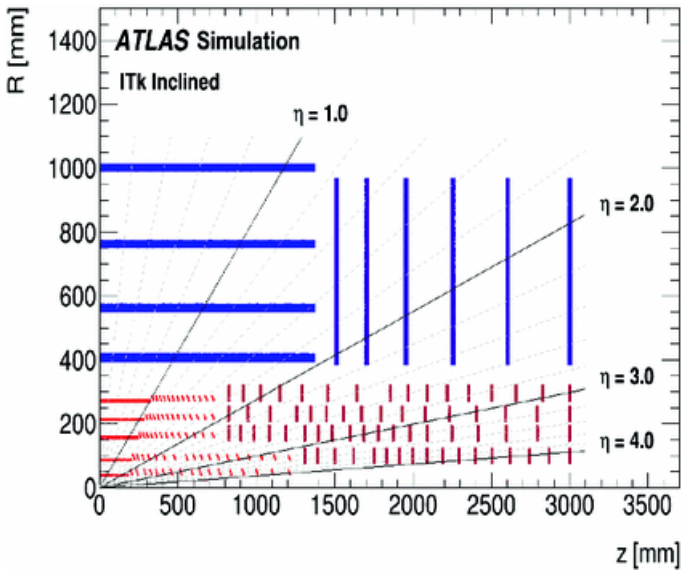

Figure 3.4: Diagram of the foreseen all-silicon Inner Tracker (ITk) upgrade of the ATLAS Inner Detector, due to be installed in the phase II upgrade [8].

The strip detector will be installed on every side of the pixel detector [6], which is consist of four layers in the barrel of silicon strip detector and six petal shape disks on both end-caps to supply a coverage up to $|\eta| = 2.7$. It is made of two type of silicon strips with a pitch of 75.5 μ m and a length of either 24.10 mm or 48.20 mm that depend on the local occupancy. The

strips are radially distributed on stave in the barrel and petal in the end-caps and provide a fine radial resolution. To sustain some resolution in other direction the modules are tilted with a little stereo angle. The design of both the pixel detector has been improved to give total of at least 13 hits for $|\eta|<2.6$. This should permit the ITk to record a better performance in the barrel region than the ID during run-2, while providing a coverage with allowable performance up to $|\eta|=2.6$.

3.3 High-Granularity Timing Detector

As a result of high luminosity in HL-LHC a new detector named the High Granularity Timing Detector (HGTD) [35] will help to decrease the negative effect of pile-up. As the collision in bunches do not happen at exactly the same time, there is a time difference between them. By measuring the time of particle tracks will help to separate all the interactions so we can solve the problems due to pile-up interactions. The HGTD will be able to determine that from the numbers of collision vertices are located at the same spot, if they came from separate collisions. Because of high luminosity in HL-LHC the number of collisions will increase highly so the tracking mission will get complicated due to large numbers of pile-up. Pile-up are those interactions that when the readout of particle detector can have information that are from the secondary beam interactions, or detector measure those objects that are not coming from the Primary Vertex, where the hard scattering , it meaning that with energy scale more than a few GeV occurs. Pile-up events are uninteresting interactions and having very low energy which can be calculated by simulations

There are two types of pile-up interaction, **In-time pile-up** these are those interaction that are coming from the same protons bunch from the interaction of interest, it could be solved by sitting the location of the points of interaction by identifying vertices, by measuring their distances and comparing with the primary vertex. The second one is the **out-time pile-Up** this is coming from the other proton bunches when detector not yet recorded

signal completely due to dead time, the time which is required for a sealed detector that is able to record an event after the previous one or some other reasons, that could be dictated by silicon detector because they have a time resolution equal to the time per-bunch crossing, 25 ns.

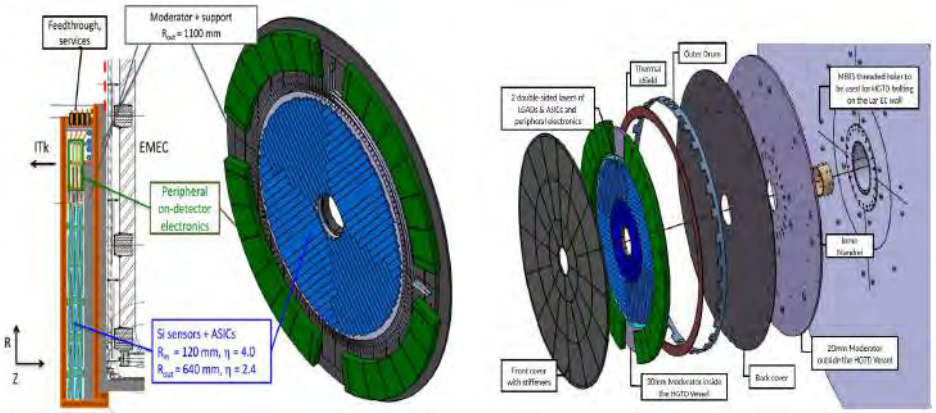

(a) (b)

Figure 3.5: An Assembly of the HGTD design. The blue structure indicate the active area and the green structure indicate electronics. The darker area in the active region is designed to yield a larger number of hits [1].

The suppression of the detectors signals is one of the hard challenges in high luminosity upgrade of LHC program that is caused by the additional low energy proton-proton collisions that are the pile-up, which are produced by a nominal average of $\mu = 200$ per-25 ns per crossing bunch. That is why the ATLAS is Offering a HGTD. Aside from the improved track-to-vertex performance, the HGTD could also be used as a luminometer. Although there are apparatuses measuring the luminosity at HL-LHC but for the precision purpose it also works. HGTD will help in reducing the uncertainty in the integrated luminosity. As the cross section of defined reaction that occurs is directly proportional to probability, so it is useful in determining the cross section for some rare processes like the cross section of Higgs bosons. The project of HGTD is patterned to run for a total integrated luminosity of 4000 fb^{-1}, it will measure the time when charge particles passing through

detector with time resolution of approximately 25 ps at start of the lifetime at the end with time resolution of 50 ps.

The mechanical design of HGTD has consist of two separate dicks that is placed between the Inner Tracker (ITK) and ATLAS end-cap calorimeters at forward direction at z = ± 3.5 m with an active area of 120 mm <R<640 mm and cover the region 2.4<|η|<4. The total thickness of detector will be 75 mm with active area. But an extra disk of moderated material of thickness 50 mm will be inserted between the end-cap and calorimeter of the HGTD. The purpose of this is to protect the HGTD and Inner Tracker from back-scattering neutrons which increase life time of the detector [1]. There are two cooling disks inside the main vessel of each end-cap. On both sides of cooling disks narrow rectangular staves are placed with sensor modules. The disks with staves are designed along R for measurement of passing particles with an average three hits at R<320 mm and two at R > 320mm. This could be achieved by placing the modules with overlap between the front and the back of each cooling disk. The mechanical design of the HGTD is shown in Figure 3.5 and its main parameters can be found in Table 4.2 .

The sensor technology which is used for the detector will be consist of **Low Gain Avalanche Detector (LGAD)** sensors which is silicon based of size 1.3 mm^2 × 1.3 mm^2 wiht active thickness of 50 μm . The over all thickness of the LGAD will be approximately 300 μm. Total 15 × 30 pads will be contained in each sensor with total size of 20 × 40mm^2 [1]. Larger or smaller the pads size was defined through the trade-off between the advantages and disadvantages. Smaller pads surface yield lower electronic noise and reduces the risk of having more than one hit which is important for acquiring accurate timing information.

Basically LGAD sensors have been optimized for timing measurements and fulfil the requirement of time resolution and requirement of surviving in an environment from the huge amount of radiations for ATLAS detector. The time resolution of the detector decreases as a function of integrated luminosity [36]. The fluence (the number of particles per area) decreases exponen-

Pseudo-rapidity coverage	$3.1 < \|\eta\| < 4.0$
Thickness in z	75mm (+ 50mm moderator)
Position of active layers in z	z = ± 3.5m
Radial extension:	
Total	$110\text{mm} < r < 1000\text{mm}$
Active area	$120\text{mm} < r < 640\text{mm}$
Pad size	1.3 mm × 1.3 mm
Active area	$120\text{mm} < r < 640\text{mm}$
Active sensor thickness	50 μm
Number of channels	3.59 M
Active area	6.4m^2
Average number of hits per track	
$2.4 < \|\eta\| < 3.1$	≈ 2
$3.1 < \|\eta\| < 4.0$	≈ 3
Collected charge	> 2.5 fC
Average time resolution per hit (start and end of operational lifetime)	
$2.4 < \|\eta\| < 3.1$	≈ 40 ps (start) ≈ 70 ps (end)
$3.1 < \|\eta\| < 4.0$	≈ 40 ps (start) ≈ 85 ps (end)
Average time resolution per track (start and end of operational lifetime)	≈ 30 ps (start) ≈ 50 ps (end)

Table 3.1: The main design parameters of the HGTD [1].

tially with radius, hence the part closest to the beam-line will be exposed to more radiations. It is therefore proposed that the sensors and electronics up to $R = 320$ mm are replaced halfway through the HL-LHC program. Due to high radiation levels expected in this region, and more challenging time resolution requirements that we had discussed, the HGTD will made of 4 layers (planes) of silicon in each end-cap, made of LGAD pads with an active thickness of about 50 μm and with pad area of 1.3 mm × 1.3 mm. The Sensor size is determined by requirements of $< 10\%$ occupancy. The minimum dead areas and the capacitance. That effects time resolution. Moreover one important compliment is to minimize numbers of detector types from the cost and complexity point of view.

3.4 The Low Gain Avalanche Detector (LGAD)

The sensor technology uses for the HGTD are LGAD, with low energy requirement they give a moderate multiplication (gain) on the collected charge, that will direct to a significant improvement in time resolution and signal to noise ratio. It is a kind of silicon radiation detectors widely used in collider experiments, they are based on PIN diodes. It consists of a layer of an n-type semiconductor on a p-type semiconductor with an additional layer of extra highly Boron p-doped silicon [1]. It operating with external reverse bias, it means that work on negative voltage, in full depletion region. The p-type of semiconductors are the elements of group third from the periodic table contains acceptors with excessive amount of holes and low number of electrons, while an n-type semiconductor (group five elements of modern periodic table) contains donors with excessive electrons in the outer most shell of the atom, by combining these two materials together p-n junction is created at the boundary due to diffusion of electrons and holes. The holes on the p-side travel towards n-side where it is eliminated by electrons and vice versa. This will create a negative charge on p-side of p-n junction.

Due to this an opposite charge is appear on both side of the p-n junction which creates an electric field across so called depletion region or depletion layer. This potential barrier suppress diffusion of more holes and electrons until an equilibrium is attained. So the depletion layer will allow the electrical current to flow in uni-direction across the p-n junction [37].

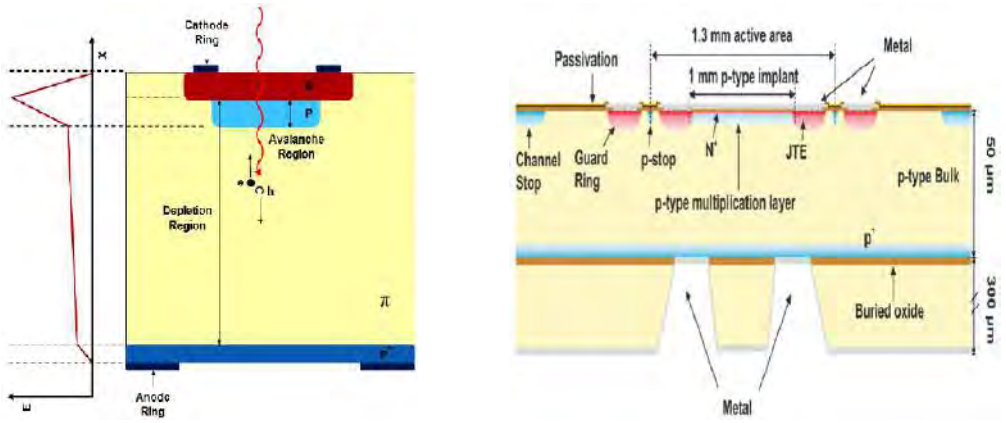

(a) (b)

Figure 3.6: A cross section of an LGAD sensor showing the directions that the electrons and holes created by a traversing charged particle (red arrow) travel. The strength of the electric field (E) across the sensor can be seen to the left [1, 9].

By the application of an external voltage over the diodes of depletion region will be increased thus making the potential barrier larger. When a charged particle passes through depletion region of the sensor, it will interrupt equilibrium and creates pairs of electrons and holes which produce small current. A cathode is connected to n-doped an anode is connected to p-doped sides, that measure the current produced. There are two ways to assemble LGAD **single pad LGA** or **2 × 2 pad array**. The sensor LGA with single pad has an overall active area of 1.3 × 1.3 mm^2.
Here we are discussing about single pad array. The important things which LGAD makes different from the other silicon detectors is highly boron doped p-type layer also called avalanche region which is located below the p-n junction as shown in the Figure 3.6. This is the region which creates a large electric field and causes internal gain which amplify signals while the noise remains low. When charges moves towards cathode and they will reach highly p-doped region and increase its acceleration. Due to high electric field fast moving electrons knock out other electrons which creates more electron-holes pairs. The electrons and holes move towards terminals and current will increase which is proportional to height of the signals [38]. The amount of

gain is dependent on the doping concentration of silicon detector and the radiation dose. LGAD sensor for the ATLAS HGTD have been designed to have a gain of around 20.

3.4.1 LGAD Performances

The time resolution of LGAD sensors from distinct manufacture have been studied extensively in many test-beam setup and lab setup, the results of HPK sensors are shown in Figure 3.7 . It has been shown that the time resolution for every single sensor before irradiation which is lower than 30 ps. This resolution can be attained with bias voltage lower than the breakdown voltage. The principal difference between the two sensor comes from their thickness, the thickness of one sensor is 30 μm while the other is 50 μm thick.

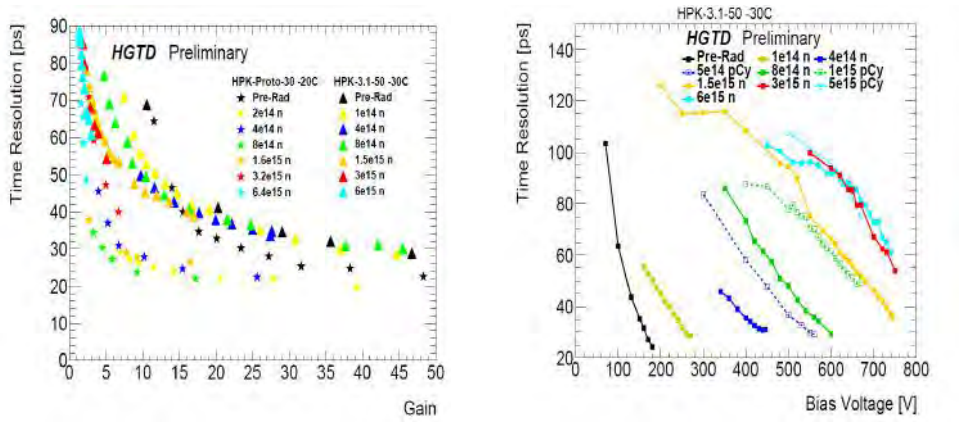

(a) (b)

Figure 3.7: Time resolution σ_t as a function of gain of 2 irradiated HPK sensors (LGADs) of 50 and 30 μm width when time walk correction is applied. Figure (b) σ_t of 2 HPK sensors which is function of bias voltage at a given temperature of -30 C.

In silicon the radiation destruction mainly results in change of effective doping concentration, the establishment of trapping centers that decrease the mean free path of charge carrier, and the leakage current will be increased. The fluence within HGTD at the end of HL-LHC will be changing from 6×10^{15} $n_{eq}cm^{-2}$ at low radius down to 1×10^{15} $n_{eq}cm^{-2}$ at large radius. This

limit greatly depend upon the quantity of material in front of HGTD. The main effect for LGAD is the loss of the effective doping concentration in the multiple layers due to deactivation of primary boron as acceptors, which leads to increase time resolution [39] due to decrease in gain. For fluence (the number of particles per area) greater than 1×10^{15} $n_{eq}cm^{-2}$, there is small differentiation between LGAD and simple PIN diode. Luckily, at this high fluence a gain has been detected for both devices PIN and LGAD, since effective acceptors produced by irradiation combine with breakdown voltage higher lead to high electric fields sufficient for charge multiplication in the full sensor. Which can be shown in Figure 3.7 (b), the maximum bias voltage achievable increases as increasing the fluence. By increasing bias voltage on the sensor at greater fluence the timing resolution can thus be sustained.

3.5 HGTD Electronics

The major character of the electronic is to magnify and shape the pulse and take out the applicable information from the pulse, digitize the instruction and then send it through the flex cable toward the peripheral on detector electronics situated at 700mm < R < 900mm. The ASIC also required to be able to hold signal with a huge dynamic scale from 1 to 20 MIP. Using simulation of the electronics shower within HGTD this scale was determined.

3.5.1 From pulse to time

There are different steps needed to determine a time from a pulse. The first one is the output signals go through the preamplifier, the main aim of the preamplifier is to further enhancing the amplitude of the pulse compared to the jitter and thus reduce (σ_{jitter}) as much as possible. These signals then go through a discriminator that will coming back a changeless output as long as the signal is above a certain threshold. This output is then transport to two Time to Digital Converter (TDC), one for estimating the Time Over Threshold (TOT) and one for Time of Arrival (TOA). The TDC work on two input, one begin and one end,the starting input is delayed compare to the

stop one by increase of 20 ps, the number of signal delayed need for the stop signal to be ahead of the start is then multiply by 20 ps, this will correlate with the time between the initial and the end, that valve is then outputted as a digital signal. For the calculation of the TOA the initial signal that correlate with discriminator signal and stop to the end of the measurement window, with this plan there will no start signal will be received by the TDC if no hit was measure, that will reduce the power waste of the ASIC. A wide range of the order of 20 ns TOT is used, in this situation the start signal will also compared to the discriminator output but the stop will this time correlate with the moment when the discriminator output return to 0.

3.5.2 Why we need low gain ?

A silicon devices with high gain like SiPM and APD are pattern to have the ability to detect single (SiPM) or a few (APD) photons, respectively, and they require high gain to do such sort of tasks. Although there are many drawbacks of high value of gain. Means the increasing in the sensor noise, the problems in the sensor segmentation, and the utilization for high power after irradiation. Instead of photons the detection of charged particles has the advantage of initial signal much larger, because in one micron 73 electron-hole pairs (MPV) are generated by a minimum ionizing particle (MIP), allowing the use of lower gains, the LGAD technology is therefore the solution to the problems caused by high gain. Leakage current for silicon detectors used in high radiation environments creates shot noise and heat, and it can be the determining factor in the selection of the optimum gain value for such applications, even when cooling the sensor sharply. For the low-noise, low-power operation required in a tracker system for a high-energy physics experiment, a gain of approximately of 20 might be an optimum choice for the functioning of LGADs.

3.5.3 Why is the selection of thin sensors ?

The current signal produced by a minimum ionization particle (MIP) in LGAD has a rather strange shape: it has a rise time that is as long as

the drift time of an electron passing the entire thickness of the sensor, and its maximum current uniquely depends on the gain value. For these two actuality, assuming a fixed value of gain, the signal steepness depends on the sensor width: thin sensors have a much faster rising edge, sometimes called "slew-rate", which in turn improves the time resolution. Sensors that are very thin, however, have large values of capacitance and require high gain to create signals that are large enough to be measured accurately by the read-out electronics: both these facts are detrimental for time resolution. The sensors therefore need to be thin, but not too thin: this delicate balance is explained in the following sections. Experimental results and simulations indicate that a thickness of 50 micron combined with a gain of approximately of 20 provides optimum performance.

3.5.4 Time resolution

The time resolution of a LGAD is mostly determined by Landau fluctuation (σ_{Landau}) and the electronic noise (σ_{elec}) [35] and defined as the accuracy of measuring the time at which particles are detected. The Landau fluctuation is caused by the variation in the energy or the deposition of energy non-uniformly when high energy particles interact with the sensor. Its contribution depends on the sensor thickness (for thinner sensor there will be less fluctuation) and the setting of the threshold [40]. And the effect due to electronic noise are inversely proportional to the slope of the signals dV/dt which is dependent on sensors gain [15]. Landau fluctuation and the electronic noise are determined by two effects: the jitter (σ_{jitter}), and the time walk ($\sigma_{timewalk}$). We can reduces the effect of the landau fluctuations by using thin sensors, that is why we are going to use thin sensor of size 50 μm for the HGTD with corresponding time resolution of approximately of 30 ps. Three important effects determine the time resolution: jitter from electronic noise, time walk from amplitude variations, and "Landau fluctuation" from the non uniformly charge deposition along the particle path. Both jitter and time walk are caused by uncertainties in reading of the time when the signal crosses a threshold. The terms noise jitter and time walk depend on the type

of readout electronics chosen, they are shown in Figure 3.8

The term *time walk* means the variation in the reconstructed time which is a function of energy when a fixed threshold is used. It can normally be made good up to a large extent using time reconstruction algorithms such as constant-fraction discrimination (CFD), time-over-threshold (ToT) or amplitude corrections. CFD is a method used in measurements assuring excellent time resolution. It depends on width and fitting of the Gaussian. The term *time jitter* refers to the variation caused by the noise of the amplitude. For sufficiently large noise it results the signal to pass the threshold too early or too late yielding in incorrect reconstructed time. It can be extenuated by a superior signal-to-noise ratio. Both these effects inversely depend on the slope of the signal that is, dV/dt.

$$\sigma_{jitter} = \frac{N}{dV/dt} = \frac{t_{rise}}{(S/N)} \tag{3.1}$$

$$\sigma_{timewalk} = \left[\frac{V_{th}}{S/t_{rise}}\right]_{RMS} \propto \left[\frac{N}{dV/dt}\right]_{RMS} \tag{3.2}$$

N : Represents an Electronic noise amplitude.
t$_{rise}$: Rise time of signal.
S : Signal amplitude.
V$_{th}$: Threshold voltage to determine time of arrival of signal.
RMS: Stand for root mean square value.

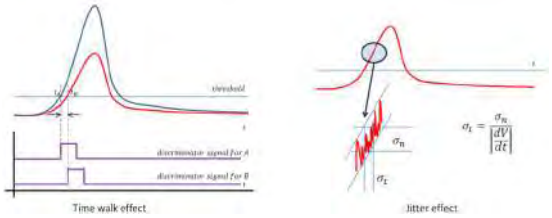

Figure 3.8: Effect of the time walk (left) and jitter (right) on the reconstruction of the time.

There are two more terms in this equation that are depending upon the size of the time-to-digital converter (TDC), and preciseness of the clock distribution, By using oscilloscope instead of time-to-digital converter (TDC) so the rest of the effect will not be considered. The total time resolution of an LGAD due to major effects are given by

$$\sigma_t^2 = \sigma_{Landau}^2 + \sigma_{jitter}^2 + \sigma_{timewalk}^2 \tag{3.3}$$

A larger gain will therefore afford a better time resolution, but there is a limit where the Landau fluctuations becomes dominant. The sensors of the given size will corresponds to a gain of approximately 20. The time resolution of LGAD sensors will get bad if the sensors have been irradiated, due to decreasing of gain. The reason of this is the changing in the effective doping concentration in the avalanche region. The decrease of effective doping will continue with more fluence until the avalanche region does not make a difference. The HGTD is planned to be built using sensors with a time resolution of 40 ps for minimum ionizing particles (MIPs) at the beginning of its lifetime. MIPs are those particles whose energy loss rates when interacting with matter are close to minimum. The particles which are produced at LHC called Relativistic particles in practice can be treated as MIPs when passing through the detectors.

3.5.5 Time walk correction

The electronics time resolution should be lower than one of the LGAD. The contribution of the electronics to the time resolution is given by :

$$\sigma^2_{elec} = \sigma^2_{jitter} + \sigma^2_{TW} + \sigma^2_{TDC} \tag{3.4}$$

The σ_{TDC} effect is due to the TDC that is the converters times to digital information. A quantization with a fixed binning is used for this conversion, it is needed that the size must be smaller than the timing resolution. Bins of size 20 pico second are used due to this, for which the contribution to the time resolution is to be of the order of 5 pico second and hence be negligible contrast to the sensor resolution. Each separate channel's time offset should be calibrated accordingly. In order to reduce the effect caused by the time walk, there exist some methods used to enable the measurement to be insensitive to the pulse pulseheight. A constant fraction discriminator could be used by the first one instead of a fixed threshold, using this method the threshold is termed as "a fraction of maximal amplitude of the pulse". Since the pulse shape is independent of its amplitude, it means that measure time will not depend on the pulse height.

For HGTD ASIC, the second technique comprises a correction application of the TOA time which is based on TOT. As the dispersion of the time walk is related to the pulse height, if someone can measure that pulse height then the time can be measured correctly. In silicon detectors the most usual way to do this correction is to measure the width of the pulse instead of directly measuring the pulse amplitude. Thus two TDCs are required one of which for the TOA and the other for TOT instead of TDC for the TOA and ADC (Analog to Digital Converter) for the amplitude. TOA is provided by the measurement of the rising edge of the discriminator pulse where as the TOT is provided by the falling edge combined with the TOT.

After the time walk correction using TOT the remainder σ_{TDC} lower than 10 ps can be obtained. The larger the amplitude of the pulse the greater is the value of TOT. In this range use for the TOT calculation, the value of TOT could become more than 20 *ns* for high energy strikes. For the TOA correction, its saturation is the only information in that case. Fortunately for actually greater signal height the dependence of time walk with the signal height decreases. The correction applied for TOT 20 *ns* can thus also be applied to those events to rectify the time walk partially.

Chapter 4

Test-beam setup for LGAD Sensor

There are two test-beam setup one is at CERN SPS north area to test the LGAD sensors for HGTD. But due to long shut down of CERN from 2019 to 2020 figure 3.1, in order to obtain information on how the LGAD sensors will perform in the HGTD, they should be tested in conditions similar to environment that they will be used in. This is done by using pulse beam of 5 GeV electrons to test the devices. This thesis will mainly focus on experimental setup of test-beam campaigns in March-2019 at DESY [41], but the setup was mostly same for all of test-beam periods.

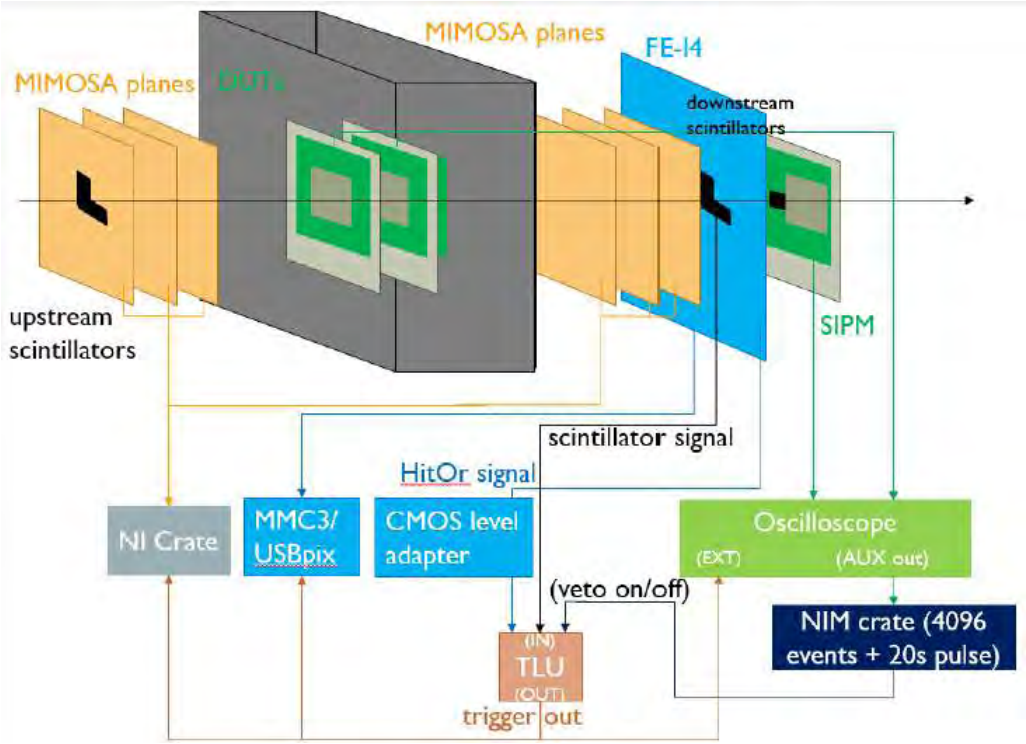

Figure 4.1: A simplified image of setup used for test-beam measurements. More than one oscilloscope is used to increase the number of simultaneously tested sensors.

There are two main parts of test-beam setup: the Device Under the Test (DUT) and telescope. The diagram of test-beam setup is shown in Figure 4.2 . The setup used for testing is a telescope consisting of six aluminium-housed sensors put perpendicular to the beam. These telescope sensors are of the Mimosa25 type. The first three sensors DUTs were connected to same 4-channel of oscilloscope. After first three mimosa planes, the beam reaches to silicon photomultiplier (SiPM) and LGAD sensors. The last channel was reserved for SiPM used as a time reference due to its time resolution being better than for the LGADs; in the order of 10 ps. The SiPM and LGADs sensors were located after each other along the beam line, and its active area is perpendicular to the beam for the purpose to pass the beam to all of its components.

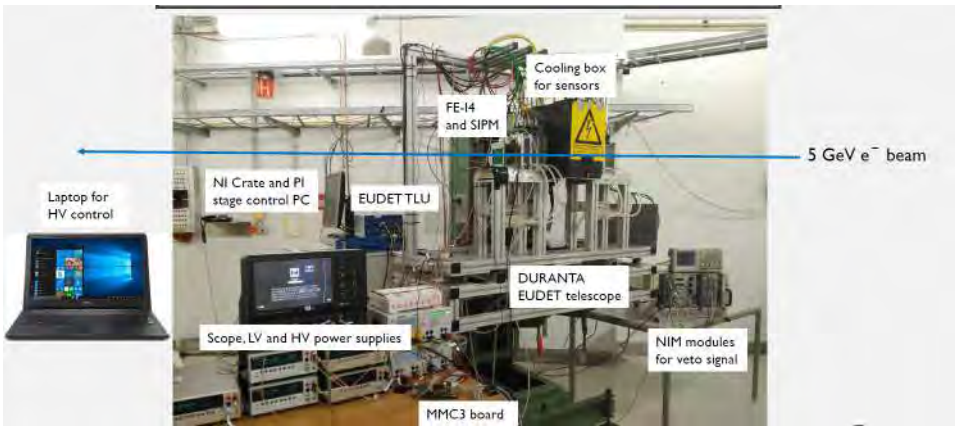

Figure 4.2: The DESY test-beam setup in March-2019.

There were two oscilloscopes used for the test-beam campaigns that allowing the data taking for up to six DUTs at same time. The SiPMs and DUTs were then placed in a styrofoam box. The purpose of the styrofoam box is to help keep a stable temperature around the sensors and to shielding the SiPMs from light. All these setup can be seen in the Figure 4.2 . Moreover the telescope is placed upstream and downstream the sensors measuring the positions of the particles where it hit the DUTs, making it possible to evaluate the behaviour of LGADs across the different regions of the sensors. A separate triggering system make sure that only relevant traversing particles were saved as an event.

4.1 Device Under Test

The DUTs in set up are several LGAD sensors. All these sensors that we will study in this thesis are un-irradiated and irradiated single-padded arrays created by Hamamatsu Photonics (HPK) for the test-beam March-2019. Each pad was connected to their own oscilloscope channel to differentiate which one pad had been hit. Details about the sensors including the temperatures and bias voltage values that were tested can be found in Table 4.2.

4.2 Silicon Photomultiplier

The LGAD sensors are not equipped with any time reference system. Therefore a SiPM is needed in order to get time resolution of the tested LGADs. The SiPMs have a known time resolution of < 15 ps and work as a reference sensors for the LGADs [42]. It has an active size 3×3 mm^2 and are single cell mounted on small boards. The sensors are tied on baseboards with amplifiers and enclosed in 3D printed boxes.

4.3 Telescope

Tracking of particles was the main purpose of telescope, and making sure to obtain spatial information about where the particles hit sensors region. It is therefore called EUDET-type beam telescope consisting of six MIMOSA pixel planes and pixel with size of 18.5μm $\times$ 18.5 μm [40]. Three of the planes were placed in front of DUTs with a small separation in between the planes, and three of these planes were placed behind it. By finding location of all MIMOSA planes and internal coordinates of where particles hit them, using fit procedure tracks could be reconstructed. With the distances to the DUTs, method of interpolation was used to determine the coordinates on LGADs where particles passing.

4.4 Front End-14 Plane

A scintillator and a very fast pixel detector called Front End-14 (FE-14) plane use is a reference planes were placed among the telescope to act as a triggering system and to define region of interest (ROI). The FE-14 has a pixel size of 50 μm in the horizontal direction, and 250 μm in the vertical direction, and with a time window of 25 ns. The scintillator and the FE-I4 were connected to a Trigger Logic Unit (TLU), to yield a signal only when a particle hit both scintillator and FE-I4. These trigger signals were used to trigger read-out of both the telescopes and oscilloscopes. A mask of pix-

els with ROI was defined on the FE-I4 to make sure that it only triggered for particles travelling through area of the SiPMs and DUTs. The read-out window of MIMOSA planes of 112.5 μs is quite large and given the particle rate of the SPS, this usually produces a number of tracks during that period of time. Thanks to its very short time window of 25 ns, FE-I4 can also be used to determine which of the tracks observed by telescope that fired trigger.

4.4.1 Data files

The data is grouped into runs which is defined as the collection of consecutive events that are collected with out break from the data acquisition programs. The destination is to, under the course of multiple runs, collected approximately one million events with the same temperature of cooling box including the LGAD sensors and a particular voltage for each sensor. Every combination of these run with same sitting is called batch. Whole data from the test-beam collected are saved and divided into two types depending on if the data comes from the oscilloscope or telescope. Here we will discuss these two types briefly.

Unprocessed oscilloscope data are saved as data-unixtime.dat, where the unix time refers to the time when recording starts, ensuring unique names to all files. Every data files is followed by a meta text file containing information about the data file. The meta-files have not been intensively used. Root is the extension used in CERN's scientific software toolkit ROOT [40]. The root files compiled in this manner will hereafter be referred to as ntuple files. Each produced file includes information from one specific test beam session and one batch. Not every tested batch has been converted. A short descriptions of variables with names in the processed ROOT files in the ntuple data are shown in Table 4.1.

By using another externally written program it is possible to extract every individual event for each sensor saved in the ntuple file. This is critical for the auto-triggering analysis. It make able the possibility to examine if an event contains more than one voltage point large enough to be classified as a

Variable name	**Description**
pulseHeight	The amplitude of the highest peak
timeCFD	Time reconstruction with a Constan Fraction Discriminator
timeCTD	Time reconstruction with a Constant Threshold Discriminator
timeAtMax	Time at which amplitude is maximum
pedestal	Mean of the measured voltage
noise	Standard deviation of the voltage
charge	Integral of the pulse divided by the transimpedence
jitter	N/(dV/dt)
pulseHeightNoise	Max amplitude computed using only the Ist two ns of samples

Table 4.1: A short descriptions of variables with names in the processed ROOT files in the ntuple data.

trigger. In original file only the largest voltage peak for each event is being recorded. This data include information on the single event, will be referred to as the waveform data. The other type of data file is telescope files. These files including the hits on the Mimosa planes and the FE-14 chip in the telescope configuration by the beam. Since neither Mimosa planes nor the FE-14 chip is positioned exactly upon the LGADs, the tracks of the hits need to be reconstructed in order to get anything useful for the LGAD analysis. The optimization of the position and track fitting is done externally. The peak of this distribution can be fitted using a Gaussian function. The time resolution of the LGAD sensor is finally calculated by measuring the width of the Gaussian function. A more narrow distribution indicates a better time resolution.

Sensor	**Fluence**	**Bias** Voltage(V)	**Temperature** (°C)	**Batch**	**Ch**
HPK3.1SE5IP3J1	un-irradiated	100	-20	101	1
		120	-20	102	
		150	-20	103	
		200	-20	104	
		200	-20	105	
HPK3.1SE5IP3J3	un-irradiated	100	-20	101	2
		120	-20	102	
		150	-20	103	
		200	-20	104	
		200	-20	105	
HPK3.1W8P2LGE5	8e14n	390	-37.7 ∼ -35.9	601	1
		450	-35.9 ∼ -34.3	602	
		500	-41.1 ∼ -34.3	603	
		530	-40.8 ∼ -38.2	604	
		560	-32.6 ∼ 35.7	605	
HPK3.2W18P4LGE5	8e14n	250	-37.7 ∼ -35.9	601	2
		300	-35.9 ∼ -34.3	602	
		320	-41.1 ∼ -34.3	603	
		350	-40.8 ∼ -38.2	604	
		390	-32.6 ∼ 35.7	605	
HPK3.1W82×2SE5IP3	1.5e15n	390	-30.9 ∼ -27.6	701	1,2
		530	-31.7 ∼ -28	702	
		570	-35.5 ∼ -32	703	
		600	-34.9 ∼ -32.7	704	
		650	-34.3 ∼ -33.4	705	
HPK3.1W8LGE5	1e15p	550	-48 ∼ -45.9	1101	1
		570	-46.7 ∼ -45	1102	
		600	-44.6 ∼ -42.5	1103	
		650	-38.6 ∼ -32	1104	
		700	-37.4 ∼ -34.1	1105	
HPK3.1W8LGE2	3e15n	530	-47.3 ∼ -45.5	1201	1
		570	-45.7 ∼ -42.2	1202	
		600	-41.8 ∼ -39.3	1203	
		650	-38.1 ∼ -31	1204	
		700	-38.2 ∼ -38	1205	
HPK3.2W18LGE500	3e15n	530	-47.3 ∼ -45.5	1201	2
		570	-45.7 ∼ -42.2	1202	
		600	-41.8 ∼ -39.3	1203	
		650	-38.1 ∼ -31	1204	
		700	-38.2 ∼ -38	1205	

Table 4.2: The Sensors tested in March-2019 test-beam at DESY for the HGTD.

Chapter 5

Analysis and Results

This chapter explains the analysis results for HPK sensors using test-beam data taken during March-2019 at DESY. The result is shown for the studies of un-irradiated sensors HPK3.1SE5IP3J1 and HPK3.1SE5IP3J3 followed by irradiated sensors, with different fluences. Some properties of these sensors such as charge collected by the sensors, pulseheight (amplitude), noise, signal to noise ratio and time resolution are studied. Table 4.2 describe the names of sensors utilized in different batches with different fluences, bias voltage and temperature. All the results and graphs that are produced using the codes built by ATLAS-HGTD team and PyAna and have been extracted using ROOT/CERN.

5.1 Collected Charges for Un-irradiated Sensors

The un-irradiated sensors are studied for batch 101 to batch 105 at channel 1 and channel 2 respectively at temperature -20^{0}C. From the plots shown in Figure 5.1 have two peaks in the charge distribution for the sensors. The peak located around zero is the contribution from the background noise. This noise resulted by the events when the beam does not hit the sensor active area. The second peak is located approximately around the 30 fC is the signal from the sensor, when the beam of particles hit the sensor. It is important

to perform a precise analysis we need to remove the background which will be discuss section 5.6. Figure 5.1 shows charge distribution for batch 101. Plots for the other batches are shown in Appendix A for the un-irradiated sensors.

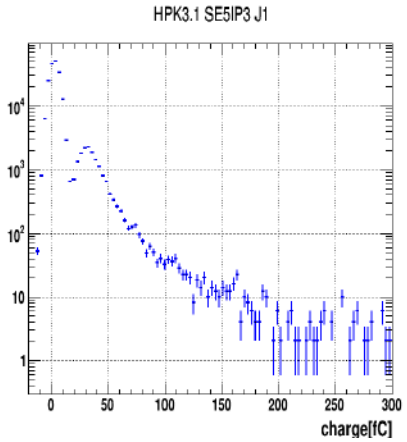

(a) Charge collected by HPK3.1SE5IP3J1

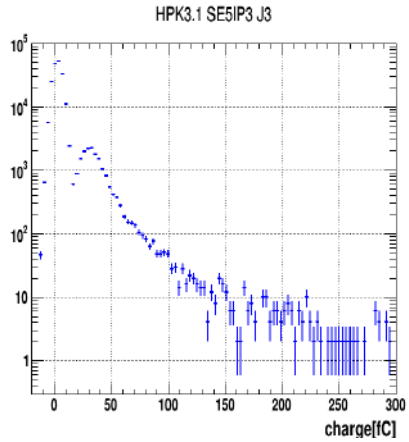

(b) Charge collected by HPK3.1SE5IP3J3

Figure 5.1: Charge distribution for two un-irradiated sensors HPK3.1SE5IP3J1 and HPK3.1SE5IP3J3 at temperature -20^{0}C at channel 1 and channel 2 respectively.

5.2 Amplitude for Un-irradiated Sensor

The amplitude distribution of un-irradiated sensors HPK3.1SE5IP3J1 and HPK3.1SE5IP3J3 for batch 101 is shown in Figure 5.2 (a) and (b) respectively. Where as the amplitudes for the rest of batches are shown in Appendix A.1. From the amplitude shown in Figure 5.2 (a),(b) there are also two peaks as well, the first peak is located around 0 which is the background contribution when beam of particles hits area other than sensor. The second peak is located around 30 mV which is resulted when beam hits the active area of the sensor and induce the signals.

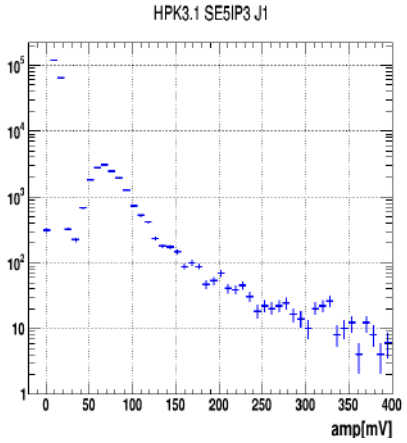

(a) Amplitude of sensor HPK3.1SE5IP3J1

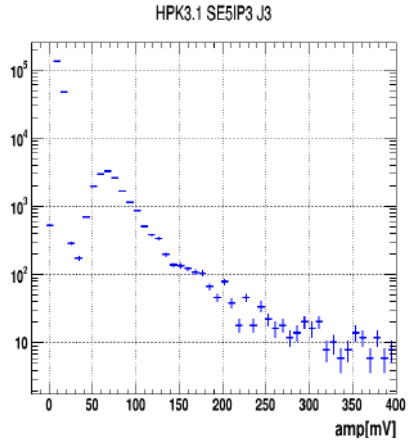

(b) Amplitude of sensor HPK3.1SE5IP3J3

Figure 5.2: Amplitude for HPK3.1SE5IP3J1 and HPK3.1SE5IP3J3 at temperature -20^{0}C at a given voltage 100 V.

5.3 Collected Charge for Irradiated Sensors

The charge distribution of irradiated sensors are studied in various batches. The sensors utilized in batch 601 to batch 605 are HPK3.1W8P2LGE5 and HPK3.2W18P4LGE5 at channel 1 and 2. And the sensors utilized in batch 701 to batch 705 are HPK3.1W82×2SE5IP3 at channel 1 and channel 2, and for batch 1101 to batch 1105 the sensor is HPK3.1W8LGE5, and for batch 1201 to batch 1205 the sensor is HPK3.1W8LGE2 at channel 1 and HPK3.2W18LGE500 at channel 2. These sensors are irradiated with different fluence as shown in Table 5.1. The charge collected by irradiated sensors are shown in Figure 5.3, Figure 5.4, the collected charge by irradiated sensors also have the noise peak and the signal peak. It is clear from the figures that the charge collected by the irradiated sensors get lower which means by the fluence the gain will be decreased as compare to un-irradiated sensors due irradiation. The result for the other batches are shown in Appendix B. Figure 5.4 have very low gain so noise and signals have no difference.

Sensor	**Fluence**	**Bias** Voltage(V)	**Temperature** (°C)	**Batch**	**Ch**
HPK3.1W8P2LGE5	8e14n	390	-37.7 ∼ -35.9	601	1
		450	-35.9 ∼ -34.3	602	
		500	-41.1 ∼ -34.3	603	
		530	-40.8 ∼ -38.2	604	
		560	-32.6 ∼ 35.7	605	
HPK3.2W18P4LGE5	8e14n	250	-37.7 ∼ -35.9	601	2
		300	-35.9 ∼ -34.3	602	
		320	-41.1 ∼ -34.3	603	
		350	-40.8 ∼ -38.2	604	
		390	-32.6 ∼ 35.7	605	
HPK3.1W82×2SE5IP3	1.5e15n	390	-30.9 ∼ -27.6	701	1,2
		530	-31.7 ∼ -28	702	
		570	-35.5 ∼ -32	703	
		600	-34.9 ∼ -32.7	704	
		650	-34.3 ∼ -33.4	705	
HPK3.1W8LGE5	1e15p	550	-48 ∼ -45.9	1101	1
		570	-46.7 ∼ -45	1102	
		600	-44.6 ∼ -42.5	1103	
		650	-38.6 ∼ -32	1104	
		700	-37.4 ∼ -34.1	1105	
HPK3.1W8LGE2	3e15n	530	-47.3 ∼ -45.5	1201	1
		570	-45.7 ∼ -42.2	1202	
		600	-41.8 ∼ -39.3	1203	
		650	-38.1 ∼ -31	1204	
		700	-38.2 ∼ -38	1205	
HPK3.2W18LGE500	3e15n	530	-47.3 ∼ -45.5	1201	2
		570	-45.7 ∼ -42.2	1202	
		600	-41.8 ∼ -39.3	1203	
		650	-38.1 ∼ -31	1204	
		700	-38.2 ∼ -38	1205	

Table 5.1: Irradiated sensors tested in March-2019 test-beam at DESY for the HGTD.

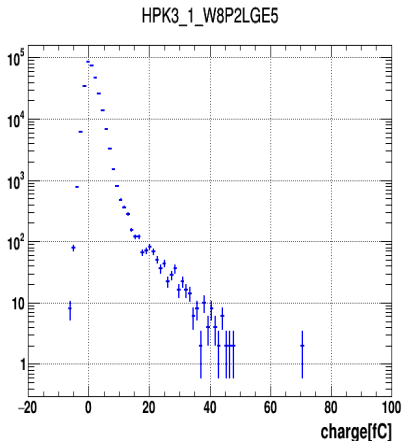

(a) HPK3.1W8P2LGE5 charge for batch601-1

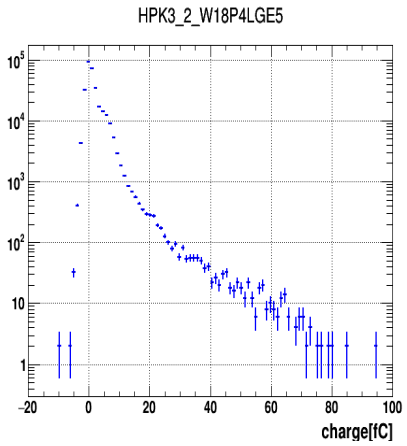

(b) HPK3.2W18P4LGE5 charge for batch601-2

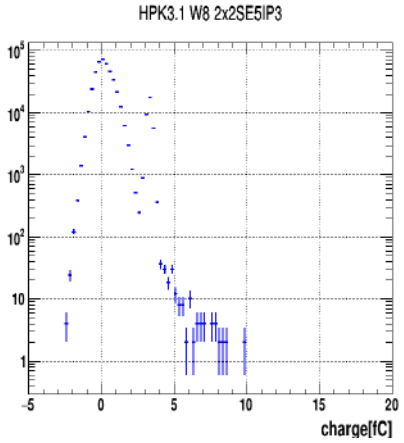

(c) HPK3.1W8 2×2SE5IP3 charge for Sensor b701-1

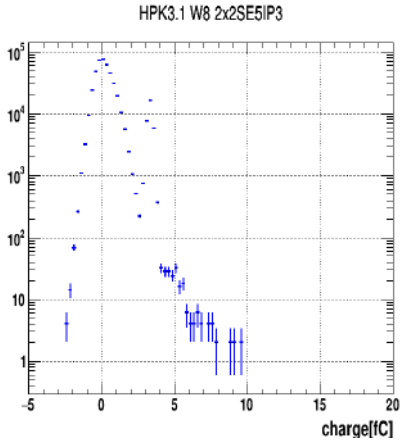

(d) HPK3.1W8 2×2SE5IP3 charge for b701-2

Figure 5.3: Charge collected by irradiated sensors with different fluence, bias voltage and temperature shown in table 4.2.

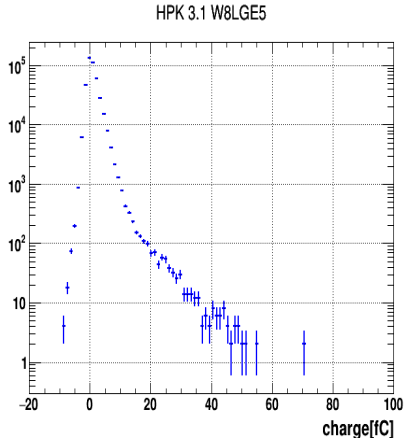

(a) Charge of Sensor HPK3.1 W8LGE5 for batch1101

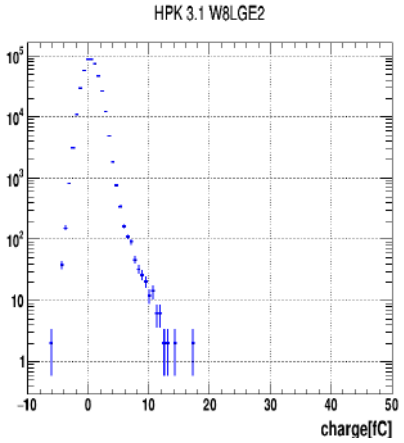

(b) HPK3.1 W8LGE2 charge for b1201-1

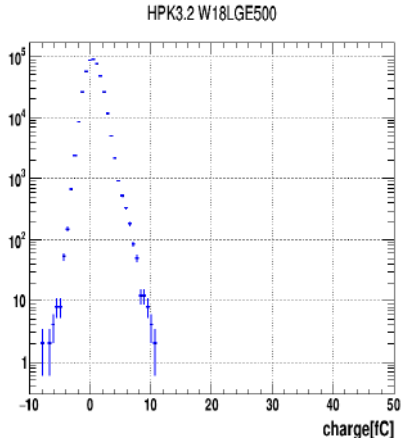

(c) HPK3.2 W18 LGE500 charge for b1201-2

Figure 5.4: Charge collected by irradiated sensors with different fluence, bias voltage and temperature shown in table 4.2.

5.4 Amplitude of Irradiated Sensors

The amplitudes of irradiated sensors presented in Table 5.1 are shown in Figure 5.5 and Figure 5.6. The amplitude of irradiated sensors also contains the peaks both for the signal and background noise. It is clear from the figures that irradiated sensors have lower gain due to irradiation as compare to un-irradiated sensors. The plots for the other batches are shown in Appendix-

B.1.

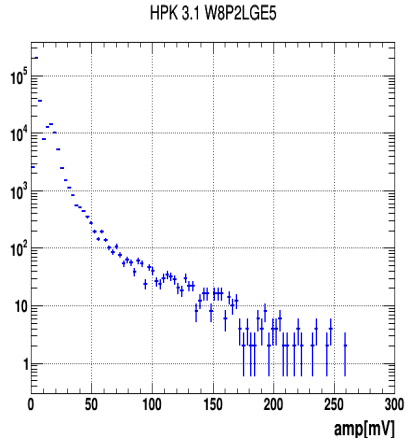

(a) Amplitude of sensor HPK3.1W8P2LGE5

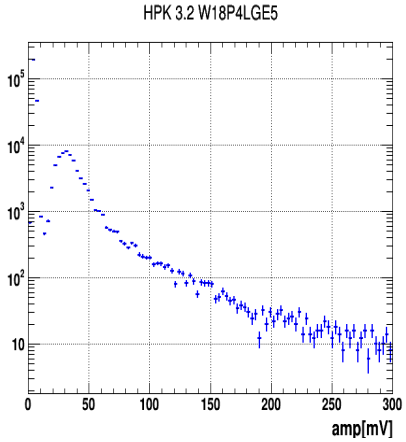

(b) Amplitude of sensor HPK3.2W18P4LGE5

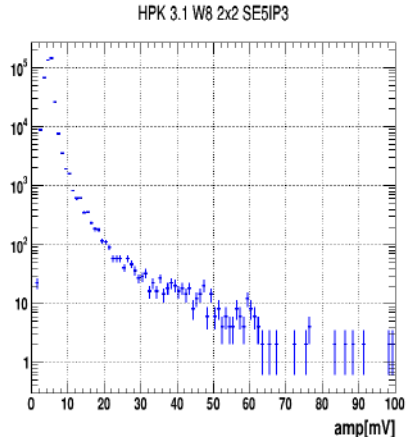

(c) Amplitude of sensor HPK3.1W8 2×2SE5IP3

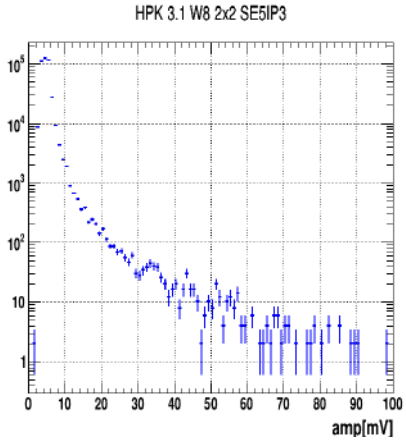

(d) Amplitude of HPK3.1W8 2×2SE5IP3

Figure 5.5: The amplitude of irradiated sensors for different fluence, bias Voltage and temperature for channel 1 and channel 2.

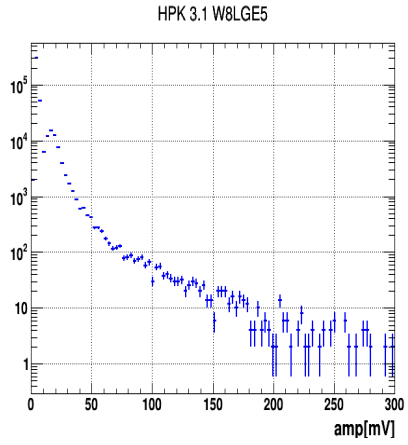

(a) amp of sensor HPK3.1W8LGE5 for batch1101

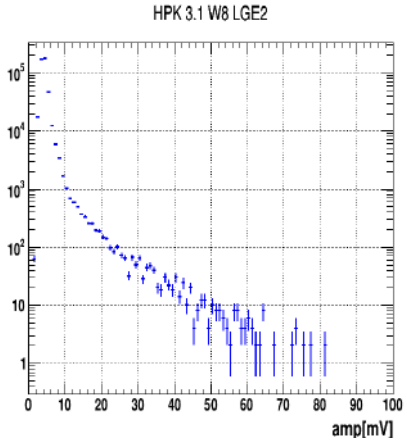

(b) Amplitude of sensor HPK3.1W8LGE2 for batch1201-1

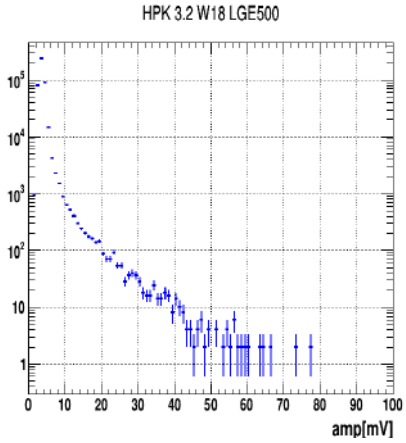

(c) Amplitude of sensor HPK3.2W18LGE500 for batch1201-2

Figure 5.6: Amplitude for HPK3.1W8LGE5 at channel 1, HPK3.1W8LGE2 and HPK3.2W18LGE500 sensor at channel 1,2.

5.5 Background Removal Strategy

To perform a precise analysis it is very important to separate background noise from all the real pulses caused by particles that are passing through the DUTs. Our strategy of background removal noise is to obtain the sensor active pad area. This was make possible by utilizing the beam-telescope data

to plot the collected charge and amplitude inside and outside the sensor pad area. Then by applying several cuts along X-axis and Y-axis on the charge and amplitude, we can explicitly see the difference between the signals and background. Choosing events which hits the sensor active area and draw the plots we reduced the background successfully.

5.5.1 Tracking Plots of Un-irradiated Sensors

The tracking plots of un-irradiated sensors are shown in Figure 5.7. From figures we found the sensor area with clear edges for un-irradiated sensors with no noisy pixels. Choose the event which hit on the sensor region (x: 9.4 mm $\sim$ 10.4 mm, y: 4.8 mm $\sim$ 5.8 mm) an draw the plot we have successfully reduce the background. This is the sensor area which generate signals.

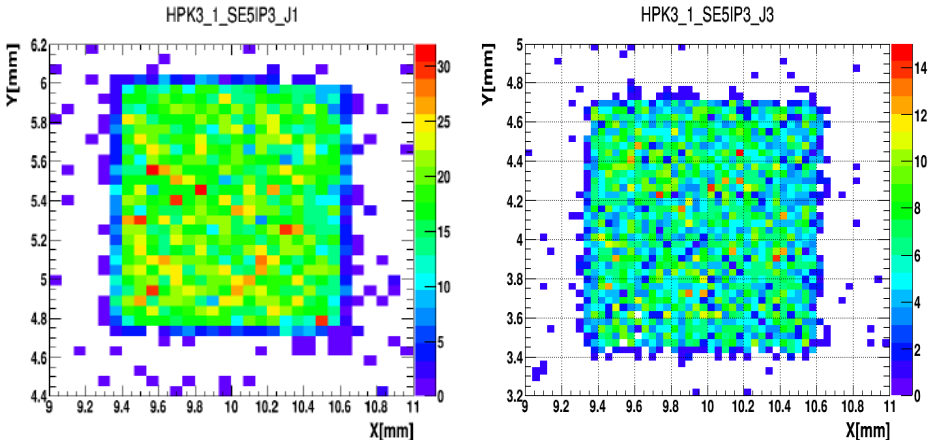

(a) (b)

Figure 5.7: Tracking plots of un-irradiated sensors HPK3.1SE5IP3J1 and HPK3.1SE5IP3J3 at temperature -20°C.

5.5.2 Tracking Plots of Irradiated Sensors

Tracking plots of sensors irradiated with different fluence are shown in Figure 5.8 and Figure 5.9. From the figures we can see the sensor dimension however

there are some pixels Figure 5.8 (a) which are noisy pixels. One of the possible reason is that pixels are not giving us signal is the irradiation of neutron dose. In Figure 5.9 we can see that with clear edges and sensors area.

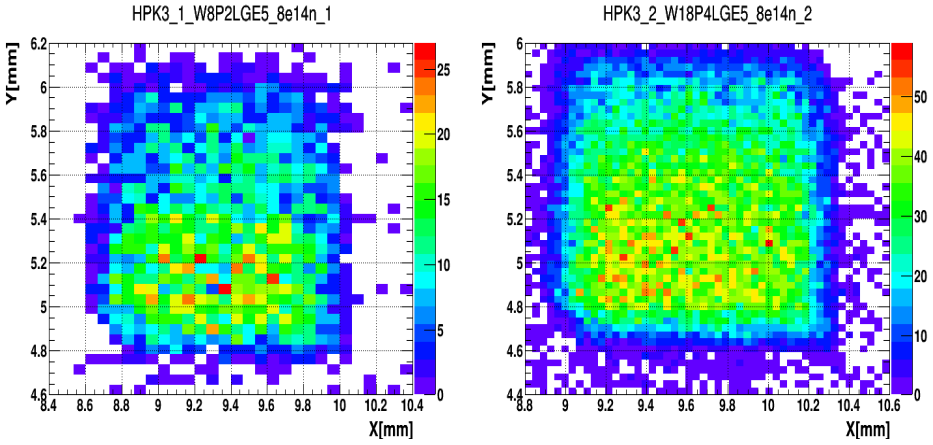

(a) (b)

Figure 5.8: Tracking plots of sensors HPK3.1W8P2LGE5 and HPK3.2W18P4LGE5 utilized in batch 60X with fluence 8e14n.

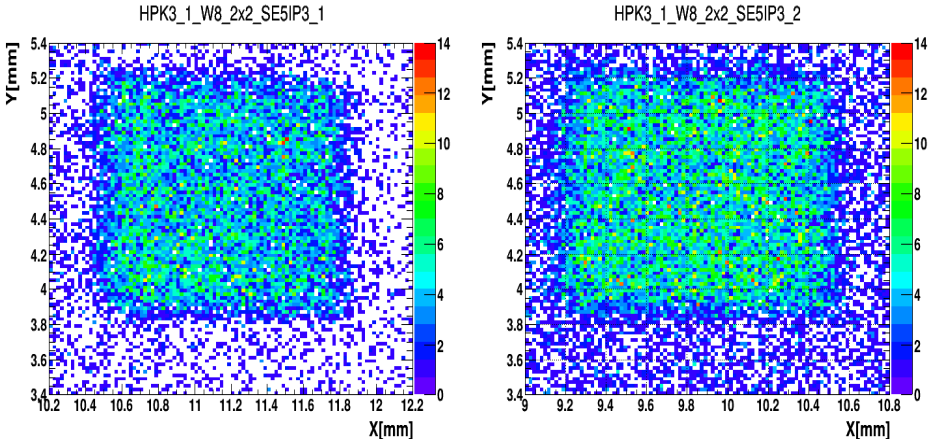

(a) (b)

Figure 5.9: Tracking plots of sensor HPK3.1W82×2SE5IP3 utilized in batch 70X with fluence 1.5e15n.

5.5.3 Background removing

In the section 5.1 and section 5.2, as the DUT collected charge and pulse-height distributions are contaminated by the background noises. To discriminate the signal and noise we use the geometry of the DUT that were obtain from the telescope data as discussed in section 5.5. When the charge pulse-height distributions are plotted inside the sensor pad region Figure 5.10 the background contribution is successfully removed from our signal shown in Figure 5.11. We also plot the distributions outside the sensor active pad region which yields the background contaminating the signal as shown in Figure 5.12.

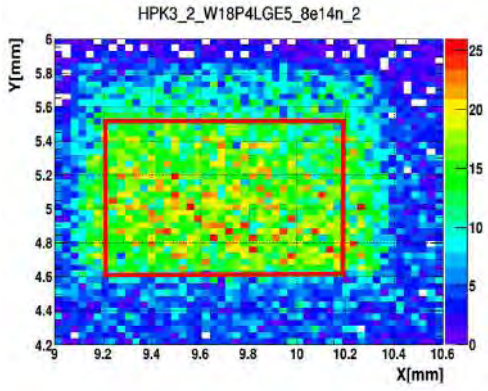

Figure 5.10: sensor active area which gives signal.

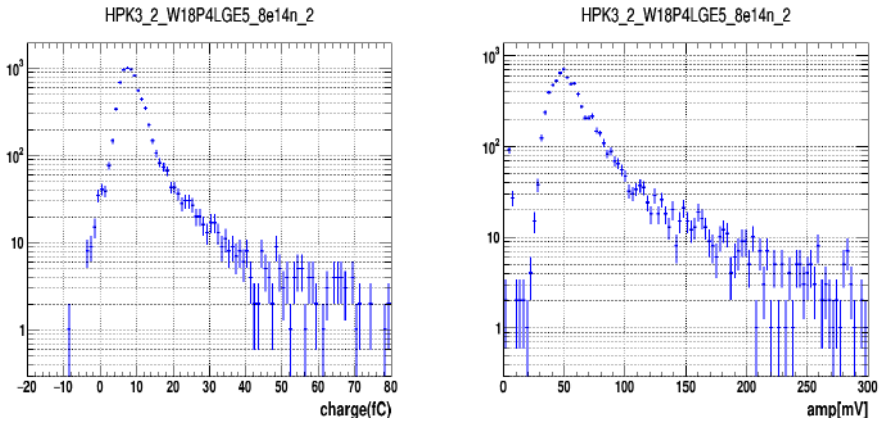

(a) (b)

Figure 5.11: (a) Charge distribution inside the sensor. (b) Amplitude inside the sensor area.

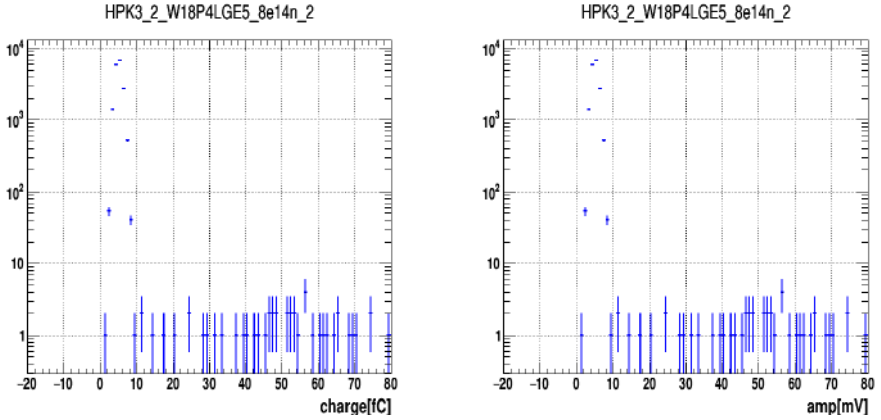

(a) (b)

Figure 5.12: (a) Charge outside the sensor. (b) Amplitude outside the sensor.

5.5.4 Fitting Function

After successfully removing the noise from our signal. We studied some important properties of pulse for the sensors as shown in Table 4.1. We apply a fit functions which is the convolution of landau and gaussian function to our data. The main goal of the this function is to take out a most probable signal value and width of the distribution. This function is particularly used for

the comparison of normalized characteristic energy that is deposited at fixed momentum, the most probable value is a more authentic then the mean of the signal distribution. This fit is construct on a numerical approximation of the landau distribution which is convoluted with a gauss distribution, which accounts for the electronic noise contributions to the signal and gaussian part in the energy deposition. The function fits location and width of the landau part together with sigma of the gaussian part. The out put gives the most probable signal, the full width at half maximum (FWHM) of the fit and its normalization.
The charge distributions and pulseheight that are fitted by the function (Landau, gauss) discussed above for un-irradiated sensors are shown in Figure 5.13, and for irradiated sensors are shown in Figure 5.14, Figure 5.15, Figure 5.16 and Figure 5.17. The rest of plots for charge with fitting function are shown in Appendix C and for amplitude with fitting function are shown in Appendix C.1

After fitting each distribution (charge, pulseheight) the most probable value (MPV) is obtained. The comparison of the MPV among the un-irradiated and irradiated sensors is discussed in section 5.6.

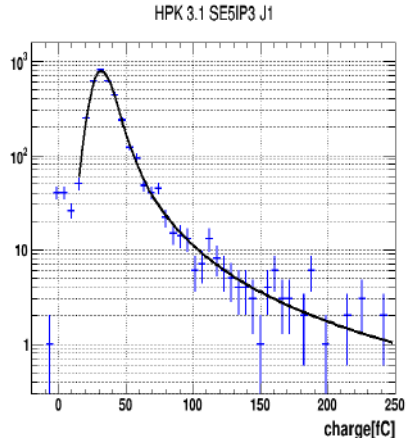

(a) HPK3.1SE5IP3J1 charge distribution MPV = 2.64 (fC)

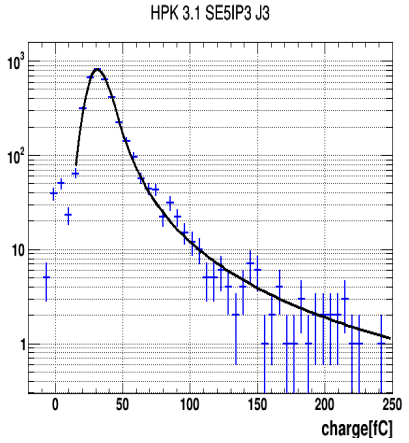

(b) HPK3.1SE5IP3J3 charge distribution MPV = 4.426 (fC)

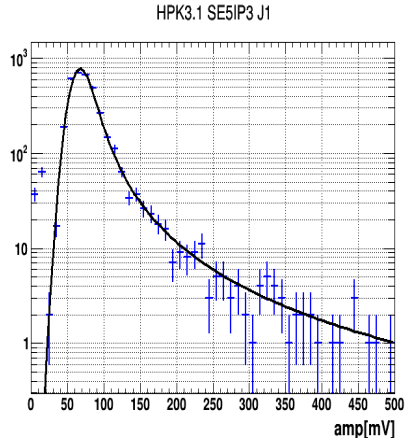

(c) HPK3.1SE5IP3J1 pulseheight distribution MPV = 62.99 (mV)

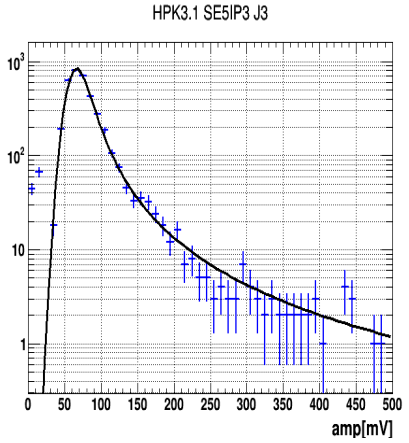

(d) HPK3.1SE5IP3J3 pulseheight distribution MPV = 62.29 (mV)

Figure 5.13: Charge and pulseheight distribution for un-irradiated HPK sensors and fitted with (landau, gauss) function.

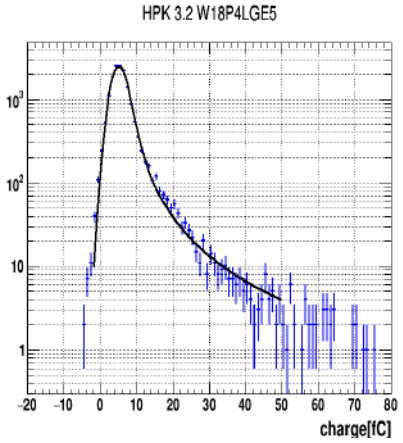

(a) HPK3.2W18P4LGE5 charge distribution MPV = 2.64 (fC)

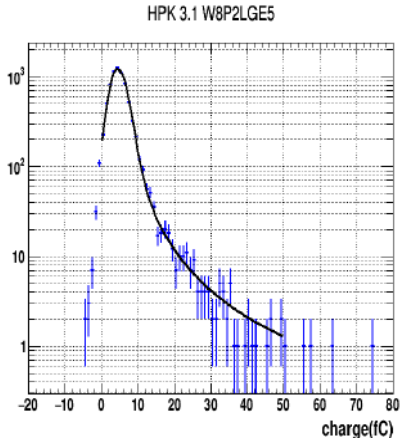

(b) HPK3.1W8P2LGE5 charge distribution MPV = 4.426 (fC)

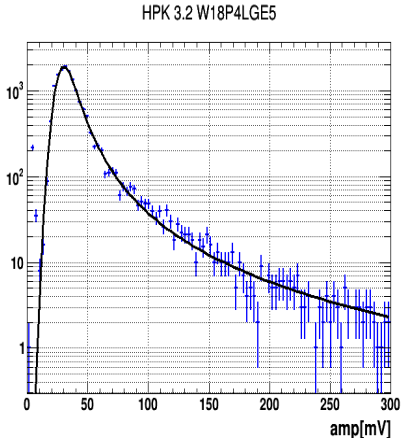

(c) HPK3.2W18P4LGE5 pulseheight distribution MPV = 28.42 (mV)

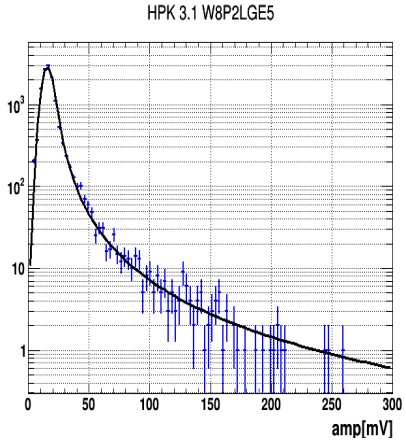

(d) HPK3.1W8P2LGE5 pulseheight distribution MPV = 14.06 (mV)

Figure 5.14: Charge and pulseheight distribution for irradiated HPK sensors and fitted with (landau, gauss) function.

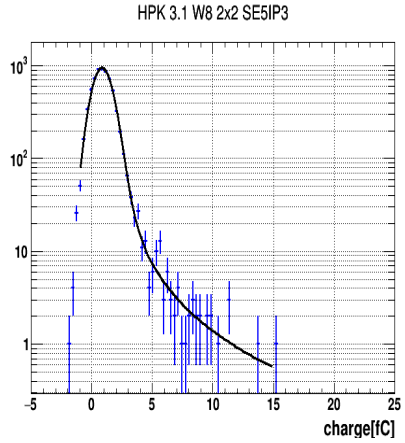

(a) HPK3.1W82x2SE5IP3 charge distribution MPV = 0.6984 (fC)

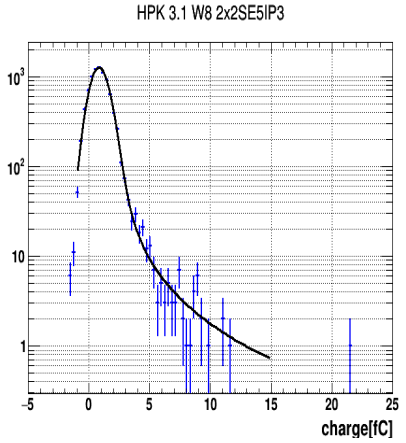

(b) HPK3.1W82x2SE5IP3 charge distribution MPV = 0.6826 (fC)

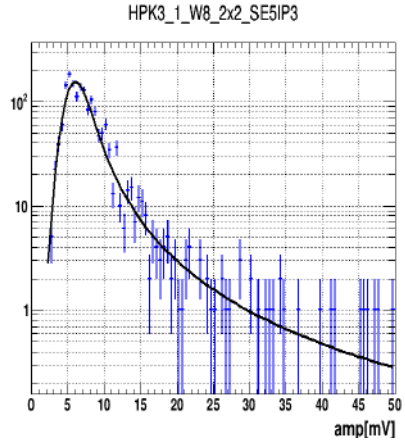

(c) HPK3.1W82x2SE5IP3 pulse-height distribution MPV = 5.588 (mV)

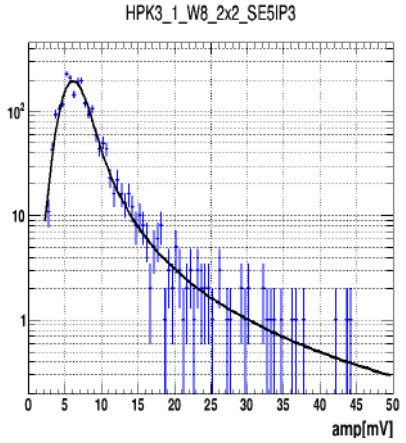

(d) HPK3.1W82x2SE5IP3 pulse-height distribution MPV = 5.582 (mV)

Figure 5.15: Charge and pulseheight distribution for irradiated HPK sensors and fitted with (landau, gauss) function.

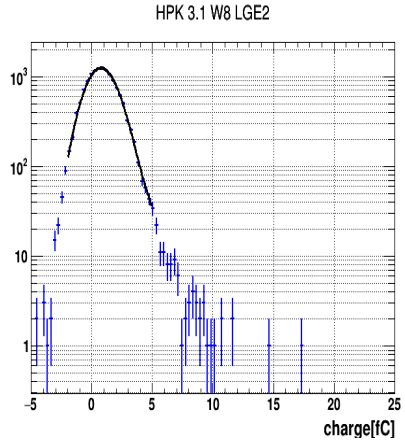

(a) HPK3.1W8LGE2 charge distribution MPV = 0.5155 (fC)

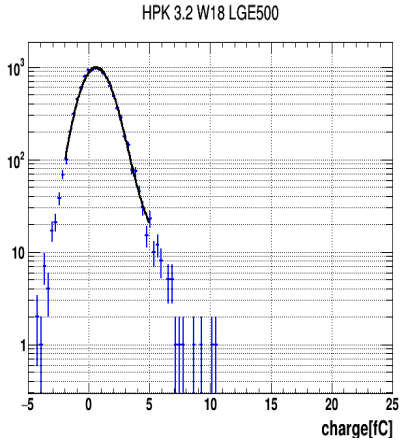

(b) HPK3.2W18LGE500 charge distribution MPV = 0.3513 (fC)

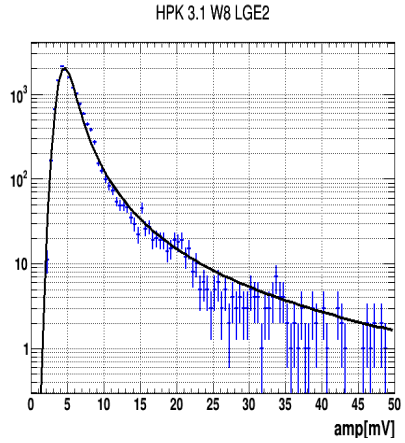

(c) HPK3.1W8LGE2 pulseheight distribution MPV = 1.32 (mV)

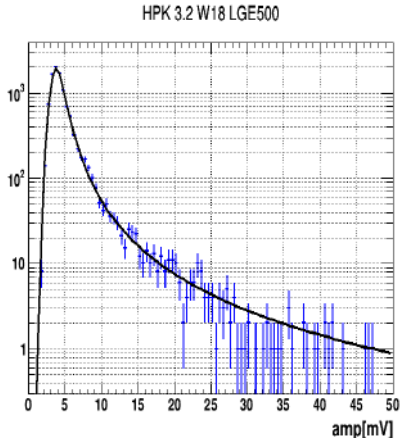

(d) HPK3.2W18LGE500 pulseheight distribution MPV = 3.537 (mV)

Figure 5.16: Charge and pulseheight distribution for irradiated HPK sensors and fitted with (landau, gauss) function.

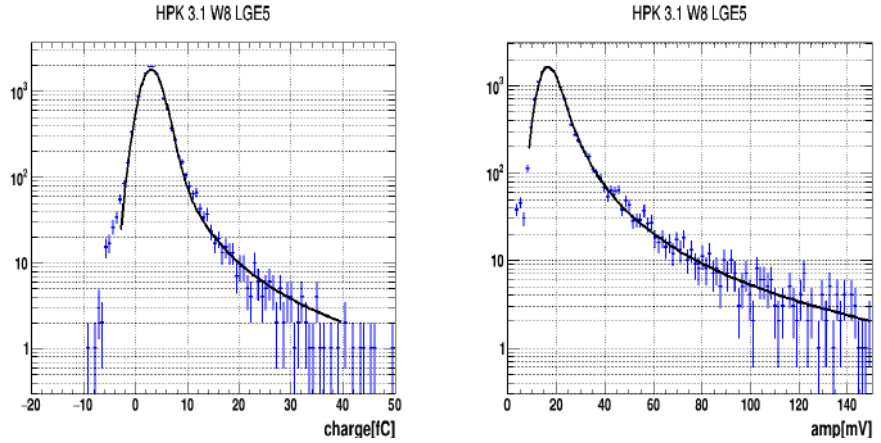

(a) HPK3.1W8LGE5 charge distribution MPV = 2.554 (fC)

(b) HPK3.1W8LGE5 pulseheight distribution MPV = 15.31 (fC)

Figure 5.17: Charge and pulseheight distribution for irradiated HPK sensors and fitted with (landau, gauss) function.

5.6 Comparison of Bias Voltage Vs Charge and Pulseheight for HPK Sensors

We studied the charge distribution for un-irradiated and irradiated sensors with different fluences placed at different channel. Here we will compare the results of the sensors collectively for the bias voltage (V) vs charge (fC). The charge distributions for all the sensors are shown in Figure 5.18. From the figure it is clear that as the bias voltage across the sensor is increasing the collected charge value is also increasing. By comparing the un-irradiated sensor with irradiated one we found that high bias voltage is needed to have relatively large gain for the irradiated sensors. The minimum threshold charge value for HGTD requirements is 2 (fC). By comparing HPK3.1W8LGE2 (3e15n) and HPK3.2W18LGE500 (3e15n) we found that HPK3.2W18LGE500 (3e15n) have achieved the minimum threshold value at bias voltage of 700 while HPK3.1W8LGE2 (3e15n) did not achieved the value.

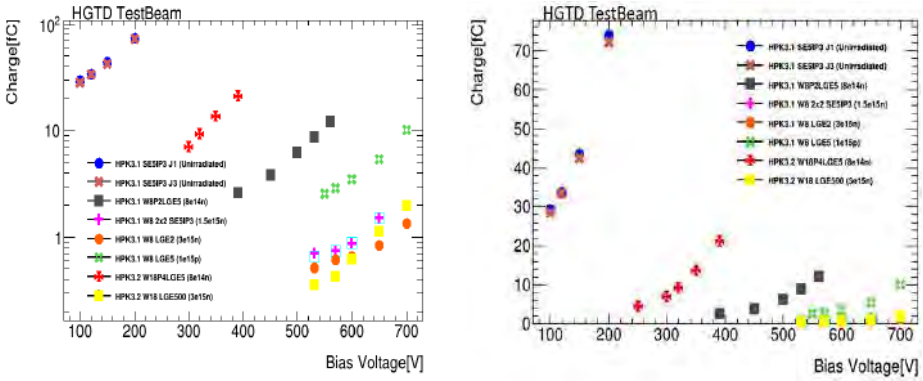

(a) Charge vs bias voltage log scale plot.

(b) Charge vs bias voltage non log scale plot.

Figure 5.18: Charge vs bias voltage for all the sensors mention in table 4.2 for different channels.

We also make comparison of the pulseheight of MPV obtain when fit is applied. We observe same trend similar to charge i.e. the amplitude is increasing with increase of bias voltage across the sensors. We also found that the for irradiated sensors we need high bias voltage to have a comparable gain compared to un-irradiated sensors as shown in figure.

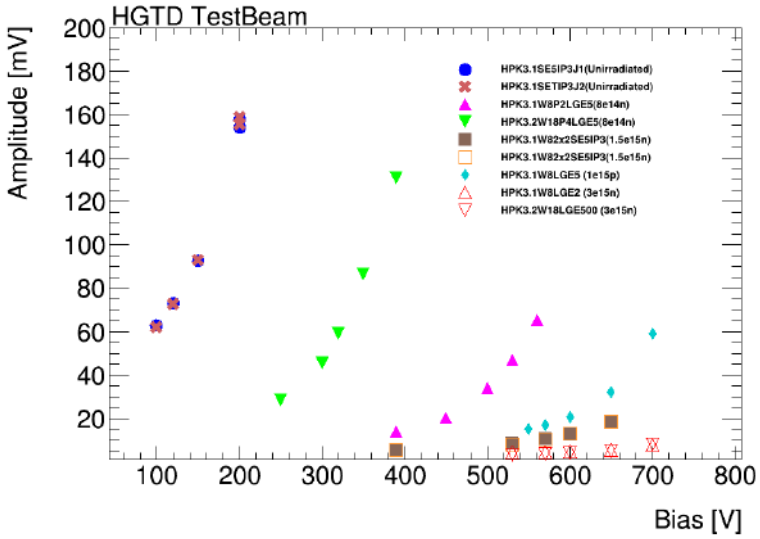

Figure 5.19: Comparison of pulseheight vs bias voltage for HPK sensors.

5.7 Comparison of Bias Voltage Vs Noise for HPK Sensors

When a signal is transmitted and received, a physical process called noise is always associated with it. Noise is basically any undesired signals added to the ideal signal. For most of the time, the noise while having no passing particle is kept at a notable lower amplitude than the amplitude from a particle passing through the sensor. As long as this is the case it is not difficult to separate the events with a pulse registered from the events only containing noise. However, there are some instances when the sensor is generating a pulse large enough to be registered as an actual pulse, even though no signal is passing through at that time. In Figure 5.20 a comparison plot for the noise vs bias voltage for both un-irradiated and irradiated is shown. For highly irradiated sensors noise is independent of bias-voltage however, for HPK3.1W8P2LGE5 (8e14n) and HPK3.2W18P4LGE5 (8e14n) sensors the noise is not constant in two batches.

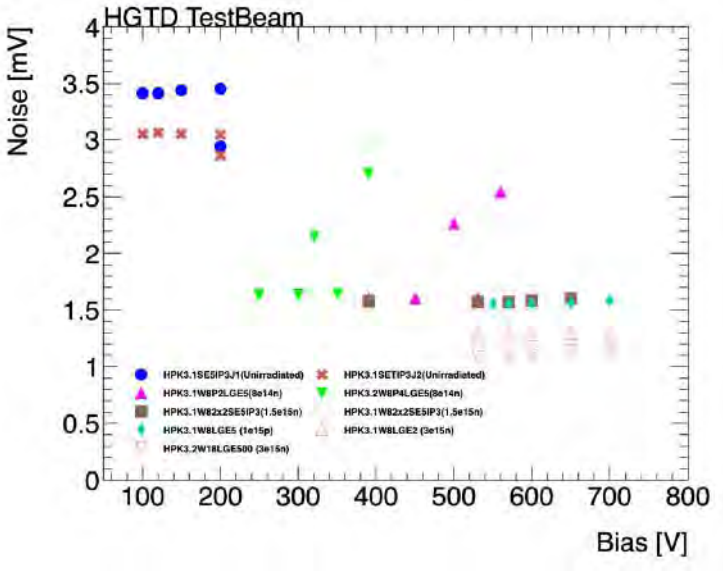

Figure 5.20: Comparison of noise distribution vs bias voltage for HPK sensors.

5.8 Comparison of Bias Voltage Vs Signal-to-Noise (S/N) Ratio for HPK Sensors

The graph is drawn for the amplitude (signal)-to-noise ratio vs bias voltage utilizing un-irradiated and irradiated sensors. Signal-to-noise (S/N) ratios are calculated by amplitude over noise. In Figure 5.21 we can see for un-irradiated sensor, HPK3.1SE5IP3J3 has high S/N ratio as compare to HPK3.1SE5IP3J1. Moreover S/N ratios for un-irradiated sensors and irradiated with different fluence also increase with increasing the bias voltage. Higher the signal-to-noise ratios higher will be the gain.

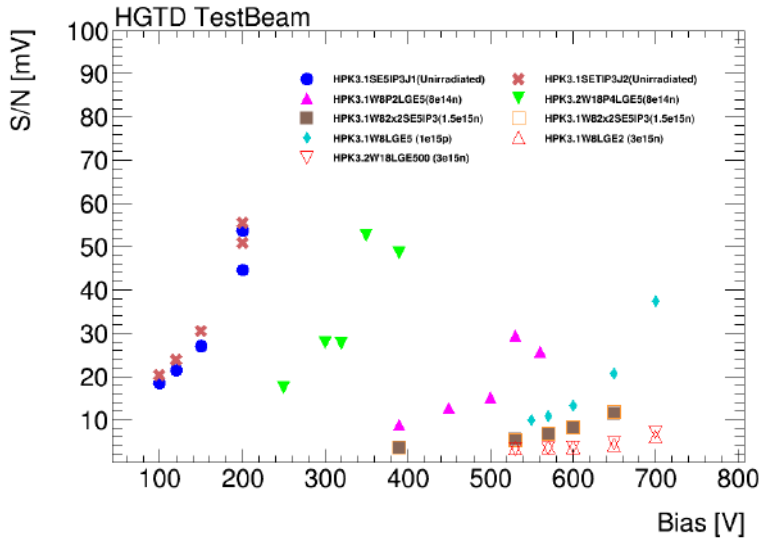

Figure 5.21: Comparison of signal-to-noise vs bias voltage for HPK sensors.

5.9 Time Resolution Study of HPK Sensors

The time resolution of the LGADs sensors was calculated by using the time difference of when a particle arrived at the SiPM and the LGAD [43]. The time of arrival of pulse could be determined by using e.g. a constant threshold of the measured voltage, time at the maximum voltage or CFD (Constant Fraction Discriminator) which was described in subsection 3.6.4. The CFD is a method used to minimize the time walk effect by defining the time of arrival as the time where the signal crosses a constant fraction (f_{CFD}) of the maximum amplitude [36]. Figure 5.22, shows the TimeCFD20 distribution for batch 101. As for SiPM and un-irradiated sensors the signals and background are clearly separated, because these have high gain as compared to irradiated sensors. The plots for other batches are placed in Appendix D.

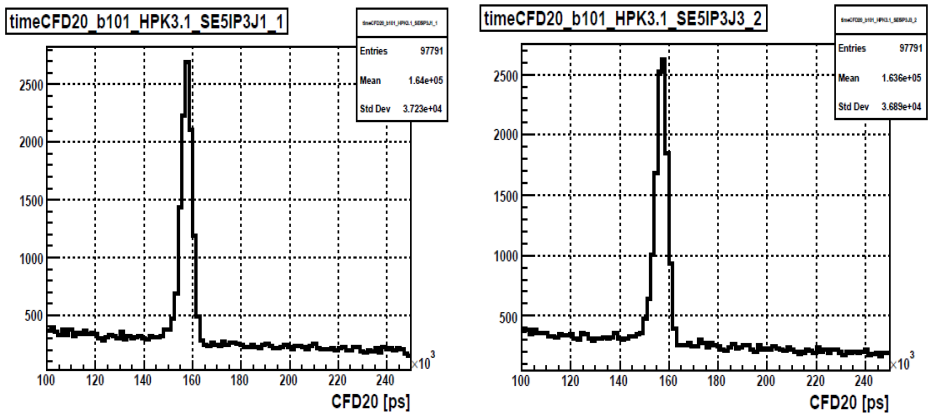

(a) TimeCFD20 distribution for HPK3.1SE5IP3J1.

(b) TimeCFD20 distribution for HPK3.1SE5IP3J3.

Figure 5.22: TimeCFD20 distribution for batch 101, un-irradiated HPK sensors utilized at channel 1 and channel 2.

Figure 5.24 shows the TimeCFD50 distribution for irradiated sensors. For the irradiated sensors the signal and background peaks were not clearly separated, so we want to have less background contribution. That is why we use TimeCFD50 for irradiated sensors. Because they have very low gain, we have to reduce the noise.

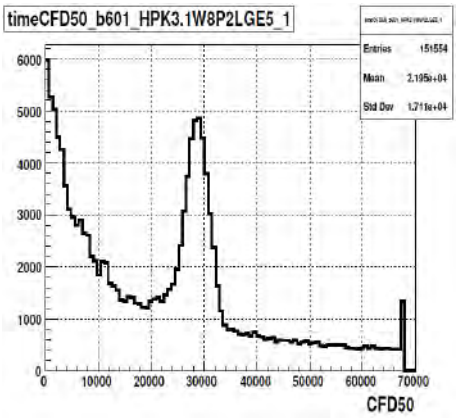

(a) TimeCFD50 distribution for HPK3.1W8P2LGE5.

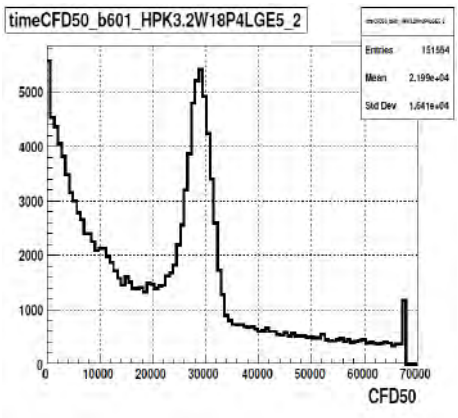

(b) TimeCFD50 distribution for HPK3.2W18P4LGE2.

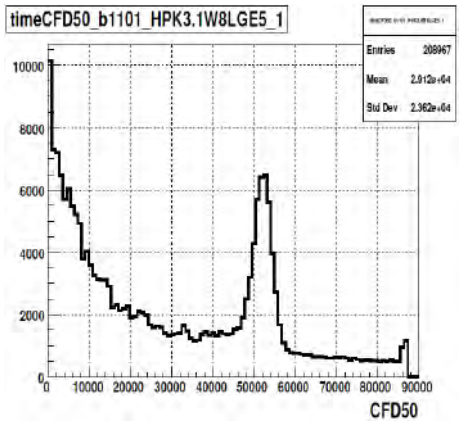

(c) TimeCFD50 distribution for HPK3.1W8LGE5.

Figure 5.23: TimeCFD50 distribution for batch 601 channel 1(a), TimeCFD50 distribution for batch 601 channel 2(b), and TimeCFD50 distribution for batch 1101 channel 1(c).

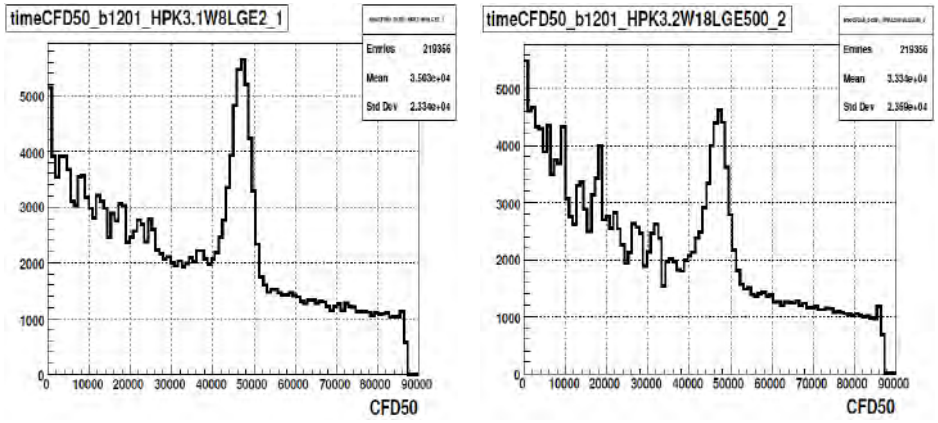

(a) TimeCFD50 distribution for HPK3.1W8LGE2.

(b) TimeCFD50 distribution for HPK3.2W18LGE500.

Figure 5.24: TimeCFD50 distribution for batch 1201 channel 1(a), TimeCFD50 distribution for batch 1201 channel 2(b).

5.10 TimeCFD vs Amplitude

In order to remove the background contribution from the time that we reconstructed for each sensors as discussed in section 5.9, we follow the strategy to find a relationship between TimeCFD20 and pulseheight (amplitude of the sensor distribution) for un-irradiated sensor shown in Figure 5.25, and for irradiated sensors relationship between TimeCFD50 and pulseheight are shown in Figure 5.26 and Figure 5.27. From the relations, if we apply some cuts on the amplitude we can remove the background from the TimeCFD20 and TimeCFD50. The plots for other batches are placed in Appendix E.

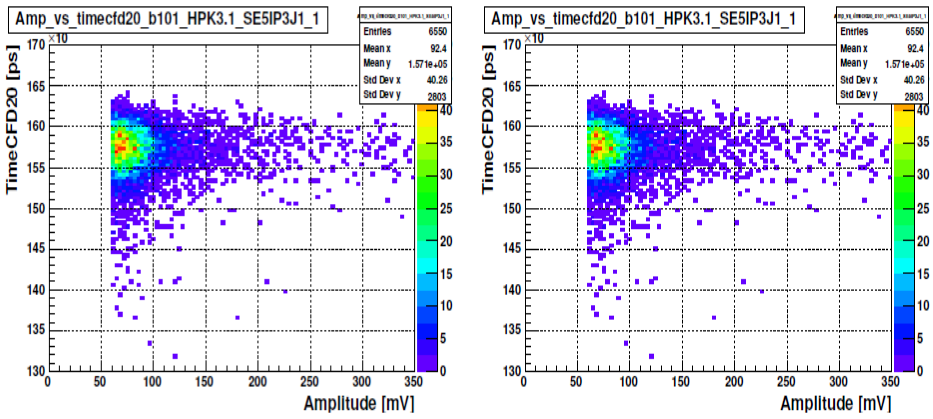

(a) Amplitude vs TimeCFD20 for HPK3.1SE5IP3J1.

(b) Amplitude vs TimeCFD20 for HPK3.1SE5IP3J3.

Figure 5.25: TimeCFD20 vs amplitude plots for batch 101 channel 1 (a), channel 2 (b).

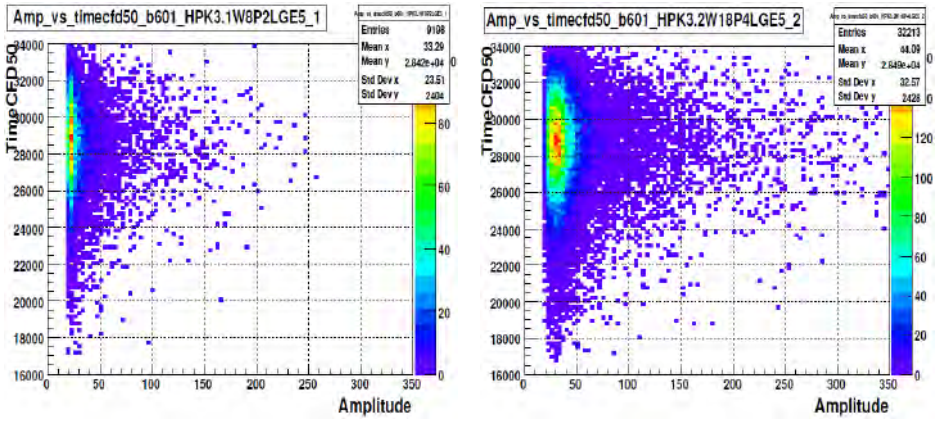

(a) HPK3.1W8P2LGE5 Amplitude vs TimeCFD50.

(b) Amplitude vs TimeCFD50 HPK3.2W18P4LGE5.

Figure 5.26: TimeCFD50 vs amplitude plots for batch 601 channel 1 (a), channel 2 (b).

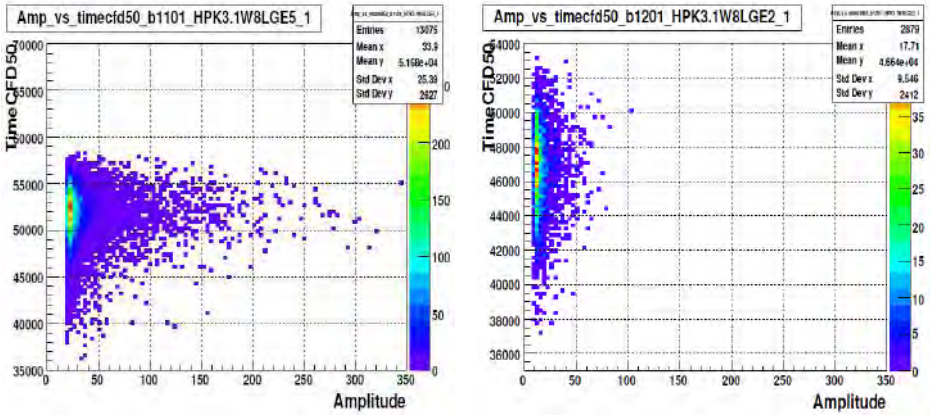

(a) Amplitude vs TimeCFD50 for HPK3.1W8LGE5.

(b) Amplitude vs TimeCFD50 for HPK3.1W8LGE2.

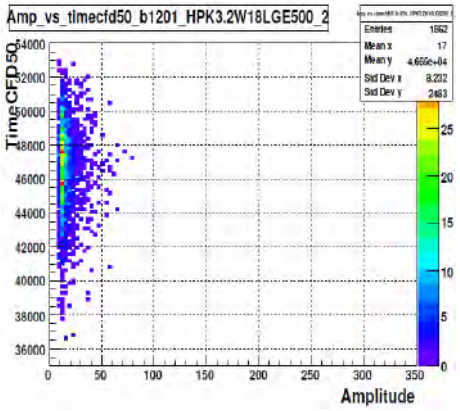

(c) Amplitude vs TimeCFD50 for HPK3.2W18LGE500.

Figure 5.27: TimeCFD50 vs amplitude plots for batch 1101 channel 1 (a), batch 1201 channel 1 (b), batch 1201 channel 2 (c).

5.11 Background Removing

As discussed in section 5.9 that TimeCFD distribution contains both signals and background noise contribution. It is necessary to separate the signal from the background. We applying cuts on the amplitude to remove the background contribution as shown in Figure 5.28, Figure 5.29 and Figure 5.30. The rest of plots for the other batches are placed in Appendix F .

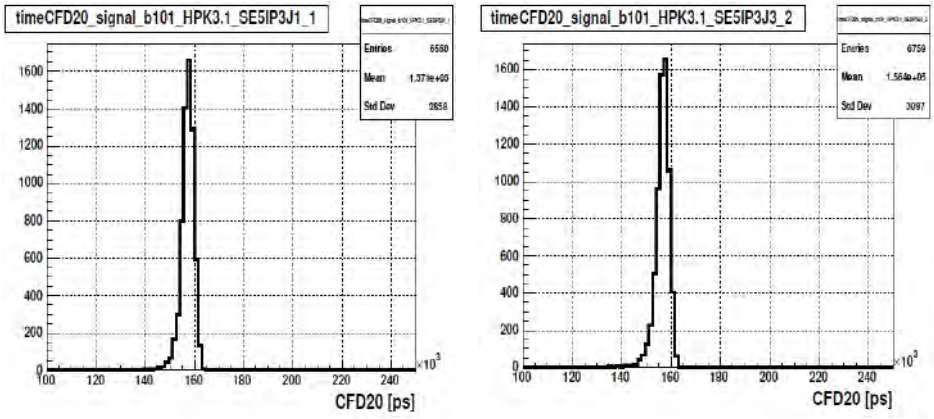

(a) HPK3.1SE5IP3J1 TimeCFD20 signal.

(b) HPK3.1SE5IP3J3 TimeCFD20 signal.

Figure 5.28: Signal contribution after removing background by applying cuts for batch 101 channel 1 (a), batch 101 channel 2 (b).

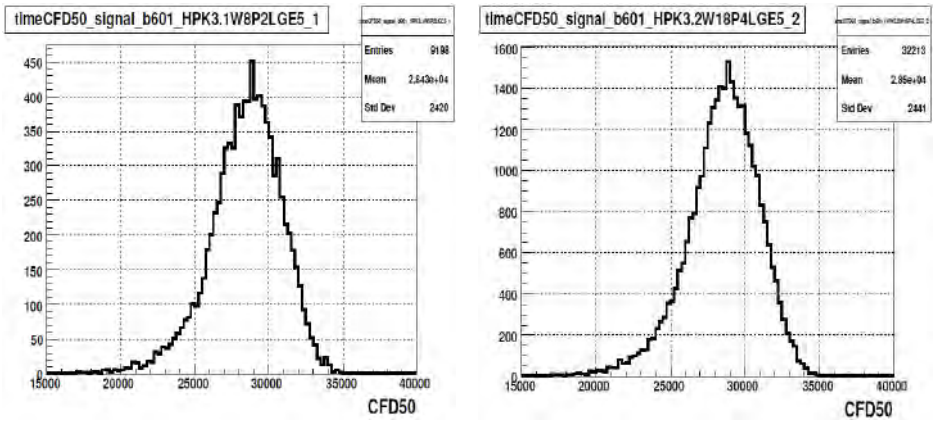

(a) HPK3.1W8P2LGE5 TimeCFD50 signal.

(b) HPK3.2W18P4LGE5 TimeCFD50 signal.

Figure 5.29: Signal contribution after removing background by applying cuts for batch 601 channel 1 (a), batch 601 channel 2 (b).

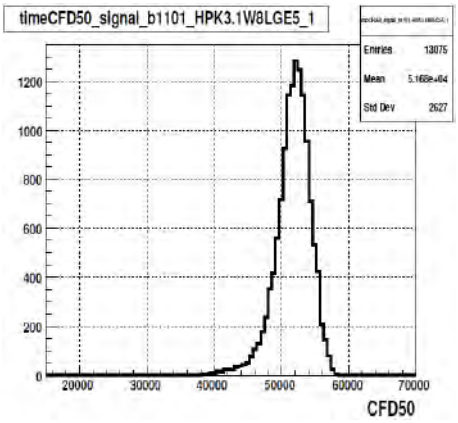

(a) HPK3.1W8LGE5 TimeCFD50 signal.

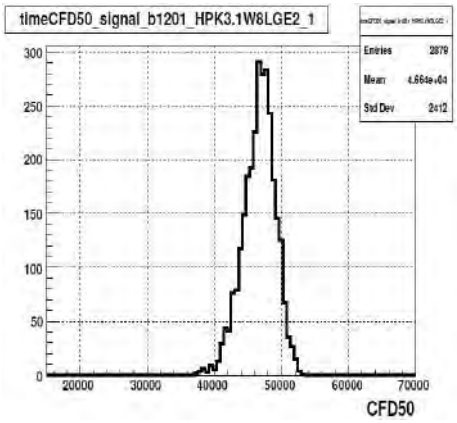

(b) HPK3.1W8LGE2 TimeCFD50 signal.

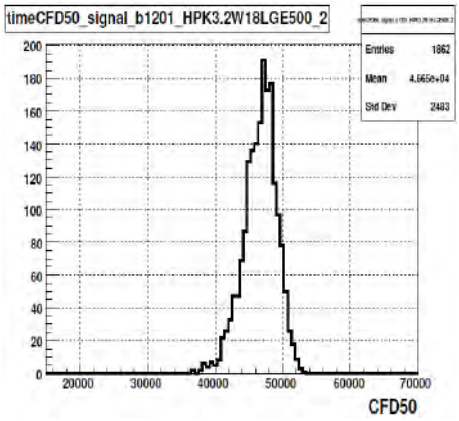

(c) HPK3.2W18LGE500 TimeCFD50 signal.

Figure 5.30: Signal contribution after removing background by applying cuts for batch 1101 channel 1 (a), batch 1201 channel 1 (b), batch 1201 channel 2 (c).

5.11.1 Time Resolution Fitting with Gaussian Function

As mentioned in chapter 4, SiPM is taken as a reference detector in order to calculate the timing resolution. The time resolution of the SiPM is known and usually of the order of 10 ps. The time resolution can be extracted from the width of the time differences computed from the LGADs and the SiPMs.

Constant fraction discriminator method is used here to reduce the effect from time walk effect. The techniques CFD20 and CFD50 are studied here. CFD50 leads to the best timing resolution [44]. Time difference between any two detectors is fitted by a gaussian function, from which we can get the sigma as combined resolution for the system which can be seen in Figure 5.31 for batch 101, where as the plots for the rest of batches are put in Appendix G .

$$\sigma^2_{HPK3.1-SiPM} = \sigma^2_{HPK3.1} + \sigma^2_{SiPM} \tag{5.1}$$

$$\sigma^2_{HPK3.1-LGA35} = \sigma^2_{HPK3.1} + \sigma^2_{LGA35} \tag{5.2}$$

$$\sigma^2_{LGA35-SiPM} = \sigma^2_{LGA35} + \sigma^2_{SiPM} \tag{5.3}$$

Once we get the sigma and put in equation 5.4, equation 5.5 for channel one and channel two respectively.

$$\sigma_{ch1} = \sqrt{\frac{\sigma^2_{ch1ch0} + \sigma^2_{ch1ch3} + \sigma^2_{ch0ch3}}{2}} \tag{5.4}$$

$$\sigma_{ch2} = \sqrt{\frac{\sigma^2_{ch2ch0} + \sigma^2_{ch2ch3} + \sigma^2_{ch0ch3}}{2}} \tag{5.5}$$

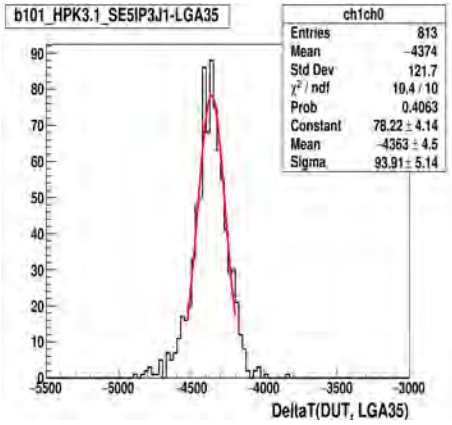

(a) Time difference of device DUT and LGA35.

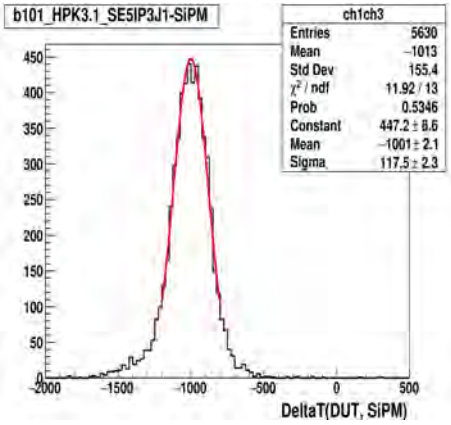

(b) Time difference of device DUT and SiPM.

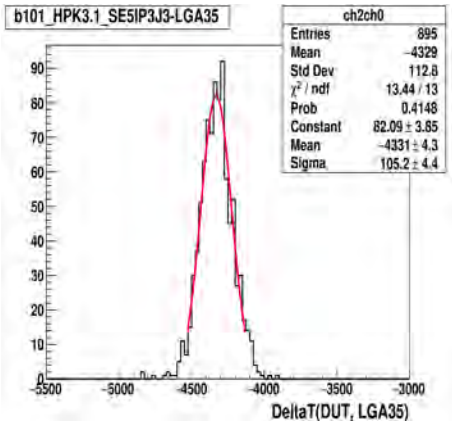

(c) Time difference of device DUT and LGA35.

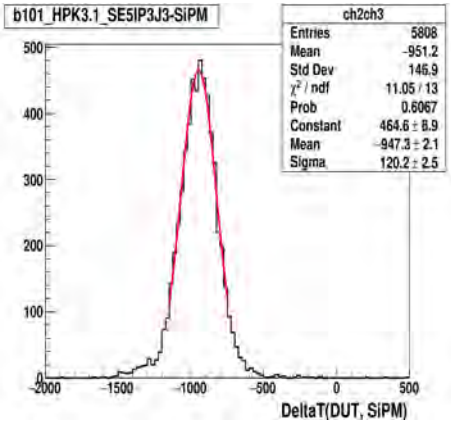

(d) Time difference of device DUT and SiPM.

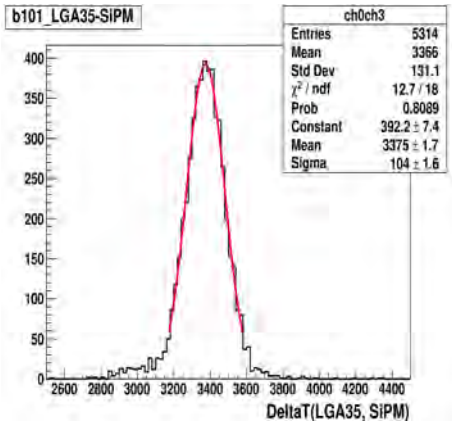

(e) Time difference of device LGA35 and SiPM.

Figure 5.31: Time difference of the devices fitted with gaussian function for batch 101, at different channels.

5.11.2 Time Resolution vs Bias Voltage

Here the performance of the different sensors is studied for the time resolution. The time resolution for un-irradiated sensor HPK3.1-SE5IP3J1 at channel 1 and HPK3.1SE5IP3J3 at channel 2 that are utilized in HGTD test-beam March-2019 from batch 101 to batch 105. Both sensors are kept at temperature -20 and the bias voltage are different for every batch. The detail information for all the sensors are shown in Table 4.2. We can see from the Figure 5.32 that the time resolution of un-irradiated HPK sensors become better and better approaching 30 ps with increasing bias voltage.

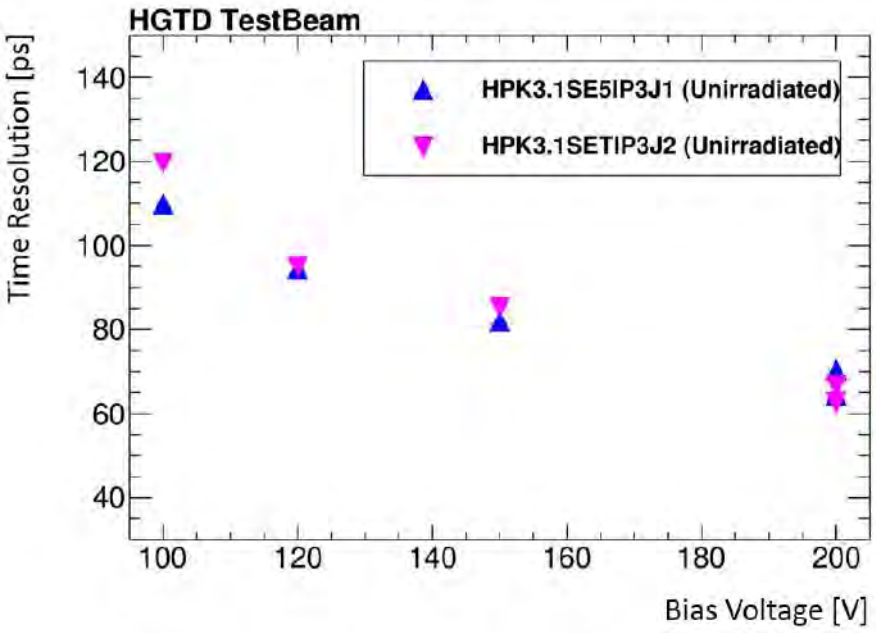

Figure 5.32: Time resolution for the un-irradiated HPK sensors vs bias voltage for batch 101 to batch 105.

The sensors utilized in batch 601 to batch 605 are HPK3.1W8P2LGE5 at channel 1, HPK3.2 W18P4LGE5 at channel 2. Both of the sensors are irradiated with 8e14n. These two sensors shown in Figure 5.33 are also showing better time resolution like the un-irradiated sensors.

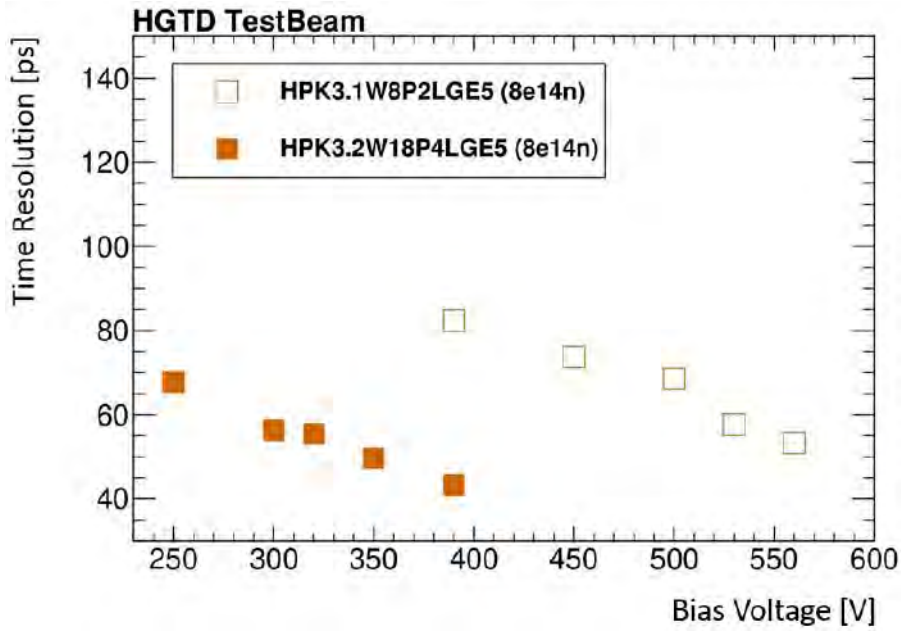

Figure 5.33: Time resolution for the irradiated HPK sensors vs bias voltage for batch 601 to batch 605.

The sensor used in batch 1101 to batch 1105 is HPK3.1W8LGE5 at channel 1, the sensor at channel 2 was dead. This sensor is irradiated with 1e15p which can be seen in Figure 5.34. The performance of this sensor is very bad, at a very high bias voltage the time resolution is around 90 ps.

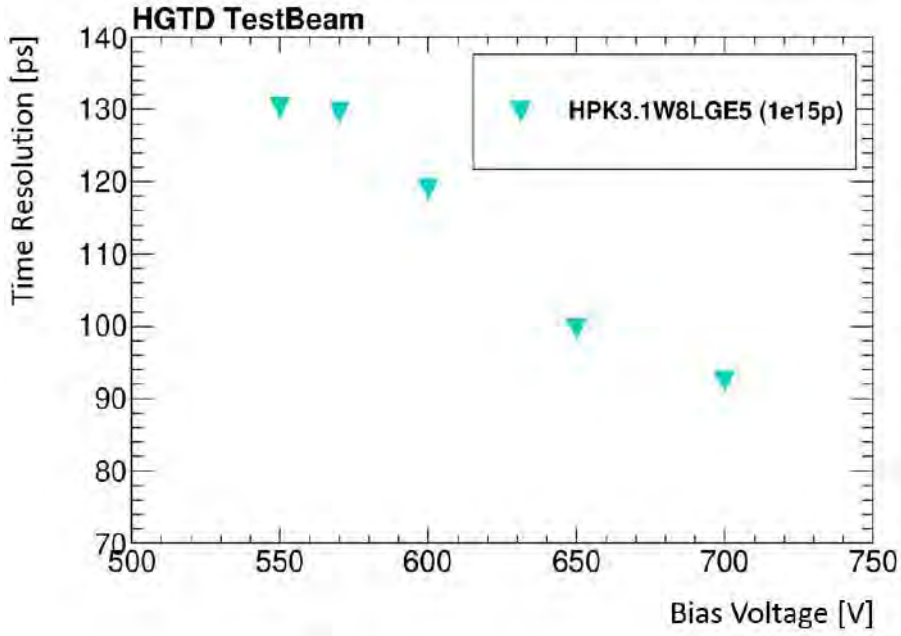

Figure 5.34: Time resolution for the irradiated HPK sensor vs bias voltage for batch 1101 to batch 1105.

The sensors utilized in batch 1201 to batch 1205 are HPK3.1W8LGE2 at channel 1, HPK3.2W18LGE500 at channel 2. Both of the sensors are irradiated with 3e15n. The time resolution for these sensors shown in Figure 5.35 becomes good at a bias voltage of around 600 V and worse at high voltage.

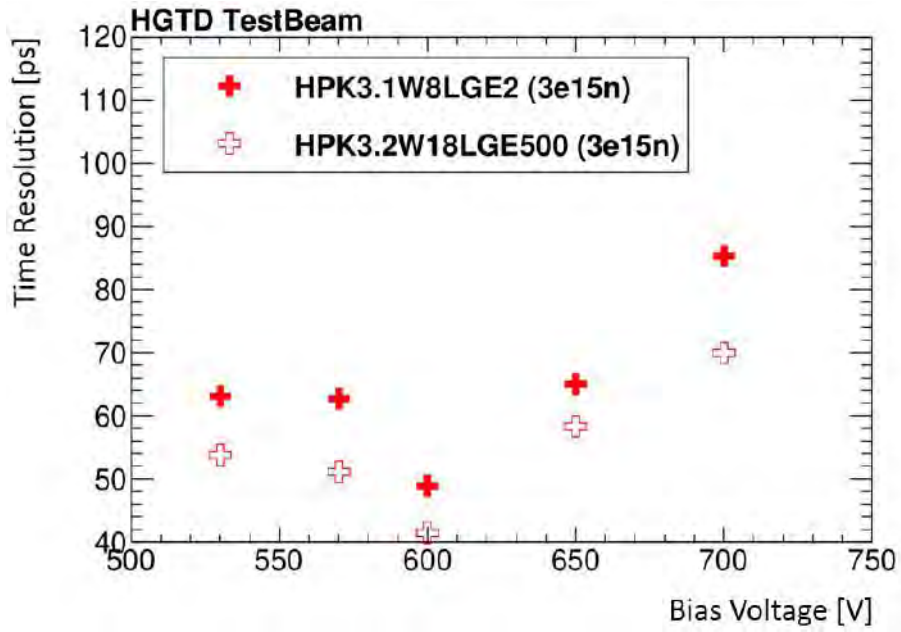

Figure 5.35: Time resolution for the irradiated HPK sensor vs bias voltage for batch 1201 to batch 1205.

Here we plotted the results of all the sensors to compare their performance. The average time resolution per track is about 30 ps at the beginning of HL-LHC. Figure 5.36 shows that highly irradiated sensors need larger bias voltage to obtain high gain as compare to un-irradiated. As the bias voltage increases, the time resolution of un-irradiated sensors changes more than irradiated sensors. The sensor utilized in batch 60X is HPK3.2W18P4LGE5 with fluence 8e14n, performing better than the other sensors. The larger the bias voltage, the better is the performance of time resolution. Except batch 120X, where the bias voltage is larger than 600V, the performance becomes worse as shown.

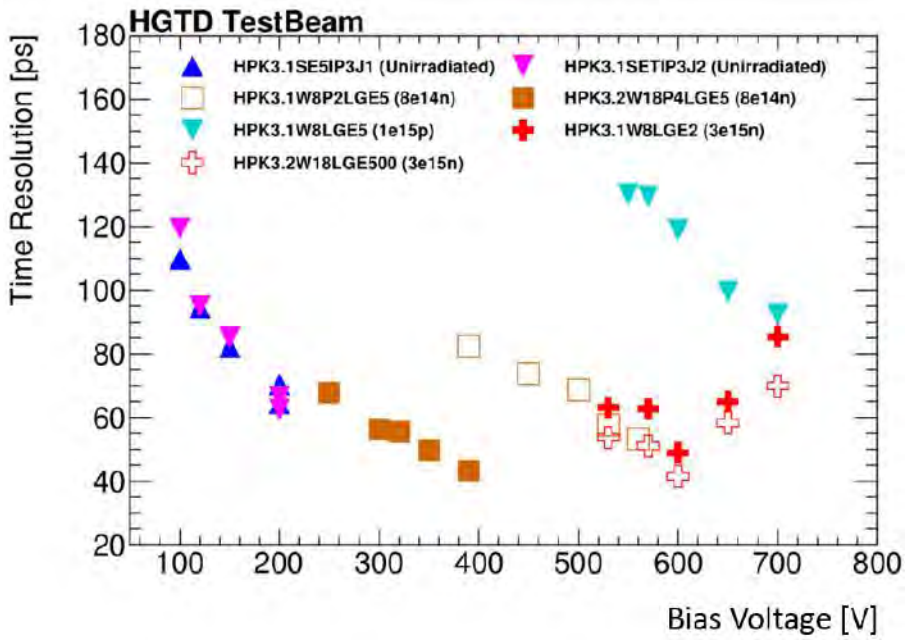

Figure 5.36: Combine plots for all HPK sensor used in HGTD test-beam Marh-2019 at DESY.

Conclusion

The High Luminosity Upgrade, which is starting in 2024, will include several upgrades in different systems, including the High Granularity Timing Detector (HGTD). The High Granularity Timing Detector covers the forward region with better radiation protection and efficiency than the Hadronic Calorimeter which was assigned for this purpose before. The HGTD is new detector that is going to collect timing information of traversing particles in the ATLAS detector at CERN. It will solve the most challenging difficulties in the upgrade, like the huge amount of pile-up and high trigger rates. To characterize the performance of the recently developed LGAD sensors for the future HGTD, three 2 $\times$ 1 pad-arrays of different sensors have been analyzed. Several properties affecting the performance in the inter-pad region have been studied with data from test beam campaigns at DESY in March-2019.

In order to get information on the behaviour of LGAD sensors in the HGTD, they must be tested in the similar conditions to the environment in which they will be used.

The data used in this analysis were collected using a beam telescope, the telescope which is EUDET type beam telescope, this is done with a test beam with energy of 5 G eV electrons to test the devices. The analysis has been done using the ROOT framework.

The first step is to plot the charge collected for all the sensors containing unirradiated and irradiated sensors, which contains the signal and background (noise). The purpose was eliminate the noise which arises from the region other than sensor. For doing this we have adopted 6 cuts, where we try to eliminate the noise without losing information from our signal. When we

removed the background we fit the signal with gaussian or Landau function. The Landau function is for interaction between the incoming particle beam with the sensor, based on the Bethe-Bloch formula.
Once the histogram has been successfully adjusted, we can choose the most probable (MPV) of charge and pulseheight. We also collected the MPVs for all the other sensors that we have studied. On comparing their amplitudes and charges we found almost same values for all sensors. For un-irradiated sensors we found that the amplitude, charge and amplitude to noise (S/N) ratios increase with increasing the bias voltage.
We also performed analysis to find the time resolution for the given sensors, the average time resolution per track about 30 ps at the beginning of the HL-LHC. From our study we found that the irradiated sensors need larger bias voltage to obtain high gain as compare to un-irradiated sensors. With larger bias voltage the time resolution of un-irradiated sensors changes more than irradiated sensors. The performance of HPK3.2W18P4LGE5(8e14n) sensors is better than all the other sensors. The larger the bias voltage, the performance of time resolution becomes better. Except batch 120X, when the bias voltage larger than 600 V, the performance becomes worse.
We can consequently conclude that the performance of un-irradiated sensors is much better than those are under irradiation. Also that when the irradiation dose increases, the performance become worse. The uncertainty becomes larger as the irradiation becomes larger, but the mean is still within error.

Appendix A

Collected Charges for Un-irradiated Sensors

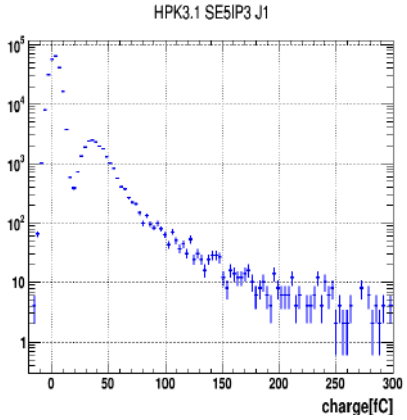

(a) Charge of HPK3.1SE5IP3J1

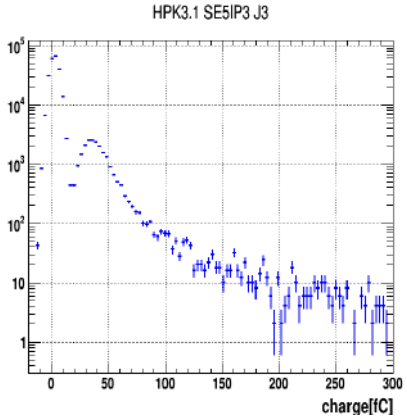

(b) Charge of HPK3.1SE5IP3J3

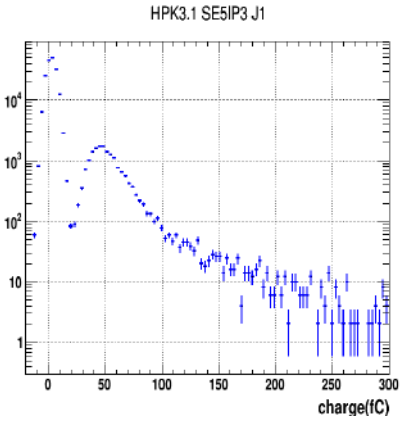

(c) Charge of HPK3.1SE5IP3J1

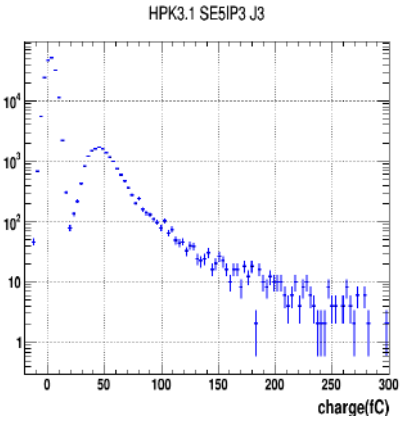

(d) Charge of HPK3.1SE5IP3J3

Figure A.1: Charge distribution for un-irradiated sensors at temperature -20^{0}C for channel 1 and 2.

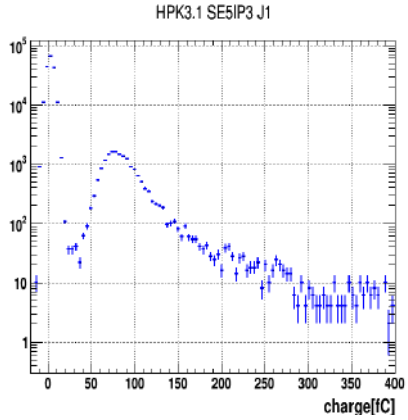

(a) Charge of HPK3.1SE5IP3J1

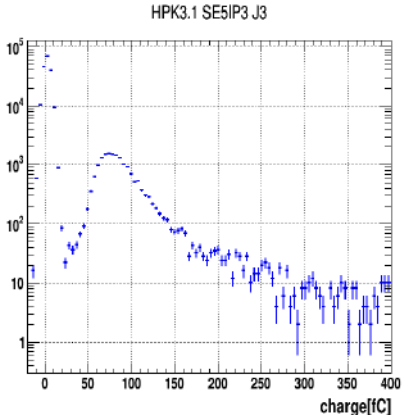

(b) Charge of HPK3.1SE5IP3J3

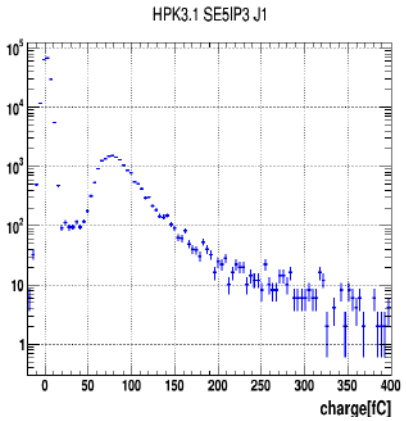

(c) Charge of HPK3.1SE5IP3J1

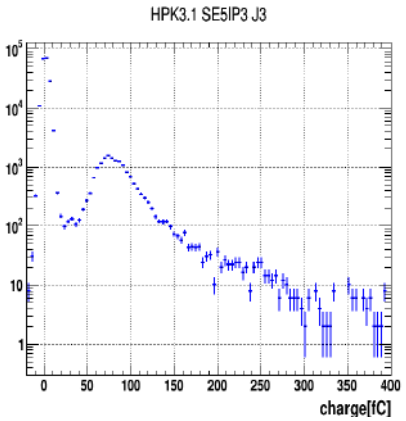

(d) Charge of HPK3.1SE5IP3J3

Figure A.2: Charge distribution for un-irradiated sensors at temperature -20^{0}C for channel 1 and 2.

A.1 Amplitude for Un-irradiated Sensors

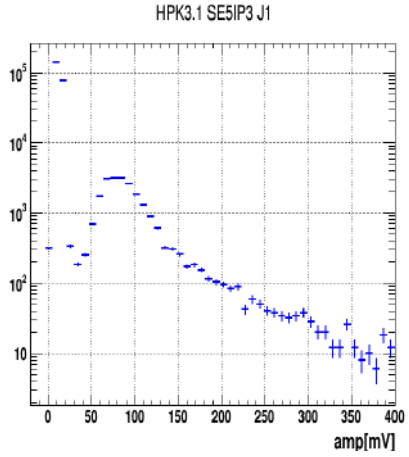

(a) Amplitude of HPK3.1SE5IP3J1

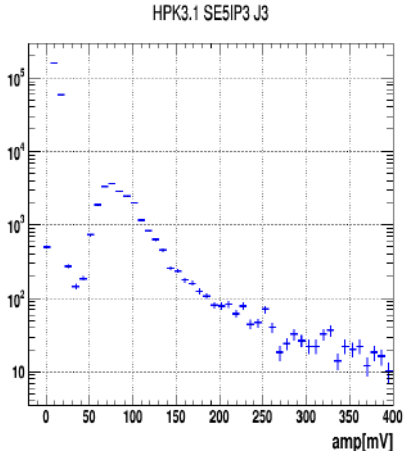

(b) Amplitude of HPK3.1SE5IP3J3

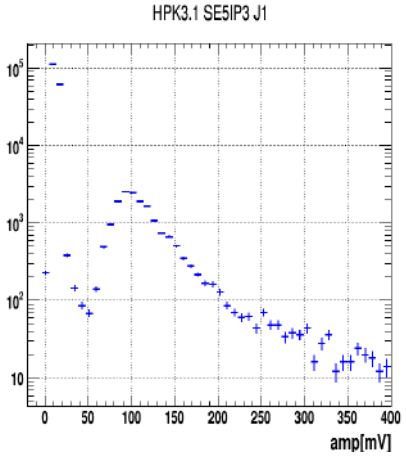

(c) Amplitude of HPK3.1SE5IP3J1

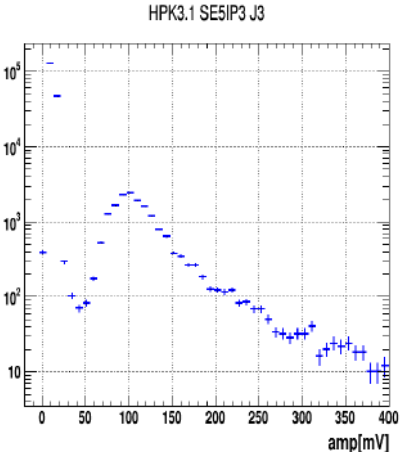

(d) Amplitude of HPK3.1SE5IP3J3

Figure A.3: Amplitude of un-irradiated HPK sensors for batch 102, batch 103 at channel 1 and channel 2.

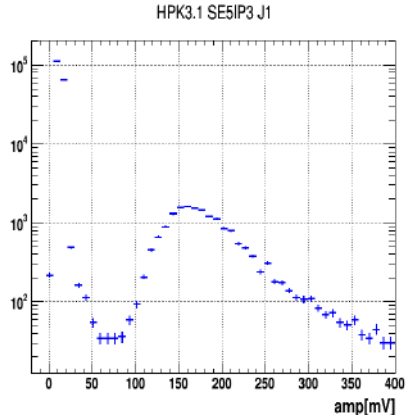

(a) Amplitude of HPK3.1SE5IP3J1

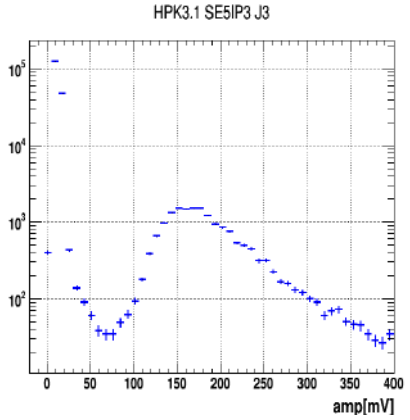

(b) Amplitude of HPK3.1SE5IP3J3

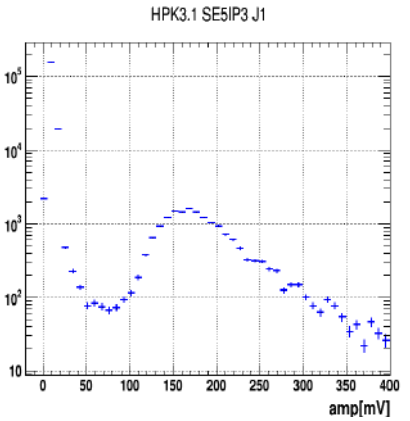

(c) Amplitude of HPK3.1SE5IP3J1

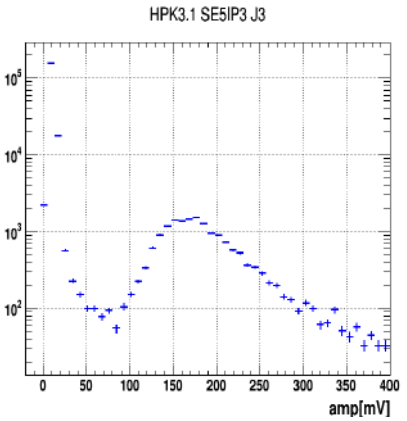

(d) Amplitude of HPK3.1SE5IP3J3

Figure A.4: Amplitude of un-irradiated HPK sensors at temperature -20^{0}C for batch 104, batch 105 at channel 1 and channel 2.

Appendix B

Charge For Irradiated Sensors

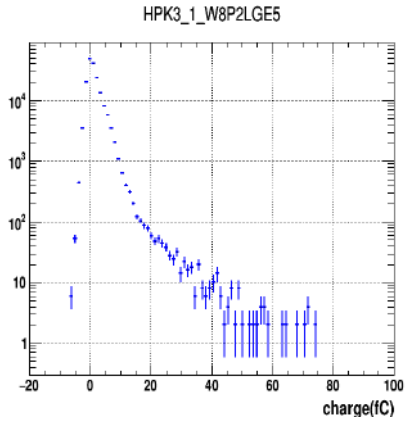

(a) Charge of HPK3.1W8P2LGE5

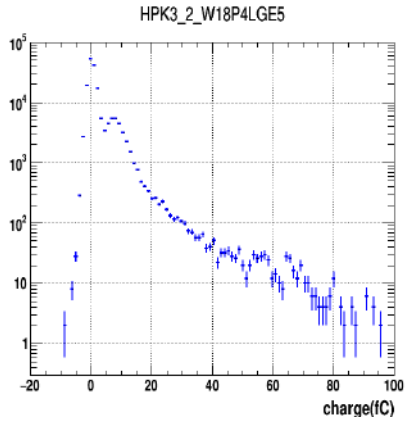

(b) Charge of HPK3.2W18P4LGE5

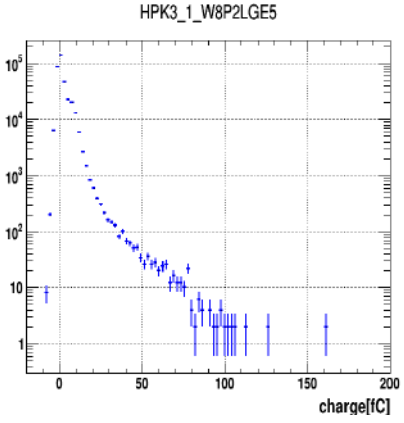

(c) Charge of HPK3.1W8P2LGE5

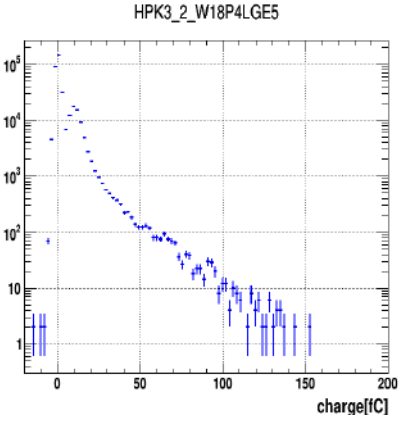

(d) Charge of HPK3.2W18P4LGE5

Figure B.1: Charge distribution for two irradiated HPK sensors at channel 1 and channel 2.

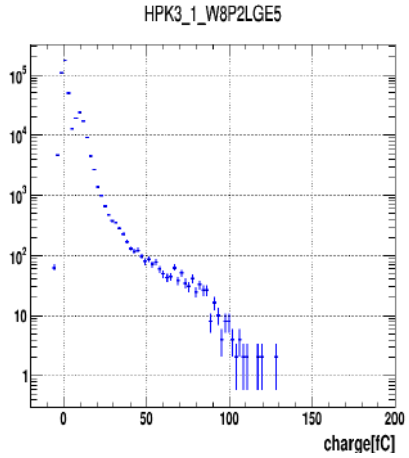

(a) Charge of HPK3.1W8P2LGE5

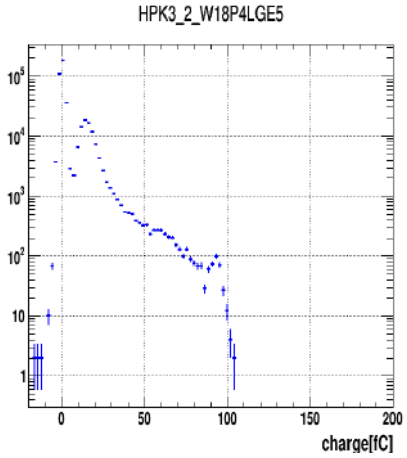

(b) Charge of HPK3.2W18P4LGE5

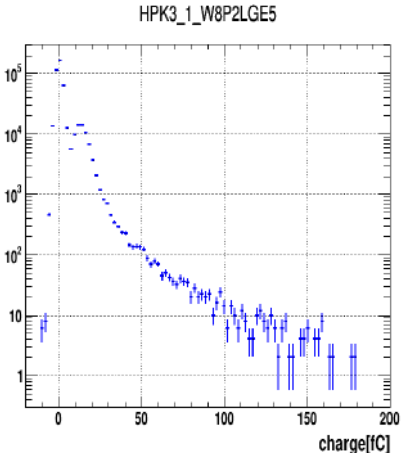

(c) Charge of HPK3.1W8P2LGE5

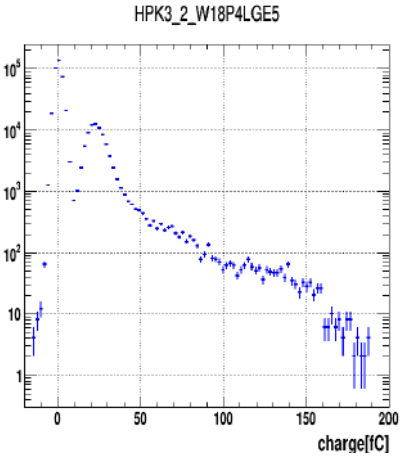

(d) Charge of HPK3.2W18P4LGE5

Figure B.2: Charge distribution of irradiated HPK sensors at channel 1 and channel 2.

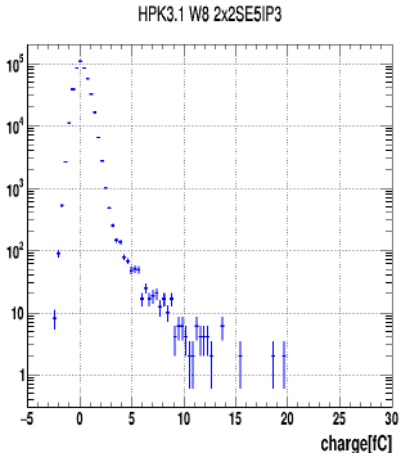

(a) Charge of HPK3.1W82×2SE5IP3

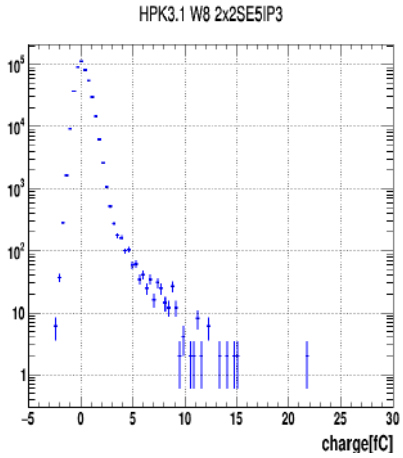

(b) Charge of HPK3.1W82×2SE5IP3

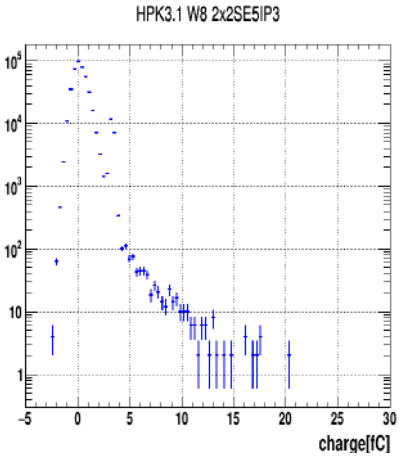

(c) Charge of HPK3.1W82×2SE5IP3

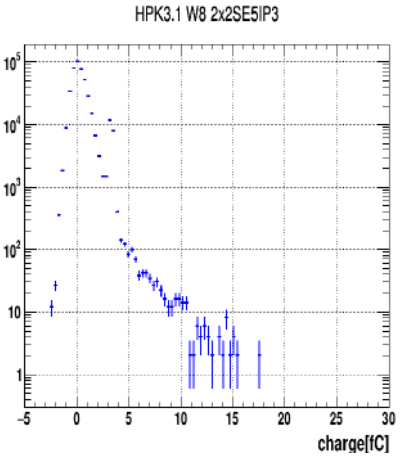

(d) Charge of HPK3.1W82×2SE5IP3

Figure B.3: Charge distribution of irradiated HPK sensors for batch 702, batch 702 at channel 1 and channel 2.

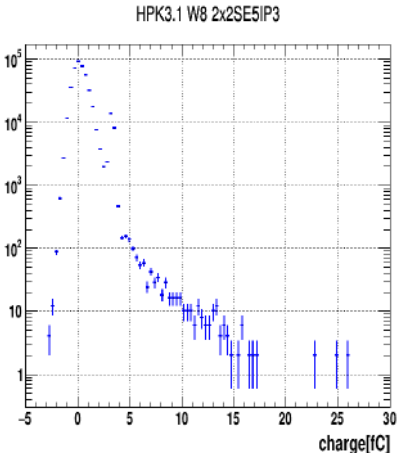

(a) Charge of HPK3.1W82×2SE5IP3

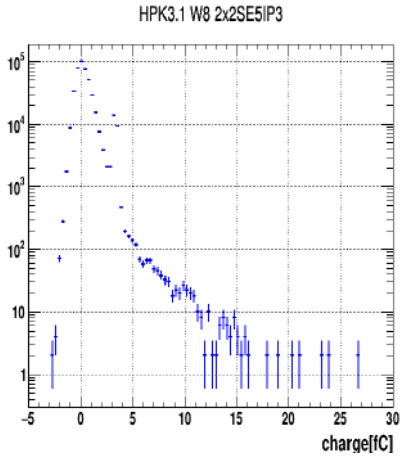

(b) Charge of HPK3.1W82×2SE5IP3

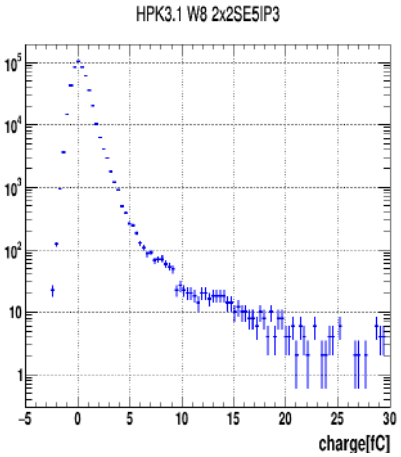

(c) Charge of HPK3.1W82×2SE5IP3

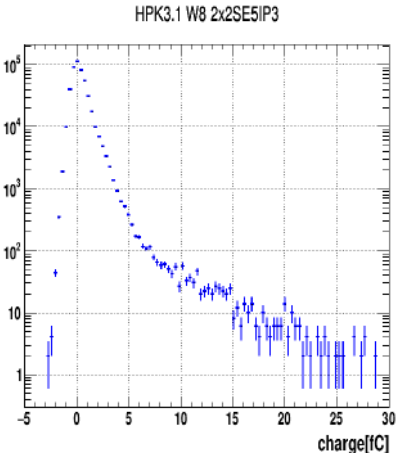

(d) Charge of HPK3.1W82×2SE5IP3

Figure B.4: Charge distribution of irradiated HPK sensors for batch 704, batch 705 at channel 1 and channel 2.

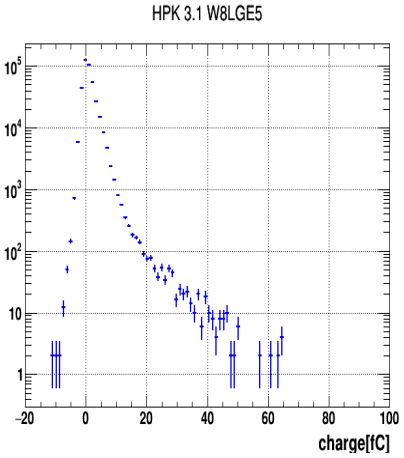

(a) Charge for HPK3.1W8LGE5

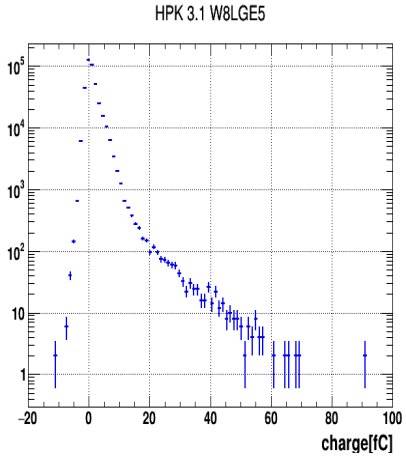

(b) Charge for HPK3.1W8LGE5

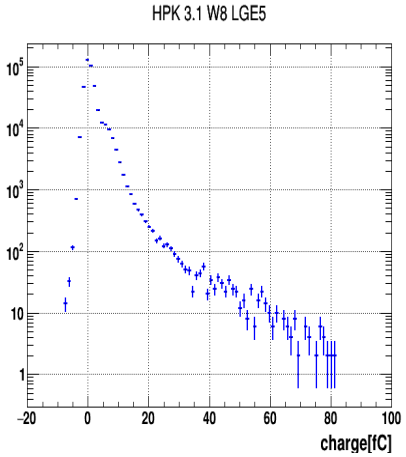

(c) Charge for HPK3.1W8LGE5

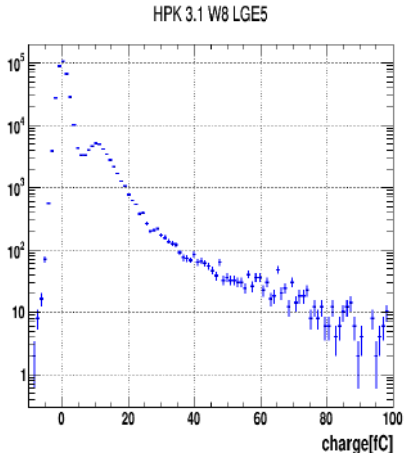

(d) Charge for HPK3.1W8LGE5

Figure B.5: Charge distribution of irradiated HPK sensor for batch 1102, batch 1105 placed at channel 1.

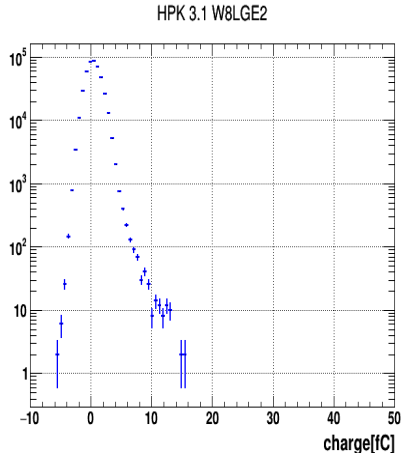

(a) Charge collected by HPK3.1W8LGE2

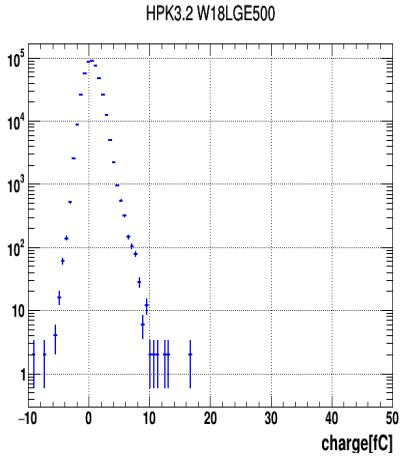

(b) Charge collected by HPK3.2W18LGE500

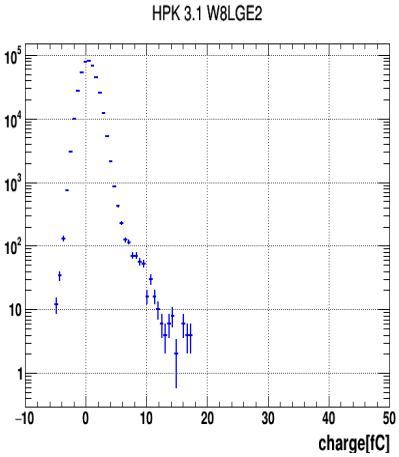

(c) Charge collected by HPK3.1W8LGE2

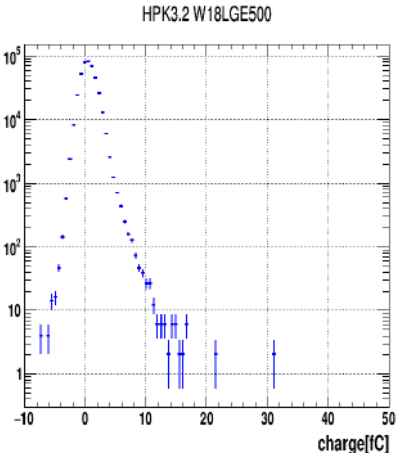

(d) Charge collected by HPK3.2W18LGE500

Figure B.6: Charge distribution of irradiated HPK sensors for batch 1202, batch 1203 at channel 1 and channel 2.

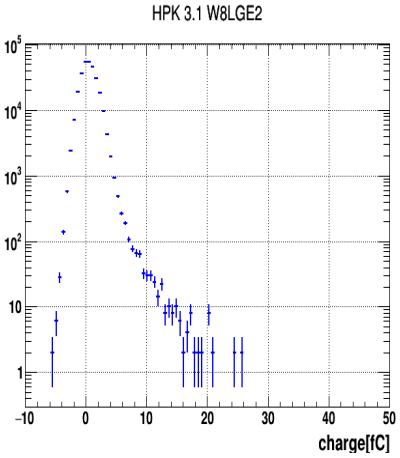

(a) Charge collected by HPK3.1W8LGE2

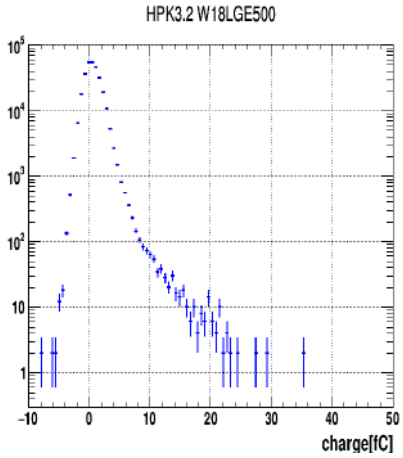

(b) Charge collected by HPK3.2W18LGE500

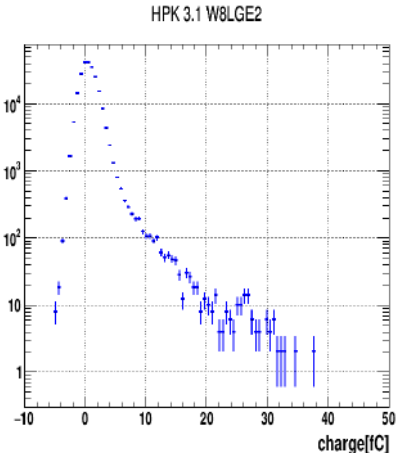

(c) Charge collected by HPK3.1W8LGE2

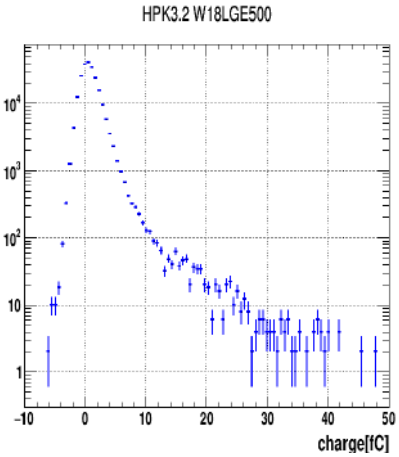

(d) Charge collected by HPK3.2W18LGE500

Figure B.7: Charge distribution of irradiated HPK sensors for batch 1204, batch 1205 placed at channel 1 and channel 2.

B.1 Amplitude Of Irradiated HPK Sensors

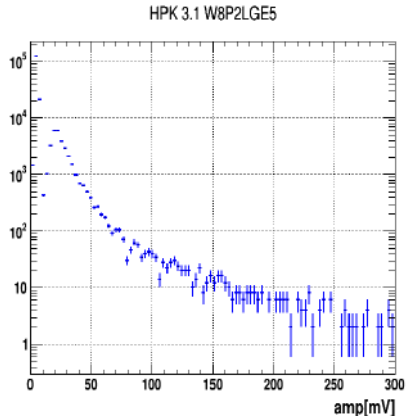

(a) Amplitude of sensor HPK3.1W8P2LGE5

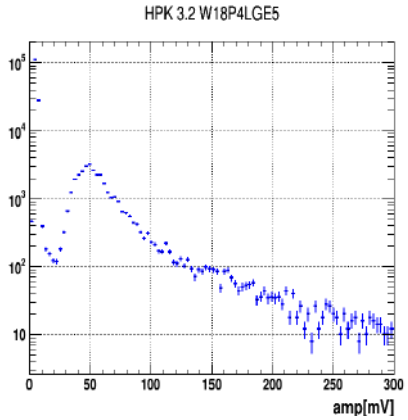

(b) Amplitude of sensor HPK3.2W18P4LGE5

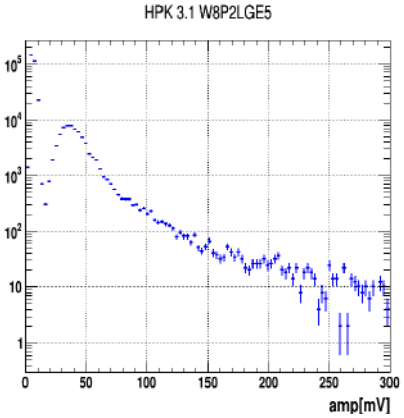

(c) Amplitude of sensor HPK3.1W8P2LGE5

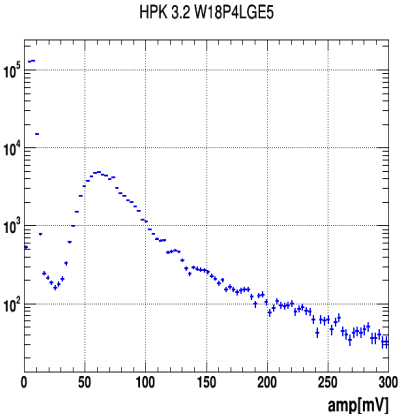

(d) Amplitude of sensor HPK3.2W18P4LGE5

Figure B.8: Amplitude of irradiated HPK sensors for batch 602, batch 603 at channel 1 and channel 2.

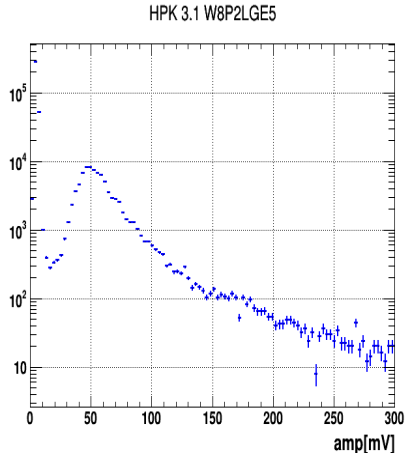

(a) Amplitude of sensor HPK3.1W8P2LGE5

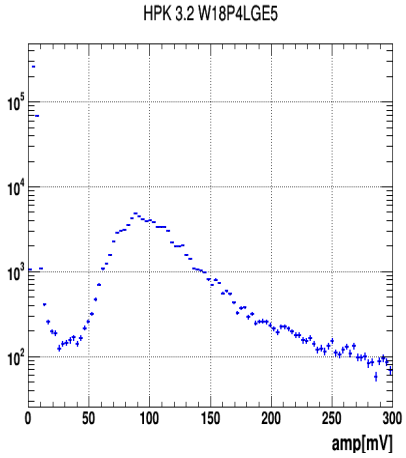

(b) Amplitude of sensor HPK3.2W18P4LGE5

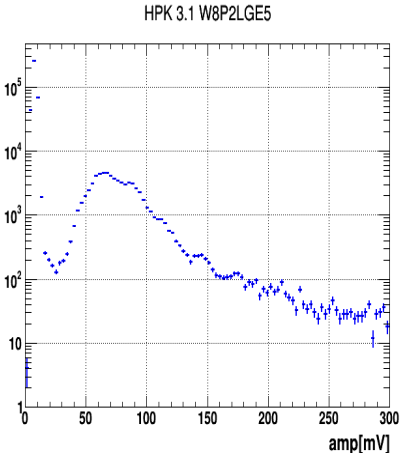

(c) Amplitude of sensor HPK3.1W8P2LGE5

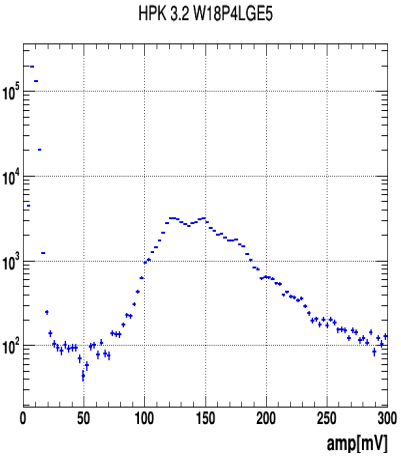

(d) Amplitude of sensor HPK3.2W18P4LGE5

Figure B.9: Amplitude of irradiated HPK sensors for batch 603, batch 605 at channel 1 and channel 2.

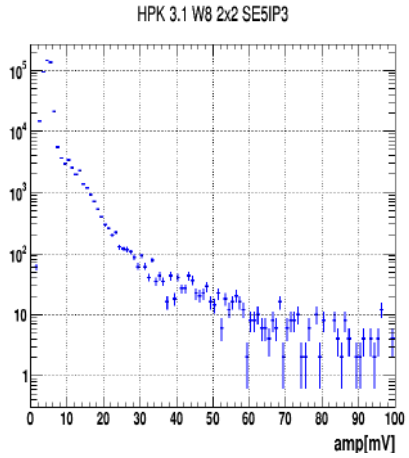

(a) HPK3.1W82×2SE5IP3 sensor amplitude

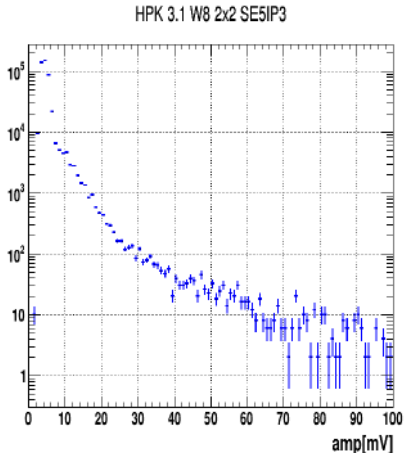

(b) HPK3.1W82×2SE5IP3 sensor amplitude

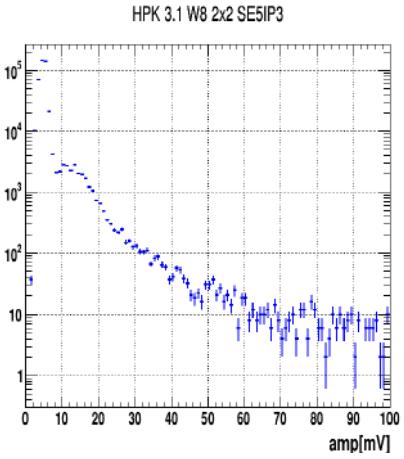

(c) HPK3.1W82×2SE5IP3 sensor amplitude

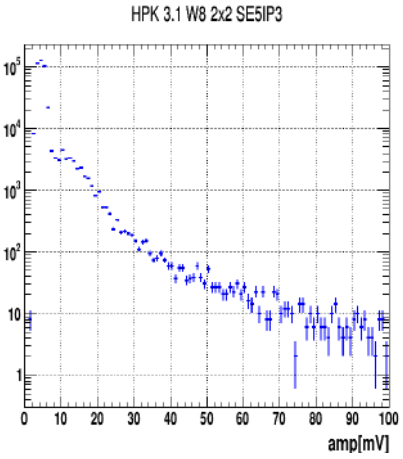

(d) HPK3.1W82×2SE5IP3 sensor amplitude

Figure B.10: Amplitude of irradiated HPK sensors for batch 702, batch 703 at channel 1 and channel 2.

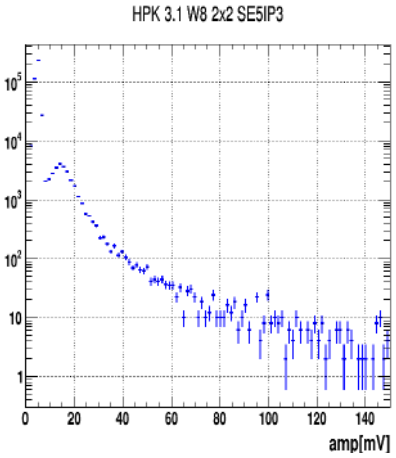

(a) HPK3.1W82×2SE5IP3 sensor amplitude

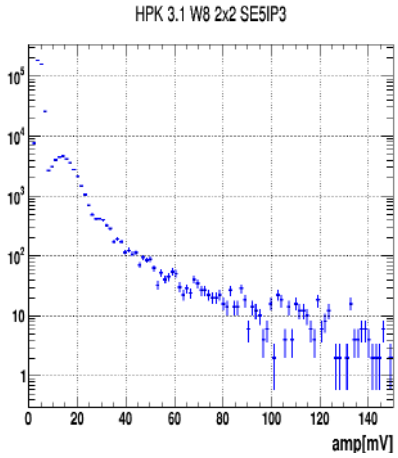

(b) HPK3.1W82×2SE5IP3 sensor amplitude

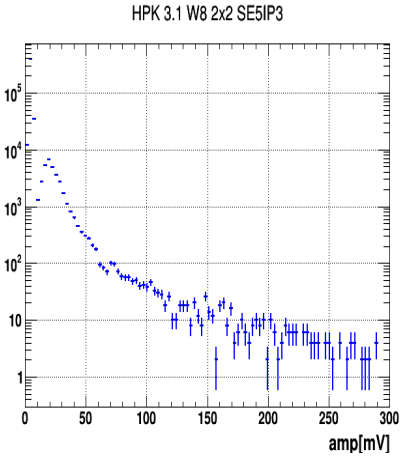

(c) HPK3.1W82×2SE5IP3 sensor amplitude

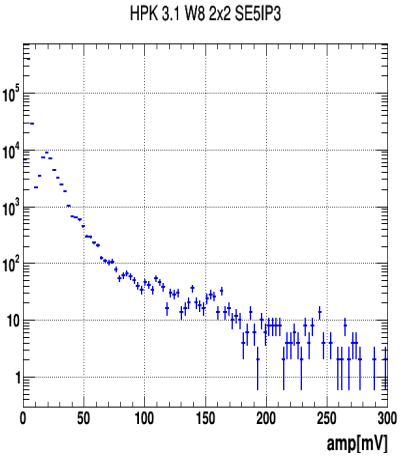

(d) HPK3.1W82×2SE5IP3 sensor amplitude

Figure B.11: Amplitude of irradiated HPK sensors for batch 704, batch 705 at channel 1 and channel 2.

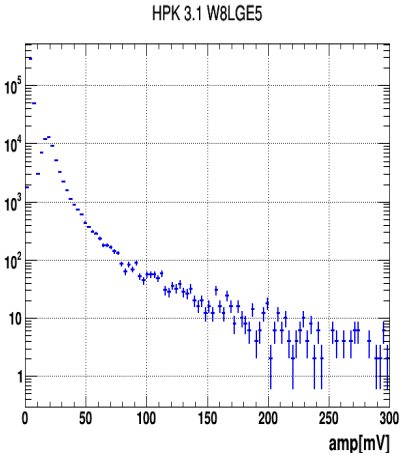

(a) HPK3.1W8LGE5 sensor amplitude

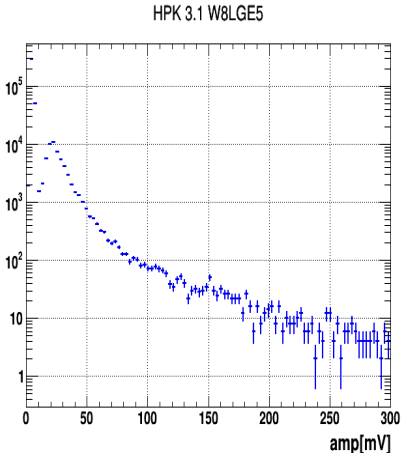

(b) HPK3.1W8LGE5 sensor amplitude

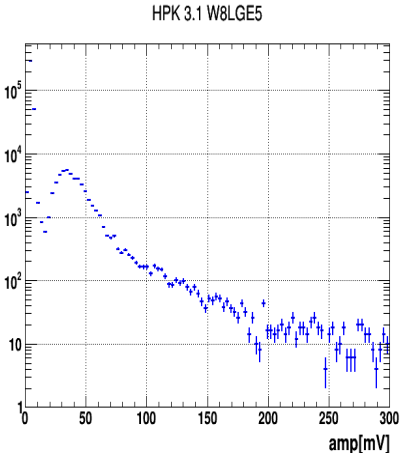

(c) HPK3.1W8LGE5 sensor amplitude

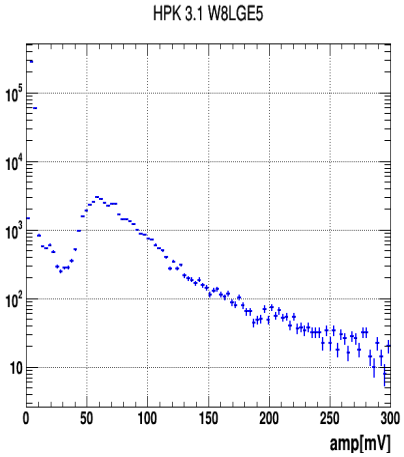

(d) HPK3.1W8LGE5 sensor amplitude

Figure B.12: Amplitude of irradiated HPK sensors for batch 1102 to batch 1105 placed at channel 1.

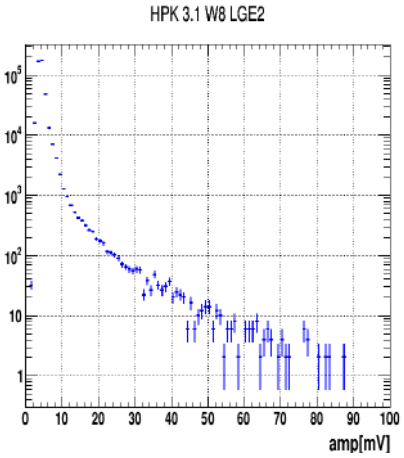

(a) HPK3.1W18LGE2 sensor amplitude

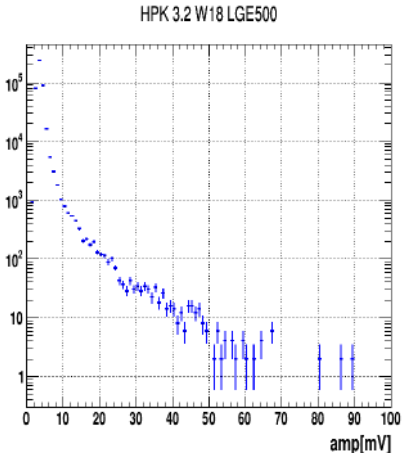

(b) HPK3.2W18LGE500 sensor amplitude

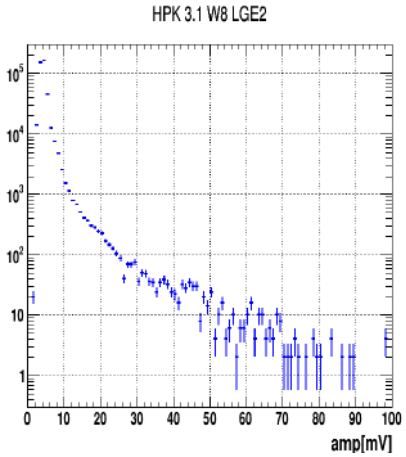

(c) HPK3.1W18LGE2 sensor amplitude

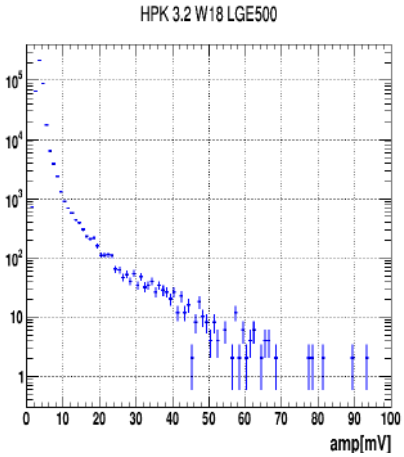

(d) HPK3.2W18LGE500 sensor amplitude

Figure B.13: Amplitude of irradiated HPK sensors for batch 1202, batch 1203 at channel 1 and channel 2.

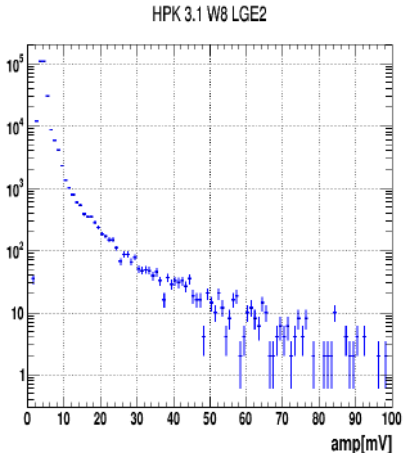

(a) HPK3.1W18LGE2 sensor amplitude

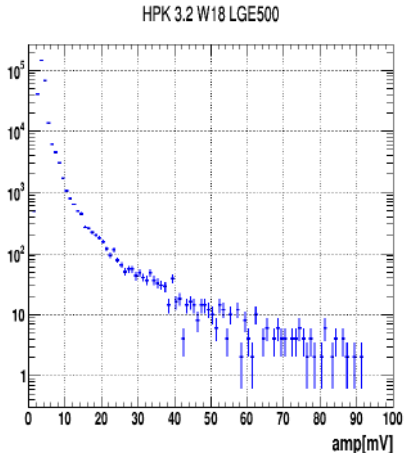

(b) HPK3.2W18LGE500 sensor amplitude

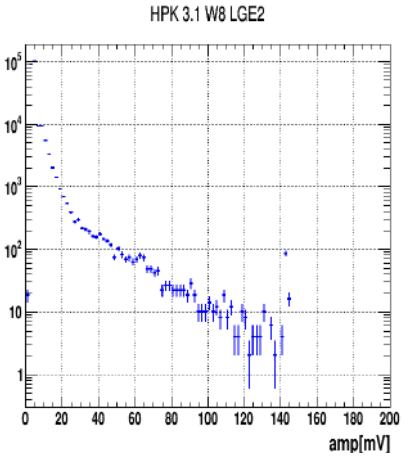

(c) HPK3.1W18LGE2 sensor amplitude

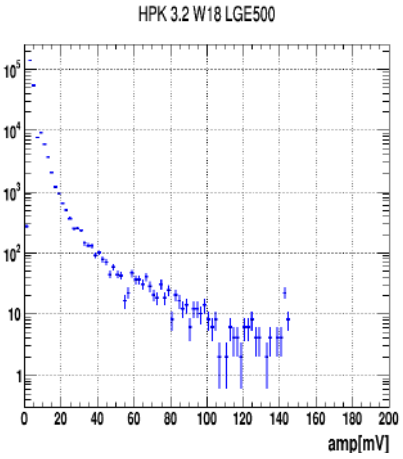

(d) HPK3.2W18LGE500 sensor amplitude

Figure B.14: Amplitude of irradiated HPK sensors for batch 1204, batch 1205 at channel 1 and channel 2.

Appendix C

Fitting Function For Charge

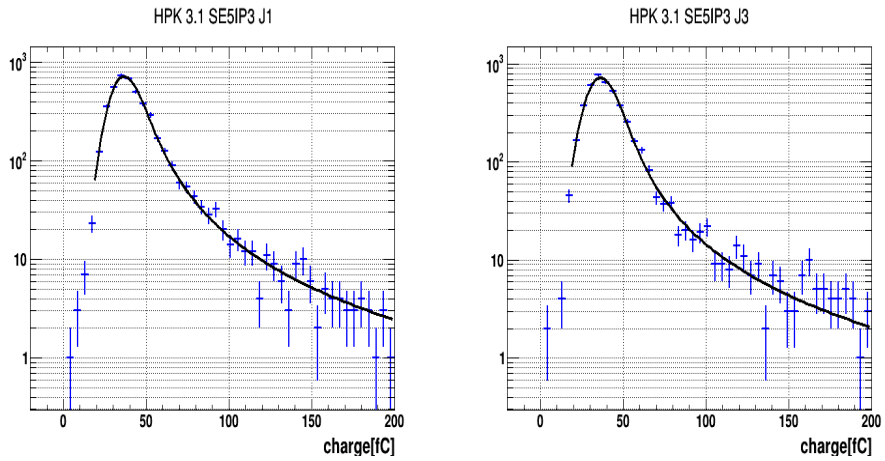

(a) HPK3.1SE5IP3J1 charge with fitting function

(b) HPK3.1SE5IP3J3 charge with fitting function

Figure C.1: Charge distribution for batch 102 channel 1, channel 2 using un-irradiated HPK sensors and fitted with (landau, gauss) function.

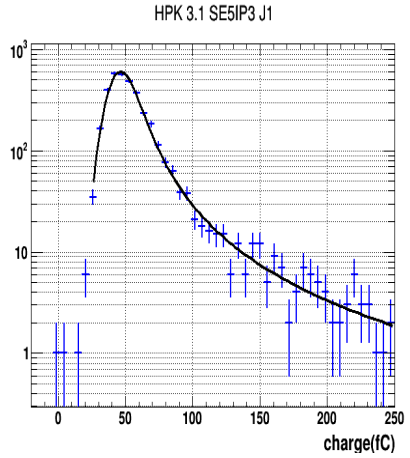

(a) HPK3.1SE5IP3J1 charge with fitting function

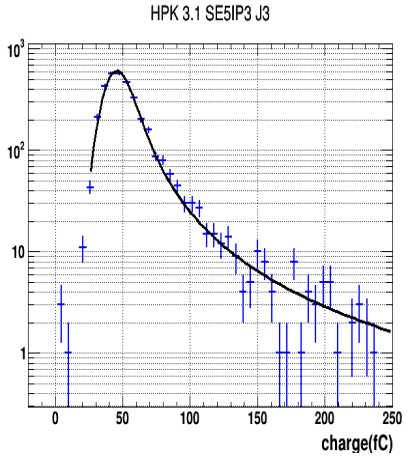

(b) HPK3.1SE5IP3J3 charge with fitting function

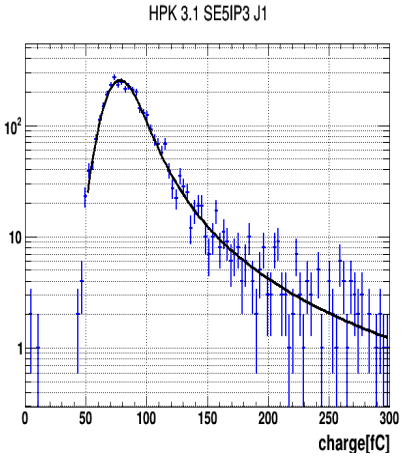

(c) HPK3.1SE5IP3J1 charge with fitting function

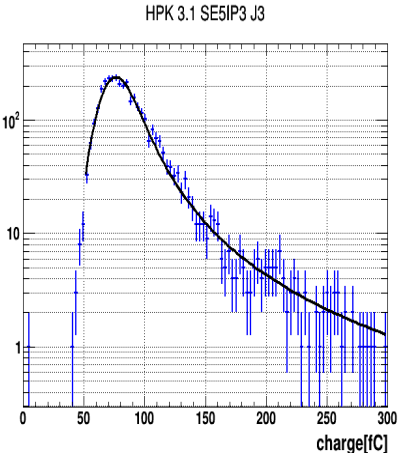

(d) HPK3.1SE5IP3J3 charge with fitting function

Figure C.2: Charge distribution for batch 103 and batch 104 channel 1, channel 2 using un-irradiated HPK sensors and fitted with (landau, gauss) function.

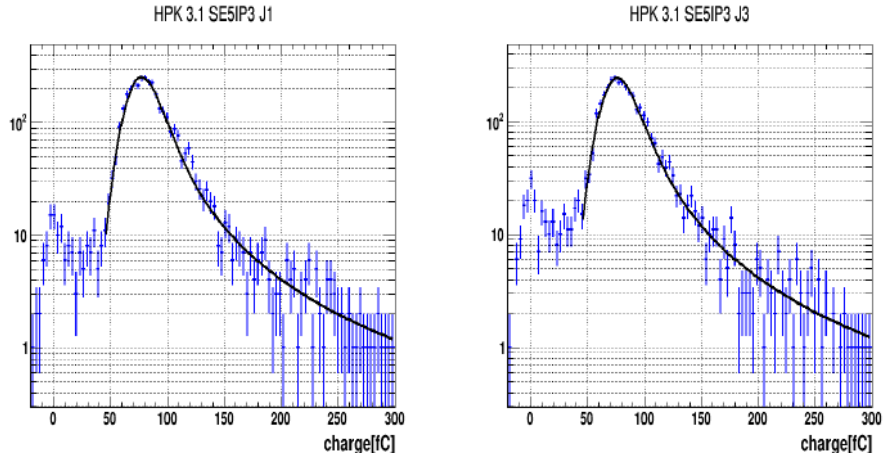

(a) HPK3.1SE5IP3J1 charge with fitting function

(b) HPK3.1SE5IP3J3 charge with fitting function

Figure C.3: Charge distribution for batch 105 channel 1, channel 2 using un-irradiated HPK sensors and fitted with (landau, gauss) function.

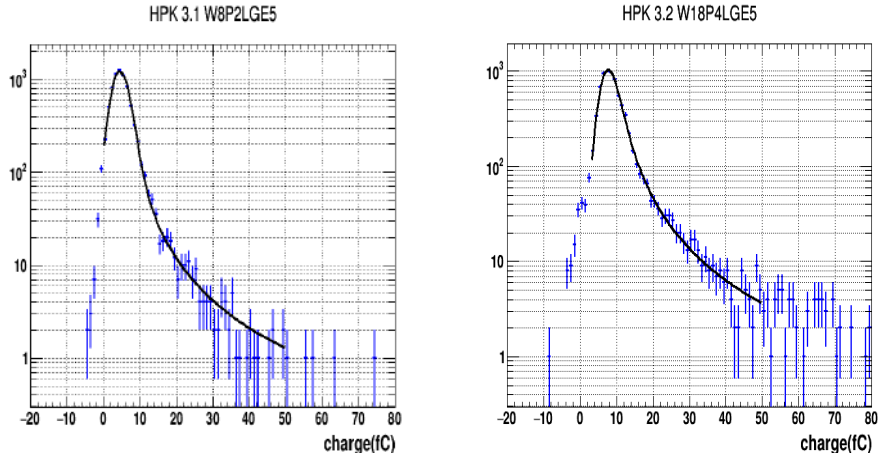

(a) HPK3.1W8P2LGE5 charge with fitting function

(b) HPK3.2W18P4LGE5 charge with fitting function

Figure C.4: Charge distribution for batch 602 channel 1, channel 2 using irradiated HPK sensors and fitted with (landau, gauss) function.

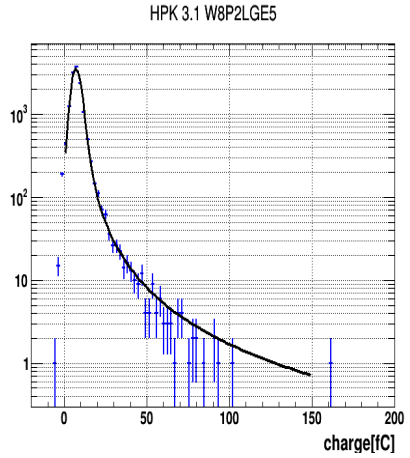

(a) HPK3.1W8P2LGE5 charge with fitting function

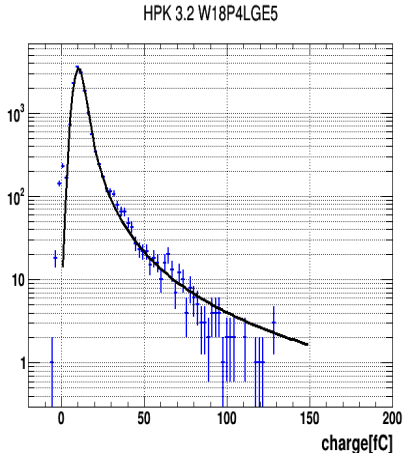

(b) HPK3.2W18P4LGE5 charge with fitting function

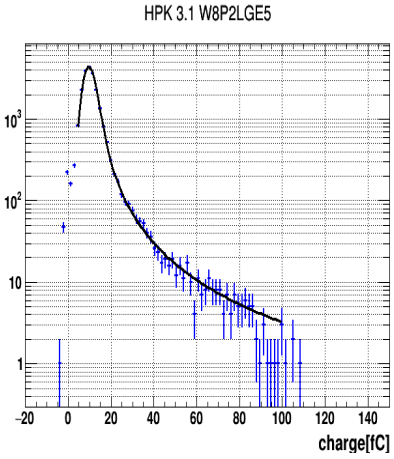

(c) HPK3.1W8P2LGE5 charge with fitting function

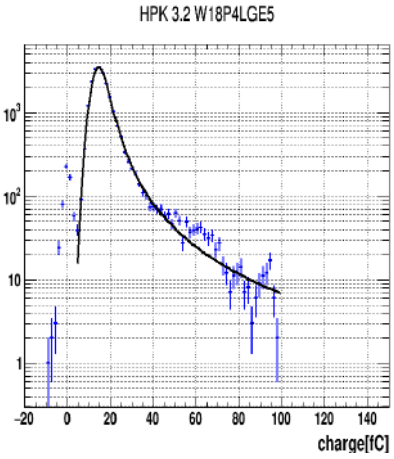

(d) HPK3.2W18P4LGE5 charge with fitting function

Figure C.5: Charge distribution for batch 603, batch 604 channel 1, channel 2 using irradiated HPK sensors and fitted with (landau, gauss) function.

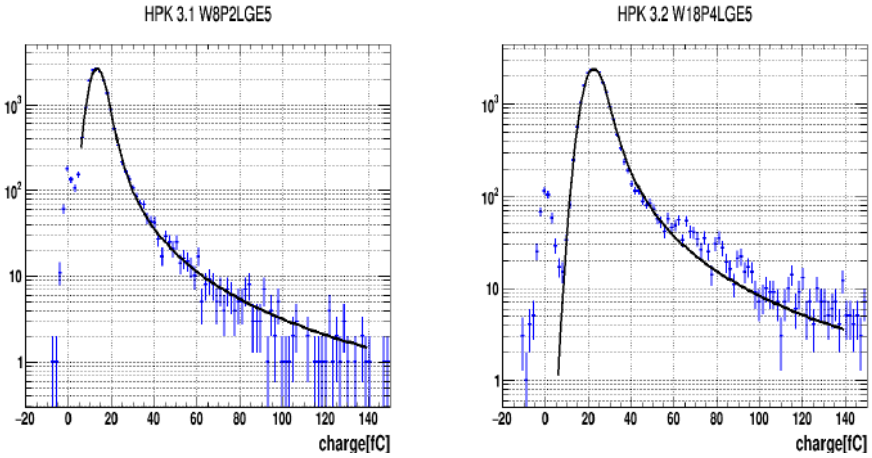

(a) HPK3.1W8P2LGE5 charge with fitting function

(b) HPK3.2W18P4LGE5 charge with fitting function

Figure C.6: Charge distribution for batch 605 channel 1, channel 2 using irradiated HPK sensors and fitted with (landau, gauss) function.

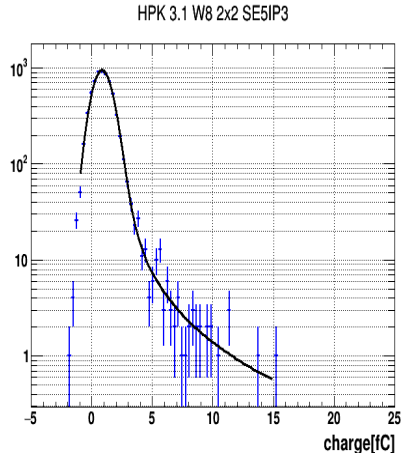

(a) HPK3.1W82×2SE5IP3 charge with fitting function

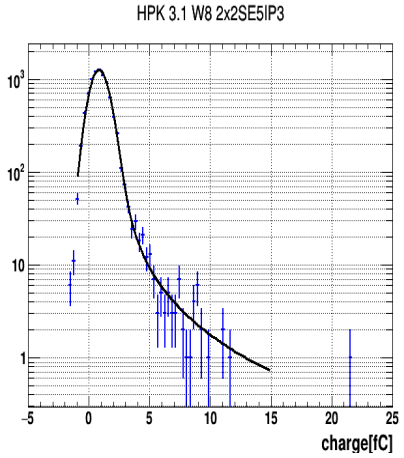

(b) HPK3.1W82×2SE5IP3 charge with fitting function

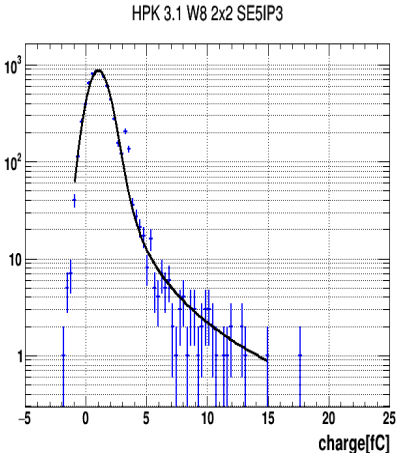

(c) HPK3.1W82×2SE5IP3 charge with fitting function

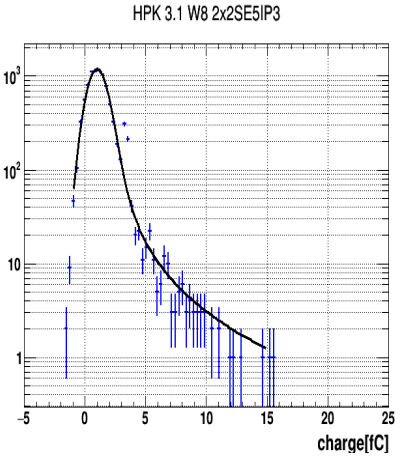

(d) HPK3.1W82×2SE5IP3 charge with fitting function

Figure C.7: Charge distribution for batch 702, batch 703 channel 1, channel 2 using irradiated HPK sensors and fitted with (landau, gauss) function.

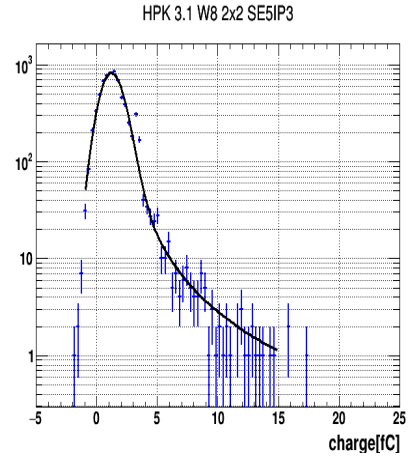

(a) HPK3.1W82×2SE5IP3 charge with fitting function

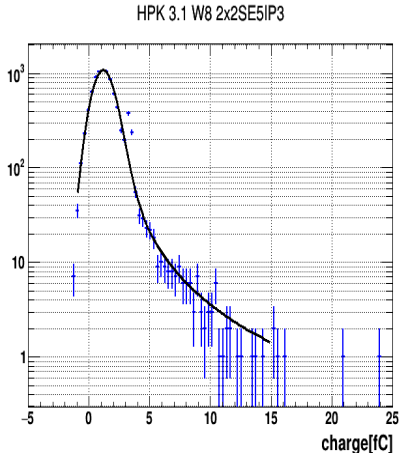

(b) HPK3.1W82×2SE5IP3 charge with fitting function

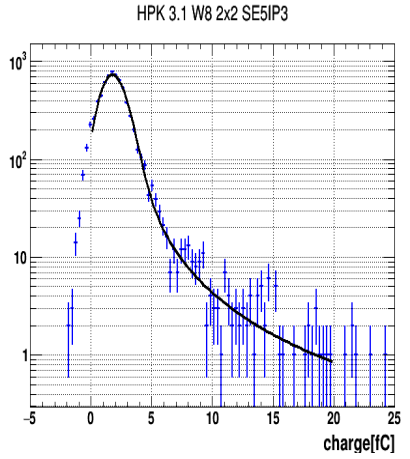

(c) HPK3.1W82×2SE5IP3 charge with fitting function

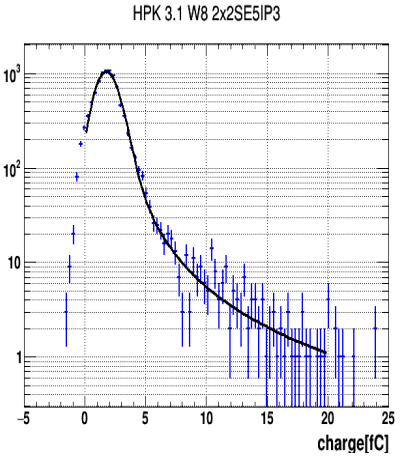

(d) HPK3.1W82×2SE5IP3 charge with fitting function

Figure C.8: Charge distribution for batch 704, batch 705 channel 1, channel 2 using irradiated HPK sensors and fitted with (landau, gauss) function.

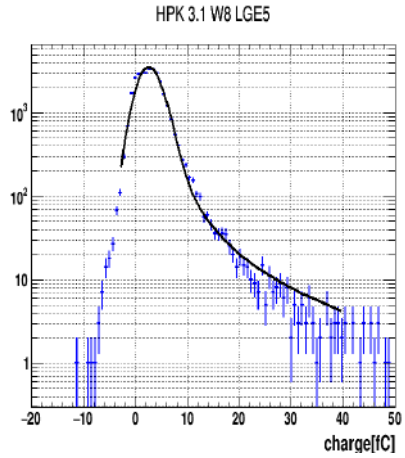

(a) HPK3.1W8LGE5 charge with fitting function

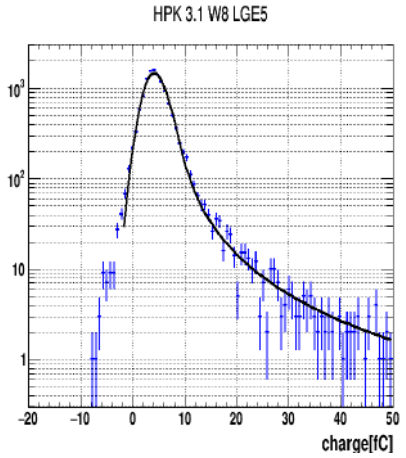

(b) HPK3.1W8LGE5 charge with fitting function

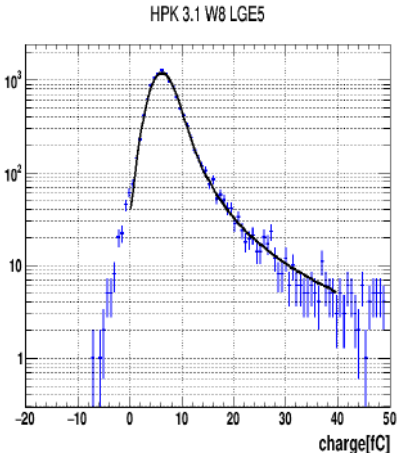

(c) HPK3.1W8LGE5 charge with fitting function

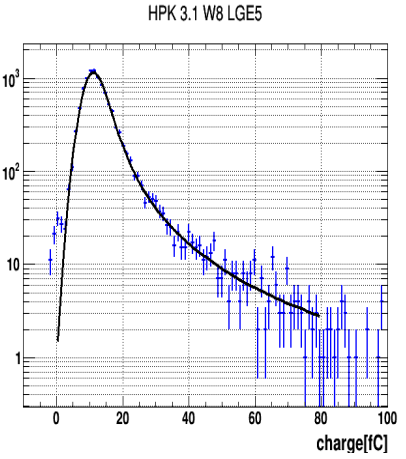

(d) HPK3.1W8LGE5 charge with fitting function

Figure C.9: Charge distribution for batch 1102 to batch 1105 channel 1, channel 2 using irradiated HPK sensors and fitted with (landau, gauss) function.

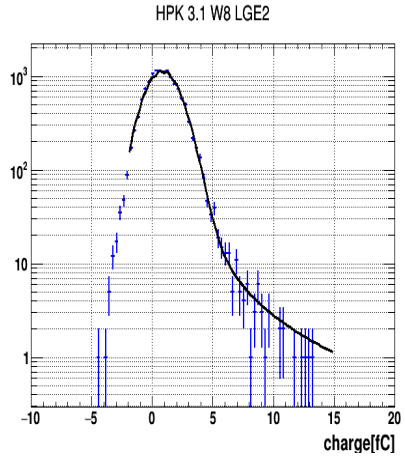

(a) HPK3.1W8LGE2 charge with fitting function

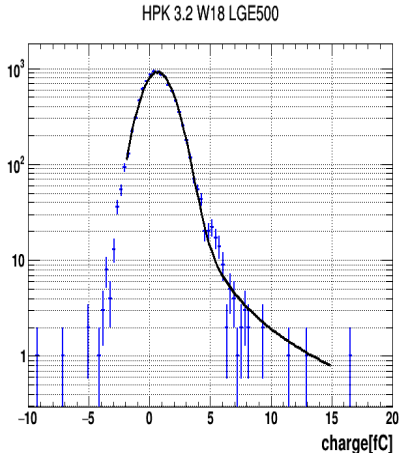

(b) HPK3.2W18LGE500 charge with fitting function

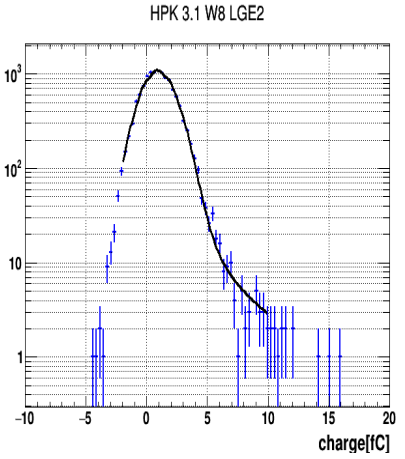

(c) HPK3.1W8LGE2 charge with fitting function

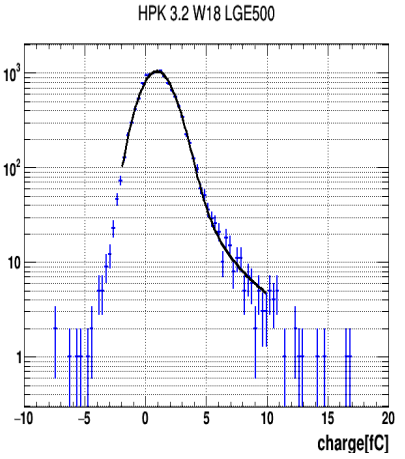

(d) HPK3.2W18LGE500 charge with fitting function

Figure C.10: Charge distribution for batch 1202, batch 1203 channel 1, channel 2 using irradiated HPK sensors and fitted with (landau, gauss) function.

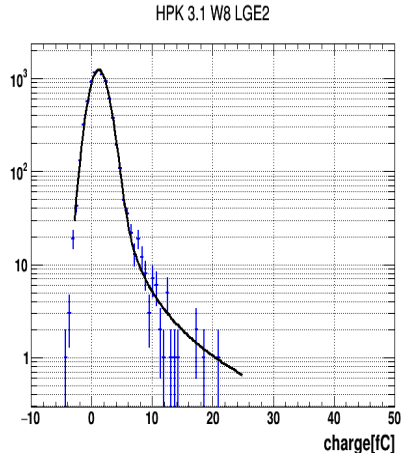

(a) HPK3.1W8LGE2 charge with fitting function

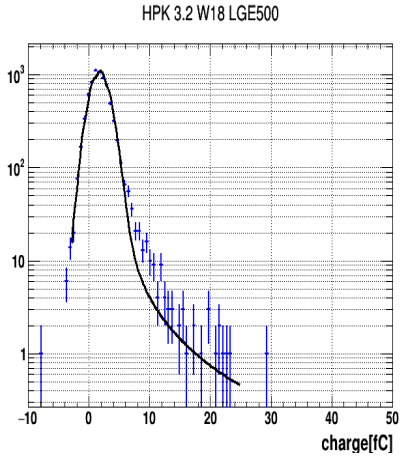

(b) HPK3.2W18LGE500 charge with fitting function

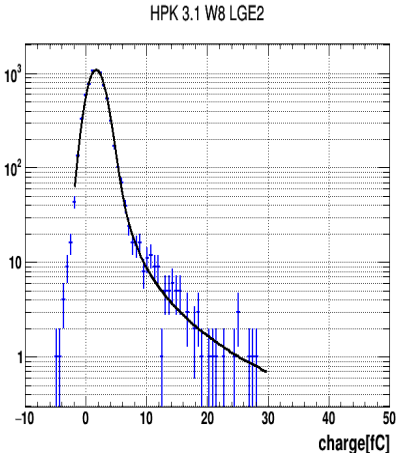

(c) HPK3.1W8LGE2 charge with fitting function

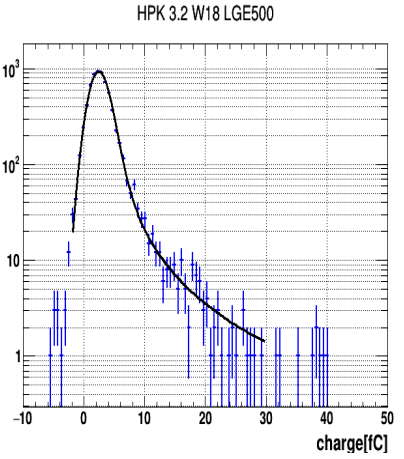

(d) HPK3.2W18LGE500 charge with fitting function

Figure C.11: Charge distribution for batch 1204, batch 1205 channel 1, channel 2 using irradiated HPK sensors and fitted with (landau, gauss) function.

C.1 Fitting Function For Amplitude

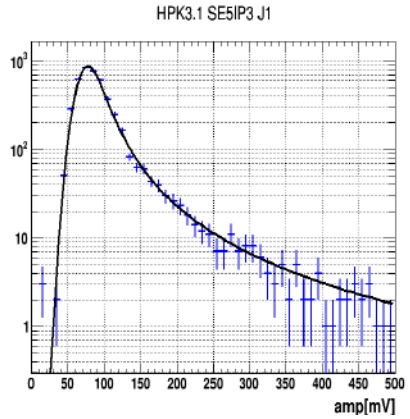

(a) HPK3.1SE5IP3J1 amplitude with fitting function

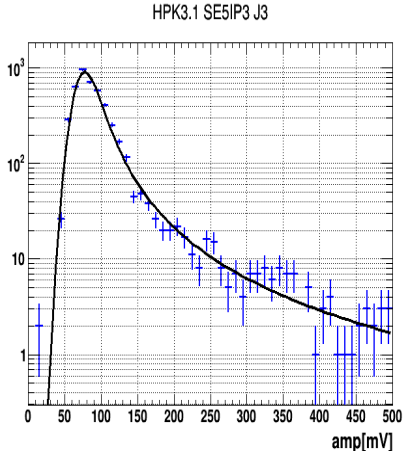

(b) HPK3.1SE5IP3J3 amplitude with fitting function

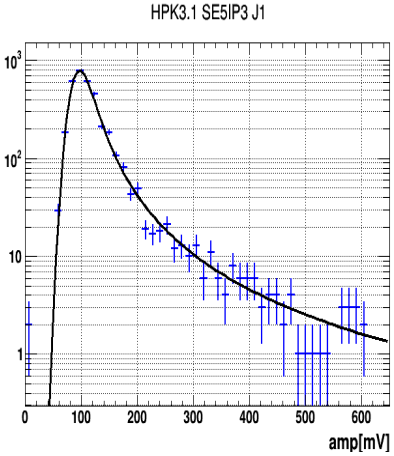

(c) HPK3.1SE5IP3J1 amplitude with fitting function

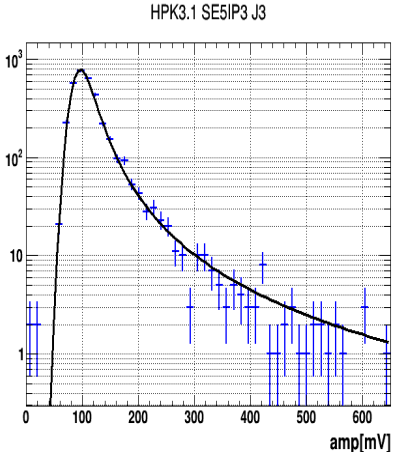

(d) HPK3.1SE5IP3J3 amplitude with fitting function

Figure C.12: Amplitude for batch 102, batch 103 channel 1, channel 2 using un-irradiated HPK sensors and fitted with (landau, gauss) function.

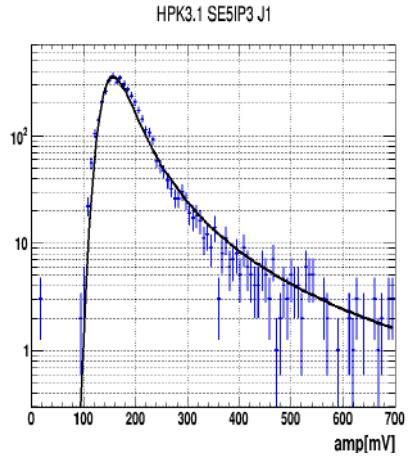

(a) HPK3.1SE5IP3J1 amplitude with fitting function

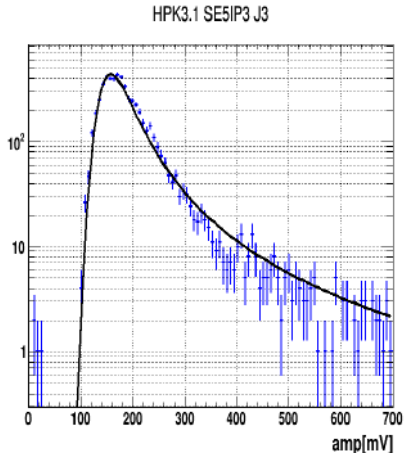

(b) HPK3.1SE5IP3J3 amplitude with fitting function

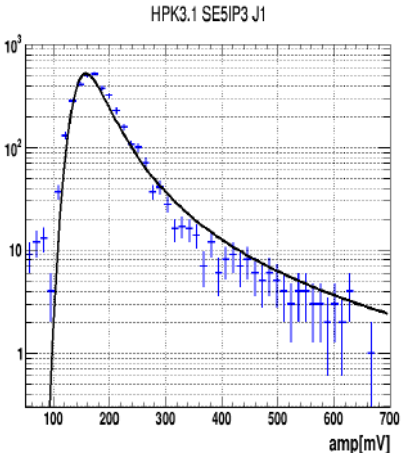

(c) HPK3.1SE5IP3J1 amplitude with fitting function

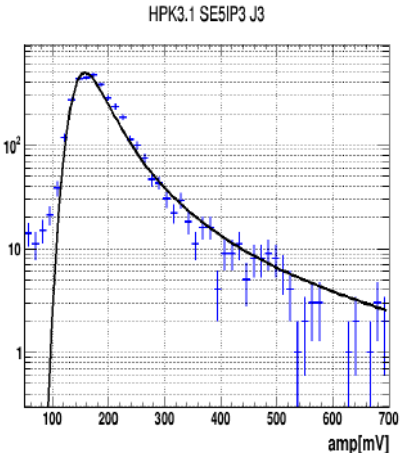

(d) HPK3.1SE5IP3J3 amplitude with fitting function

Figure C.13: Amplitude for batch 104, batch 105 channel 1, channel 2 using un-irradiated HPK sensors and fitted with (landau, gauss) function.

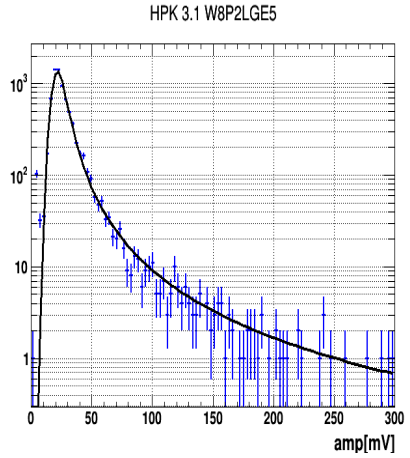

(a) HPK3.1W8P2LGE5 amplitude with fitting function

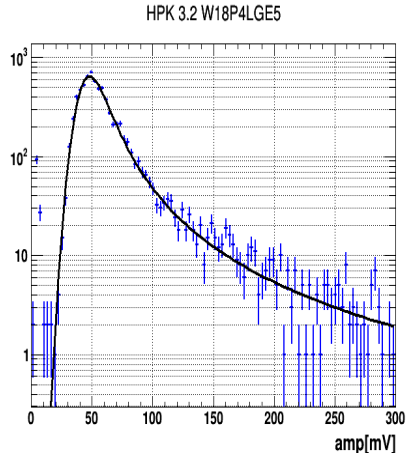

(b) HPK3.2W18P4LGE5 amplitude with fitting function

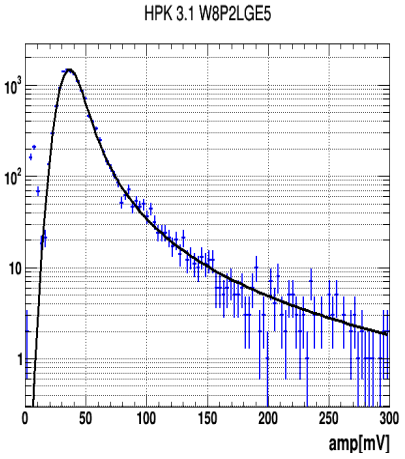

(c) HPK3.1W8P2LGE5 amplitude with fitting function

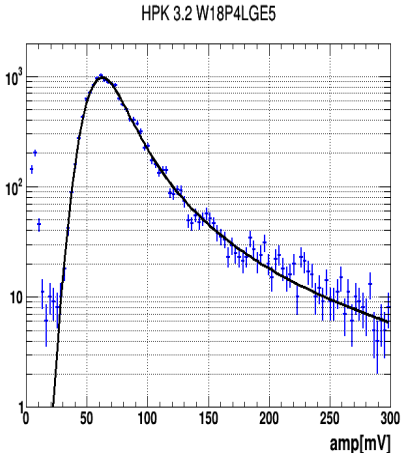

(d) HPK3.2W18P4LGE5 amplitude with fitting function

Figure C.14: Amplitude for batch 602, batch 603 channel 1, channel 2 using irradiated HPK sensors and fitted with (landau, gauss) function.

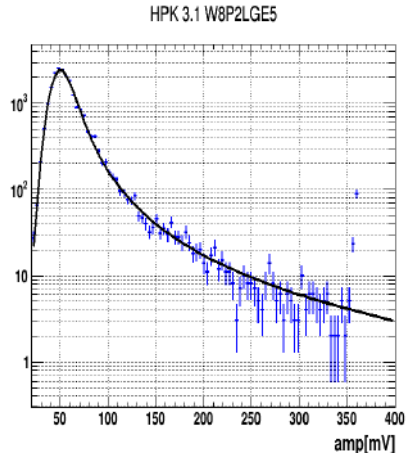

(a) HPK3.1W8P2LGE5 amplitude with fitting function

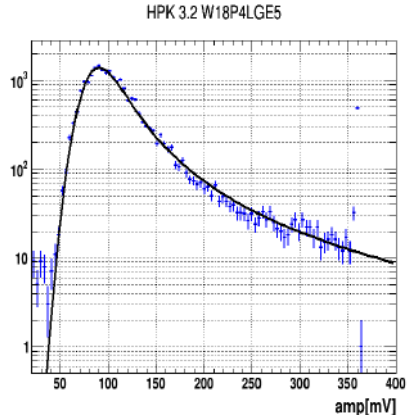

(b) HPK3.2W18P4LGE5 amplitude with fitting function

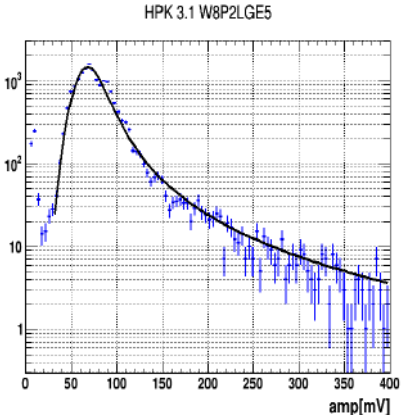

(c) HPK3.1W8P2LGE5 amplitude with fitting function

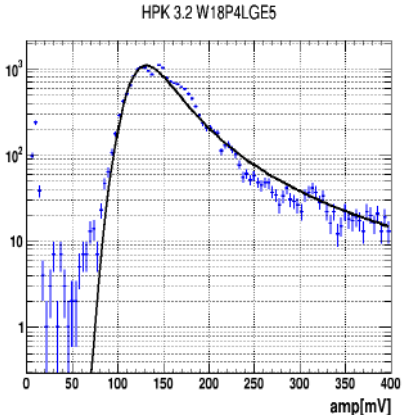

(d) HPK3.2W18P4LGE5 amplitude with fitting function

Figure C.15: Amplitude for batch 604, batch 605 channel 1, channel 2 using irradiated HPK sensors and fitted with (landau, gauss) function.

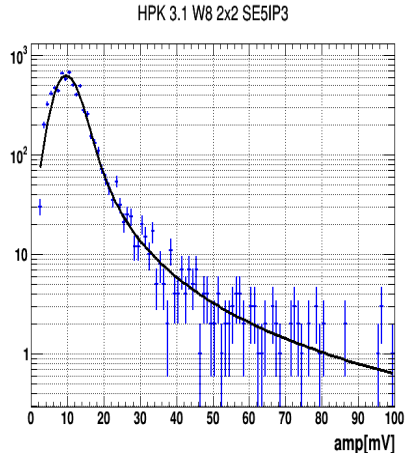

(a) HPK3.1W82×2SE5IP3 amplitude with fitting function

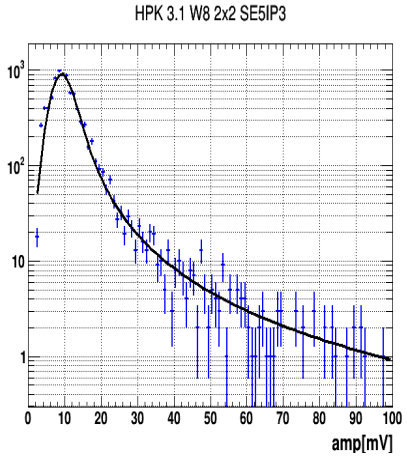

(b) HPK3.1W82×2SE5IP3 amplitude with fitting function

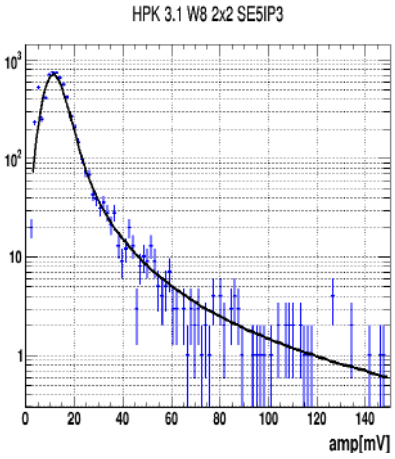

(c) HPK3.1W82×2SE5IP3 amplitude with fitting function

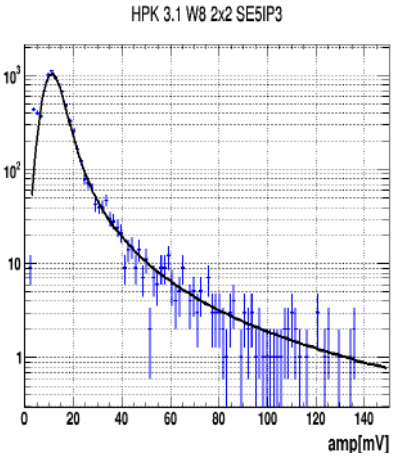

(d) HPK3.1W82×2SE5IP3 amplitude with fitting function

Figure C.16: Amplitude for batch 702, batch 703 channel 1, channel 2 using irradiated HPK sensors and fitted with (landau, gauss) function.

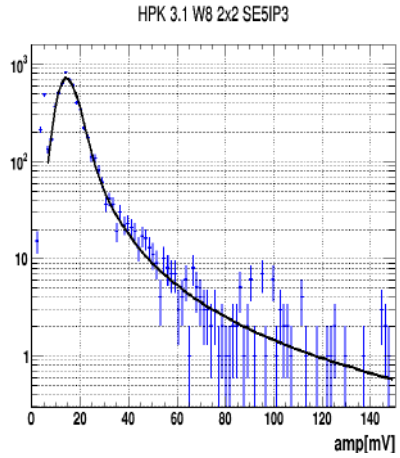

(a) HPK3.1W82×2SE5IP3 amplitude with fitting function

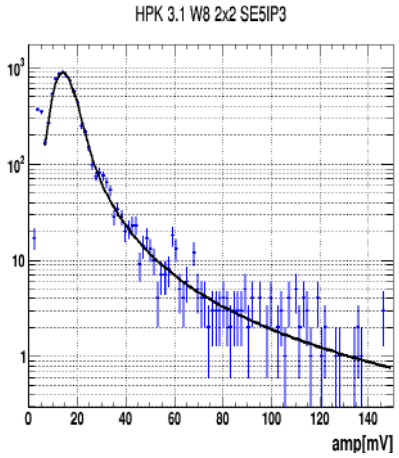

(b) HPK3.1W82×2SE5IP3 amplitude with fitting function

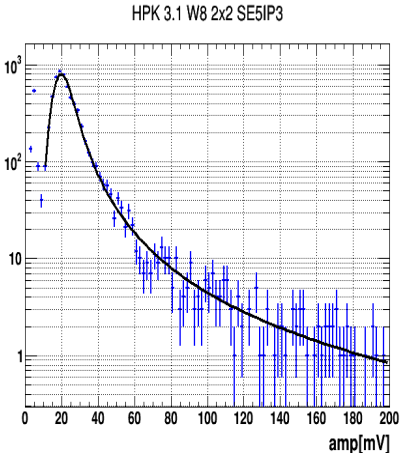

(c) HPK3.1W82×2SE5IP3 amplitude with fitting function

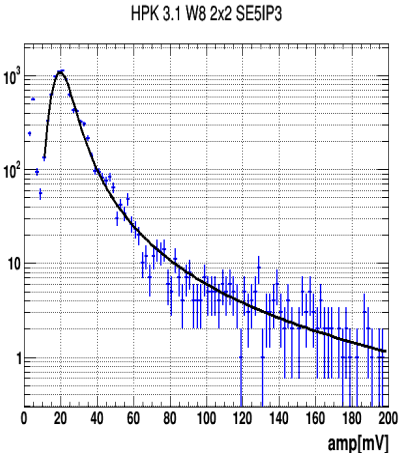

(d) HPK3.1W82×2SE5IP3 amplitude with fitting function

Figure C.17: Amplitude for batch 704, batch 705 channel 1, channel 2 using irradiated HPK sensors and fitted with (landau, gauss) function.

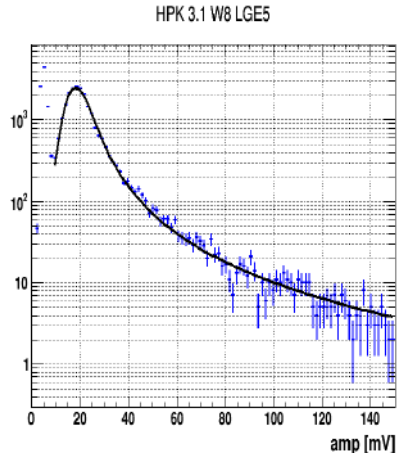

(a) HPK3.1W8LGE5 amplitude with fitting function

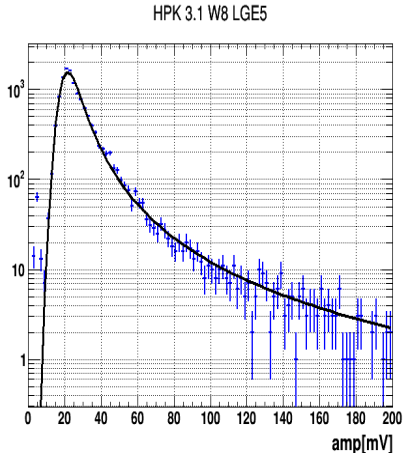

(b) HPK3.1W8LGE5 amplitude with fitting function

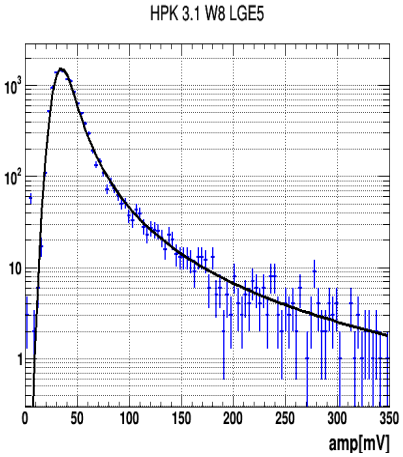

(c) HPK3.1W8LGE5 amplitude with fitting function

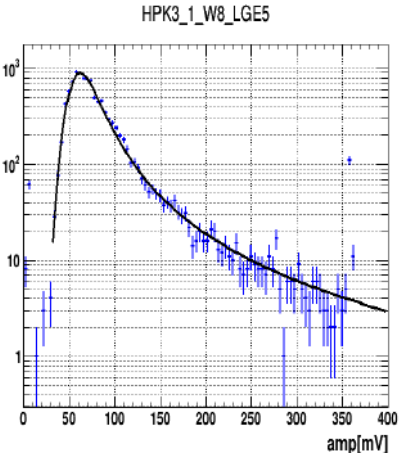

(d) HPK3.1W8LGE5 amplitude with fitting function

Figure C.18: Amplitude for batch 1102 to batch 1105 channel 1 using irradiated HPK sensors and fitted with (landau, gauss) function.

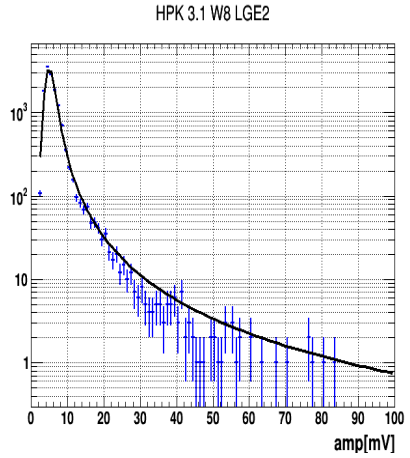

(a) HPK3.1W8LGE2 amplitude with fitting function

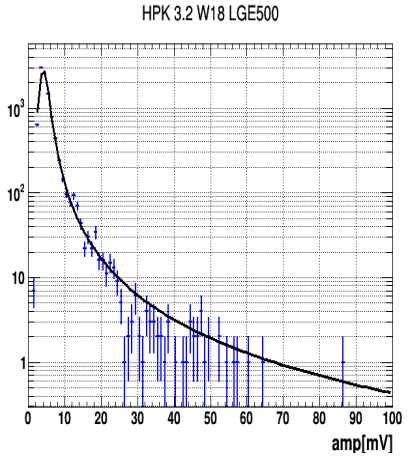

(b) HPK3.2W18LGE500 amplitude with fitting function

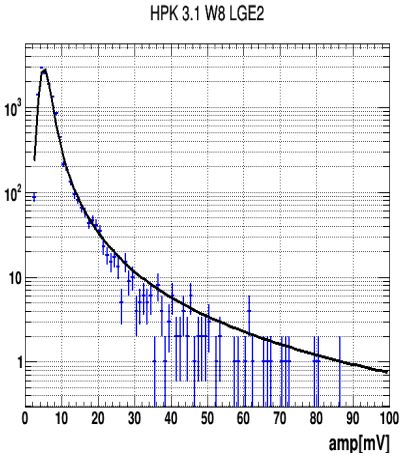

(c) HPK3.1W8LGE2 amplitude with fitting function

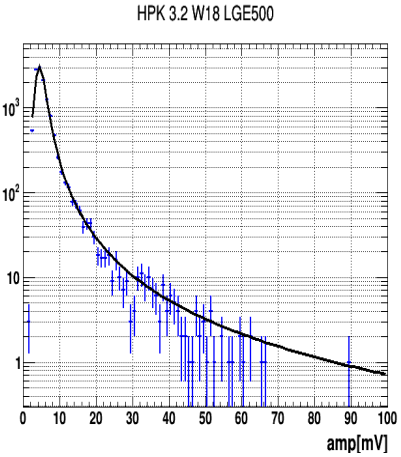

(d) HPK3.2W18LGE500 amplitude with fitting function

Figure C.19: Amplitude for batch 1202, batch 1203 channel 1 and channel 2 using irradiated HPK sensors and fitted with (landau, gauss) function.

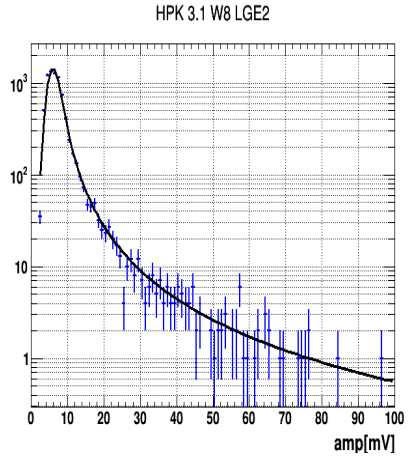

(a) HPK3.1W8LGE2 amplitude with fitting function

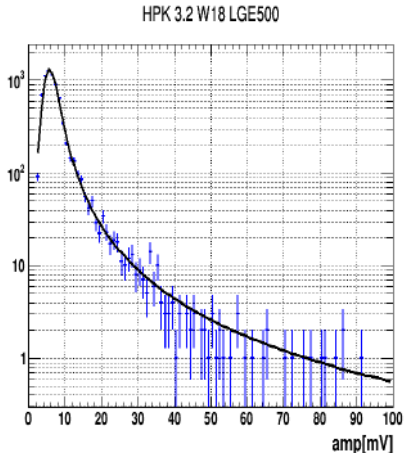

(b) HPK3.2W18LGE500 amplitude with fitting function

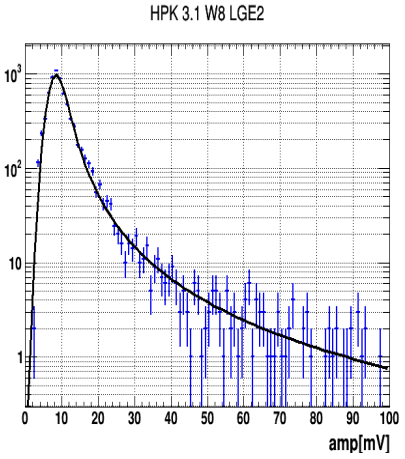

(c) HPK3.1W8LGE2 amplitude with fitting function

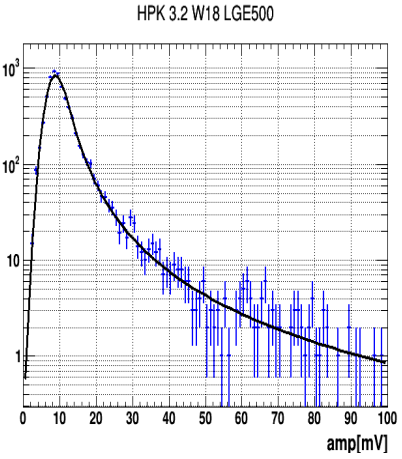

(d) HPK3.2W18LGE500 amplitude with fitting function

Figure C.20: Amplitude for batch 1204, batch 1205 channel 1 and channel 2 using irradiated HPK sensors and fitted with (landau, gauss) function.

Appendix D

HPK Sensors Time Resolution

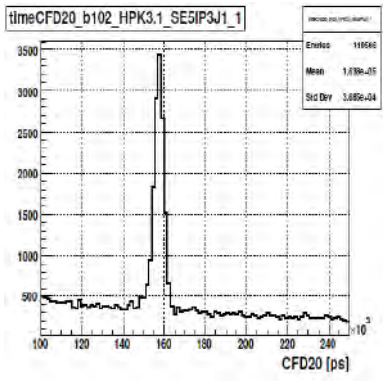

(a) TimeCFD20 distribution for HPK3.1SE5IP3J1

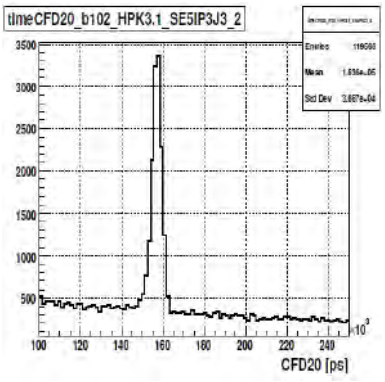

(b) TimeCFD20 distribution for HPK3.1SE5IP3J3

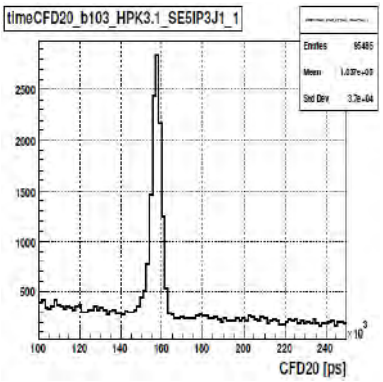

(c) TimeCFD20 distribution for HPK3.1SE5IP3J1

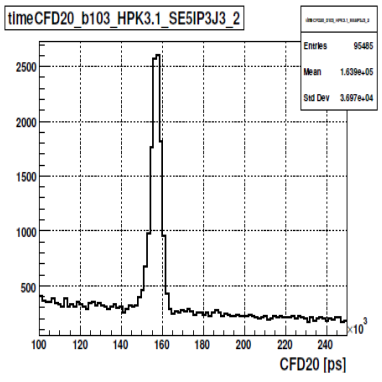

(d) TimeCFD20 distribution for HPK3.1SE5IP3J3

Figure D.1: TimeCFD20 distribution for batch 102 and batch 103, unirradiated HPK sensors utilized at channel 1 and channel 2.

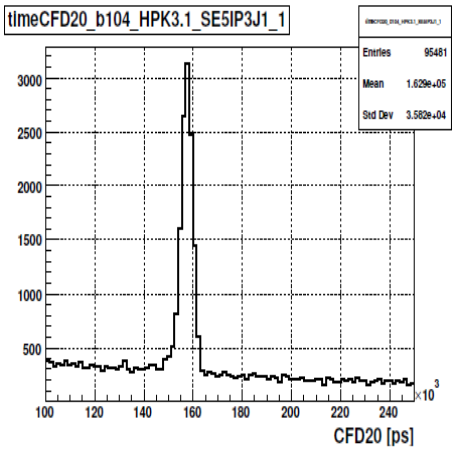

(a) TimeCFD20 distribution for HPK3.1SE5IP3J1

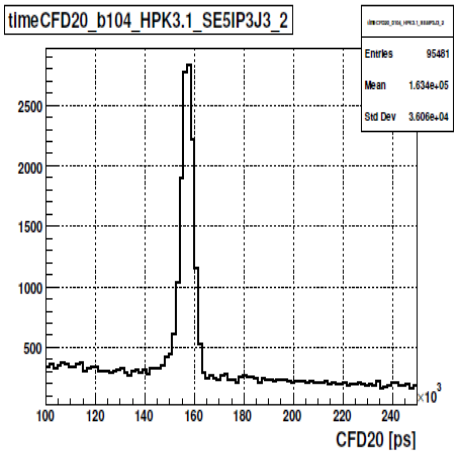

(b) TimeCFD20 distribution for HPK3.1SE5IP3J3

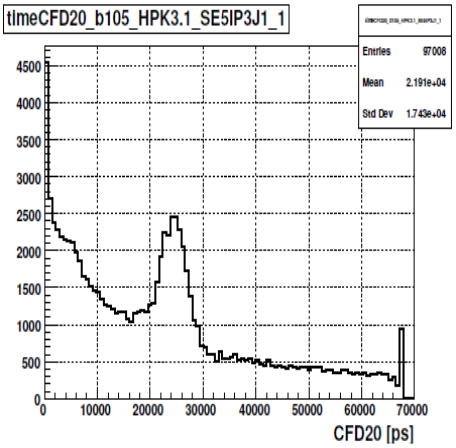

(c) TimeCFD20 distribution for HPK3.1SE5IP3J1

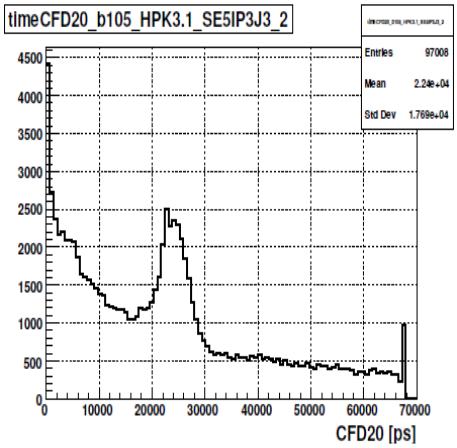

(d) TimeCFD20 distribution for HPK3.1SE5IP3J3

Figure D.2: TimeCFD20 distribution for batch 104 and batch 105, unirradiated HPK sensors utilized at channel 1 and channel 2.

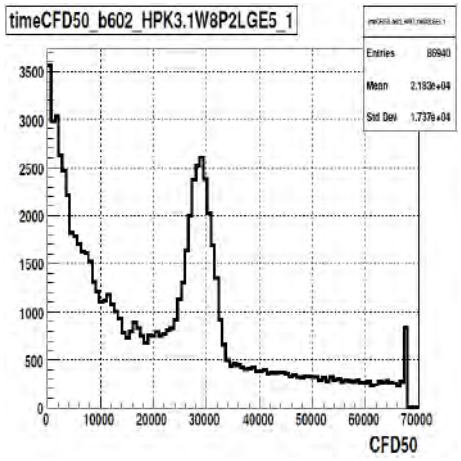

(a) TimeCFD50 distribution for HPK3.1W8P2LGE5

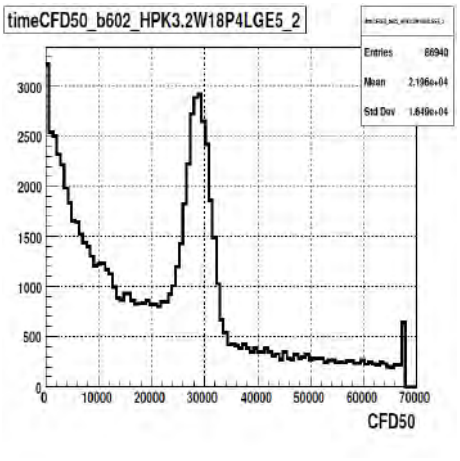

(b) TimeCFD50 distribution for HPK3.2W18P4LGE5

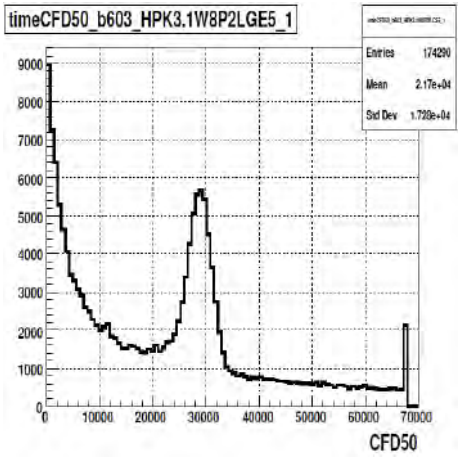

(c) TimeCFD50 distribution for HPK3.1W8P2LGE5

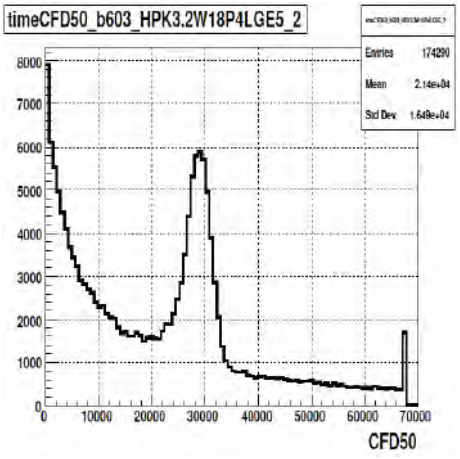

(d) TimeCFD50 distribution for HPK3.2W18P4LGE5

Figure D.3: TimeCFD50 distribution for batch 602 and batch 603, irradiated HPK sensors utilized at channel 1 and channel 2.

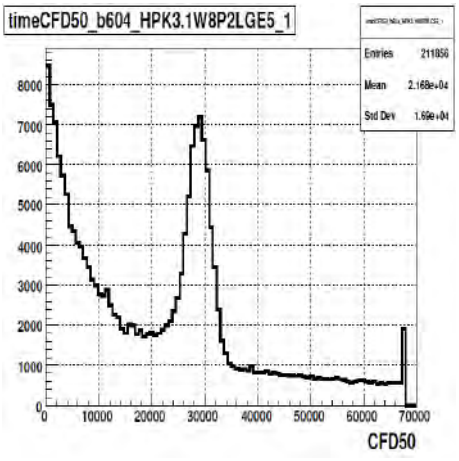

(a) TimeCFD50 distribution for HPK3.1W8P2LGE5

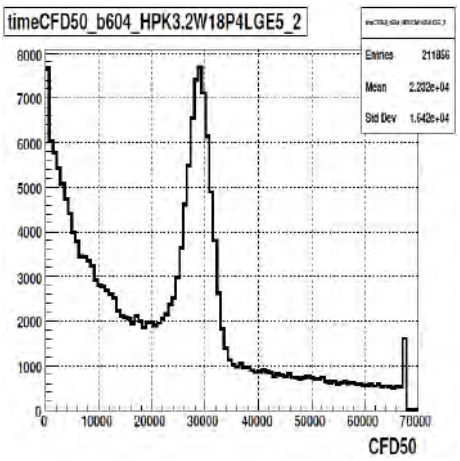

(b) TimeCFD50 distribution for HPK3.2W18P4LGE5

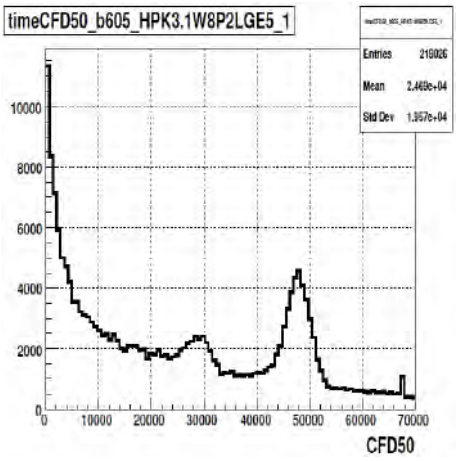

(c) TimeCFD50 distribution for HPK3.1W8P2LGE5

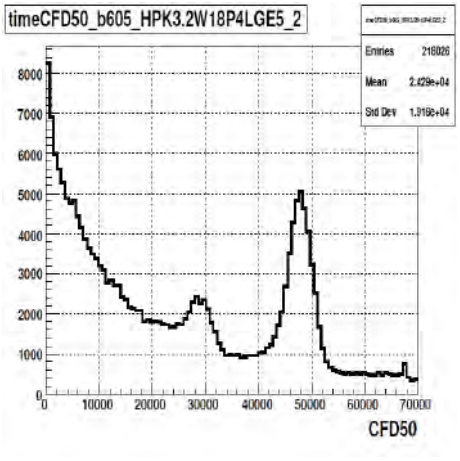

(d) TimeCFD50 distribution for HPK3.2W18P4LGE5

Figure D.4: TimeCFD50 distribution for batch 604 and batch 605, irradiated HPK sensors utilized at channel 1 and channel 2.

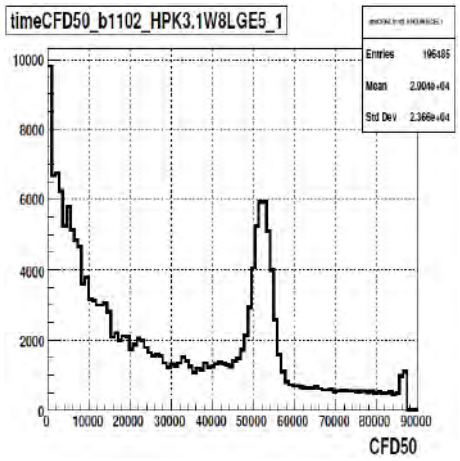

(a) TimeCFD50 distribution for HPK3.1W8LGE5

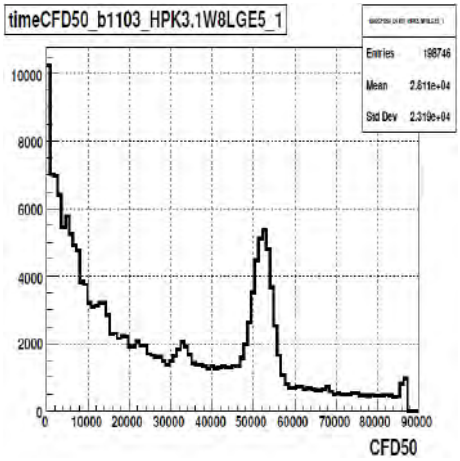

(b) TimeCFD50 distribution for HPK3.1W8LGE5

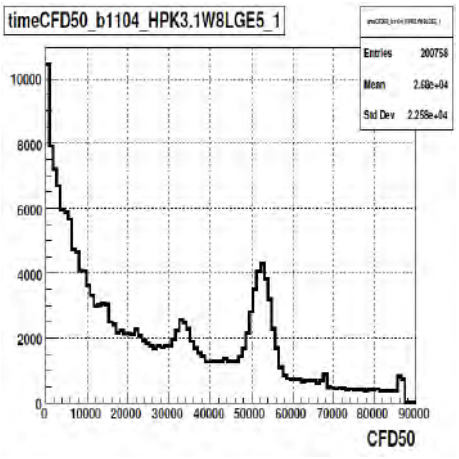

(c) TimeCFD50 distribution for HPK3.1W8LGE5

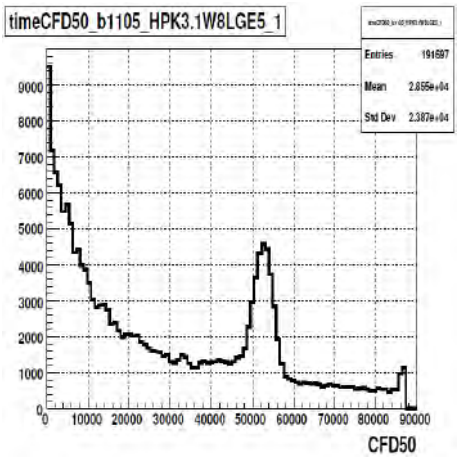

(d) TimeCFD50 distribution for HPK3.1W8LGE5

Figure D.5: TimeCFD50 distribution for batch 1102 to batch 1105, irradiated HPK sensors utilized at channel 1.

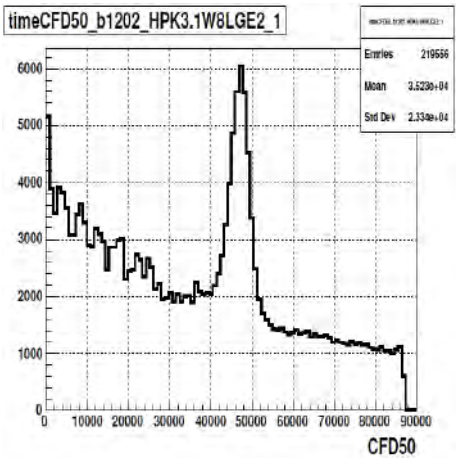

(a) TimeCFD50 distribution for HPK3.1W8LGE2

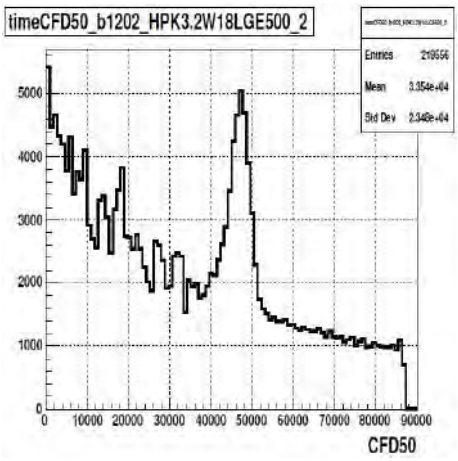

(b) TimeCFD50 distribution for HPK3.2W18LGE500

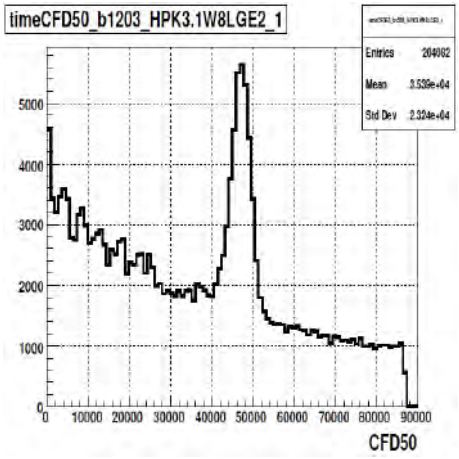

(c) TimeCFD50 distribution for HPK3.1W8LGE2

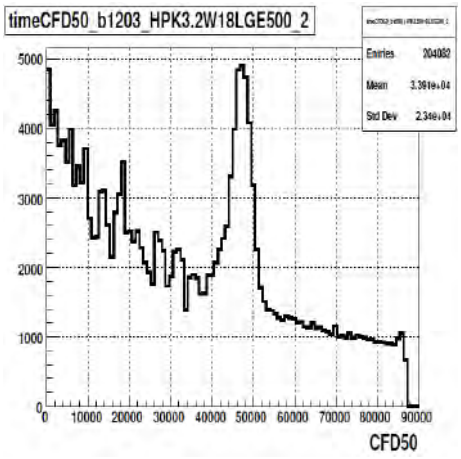

(d) TimeCFD50 distribution for HPK3.2W18LGE500

Figure D.6: TimeCFD50 distribution for batch 1202 and batch 1203, irradiated HPK sensors utilized at channel 1 and channel 2.

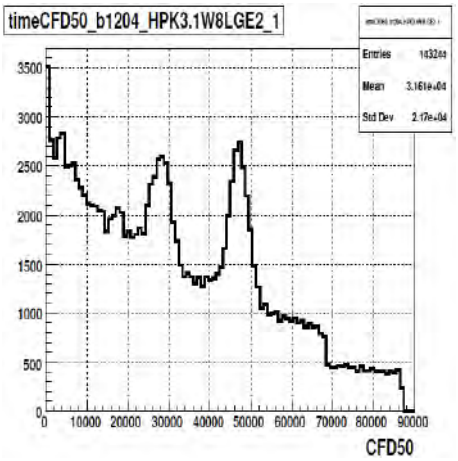

(a) TimeCFD50 distribution for HPK3.1W8LGE2

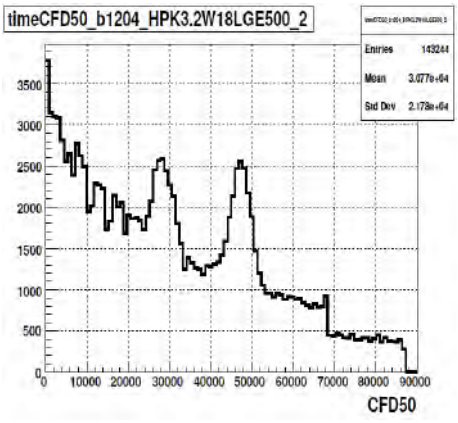

(b) TimeCFD50 distribution for HPK3.2W18LGE500

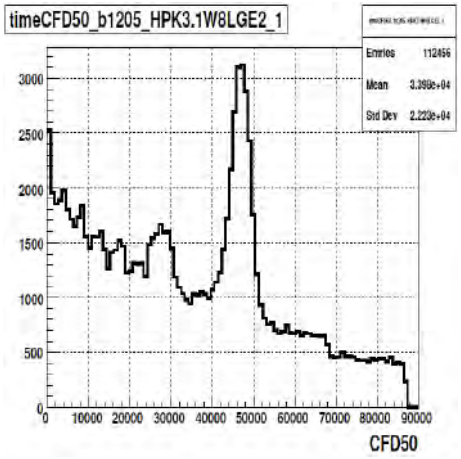

(c) TimeCFD50 distribution for HPK3.1W8LGE2

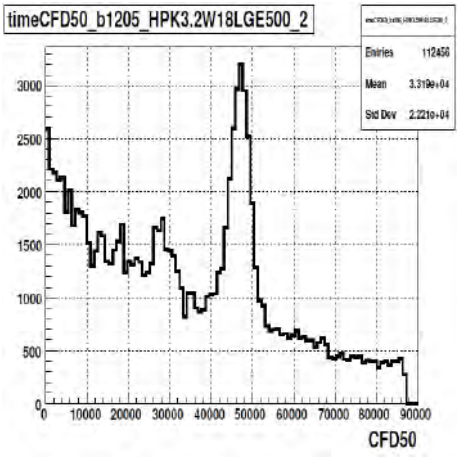

(d) TimeCFD50 distribution for HPK3.2W18LGE500

Figure D.7: TimeCFD50 distribution for batch 1204 and batch 1205, irradiated HPK sensors utilized at channel 1 and channel 2.

Appendix E

TimeCFD vs Amplitude

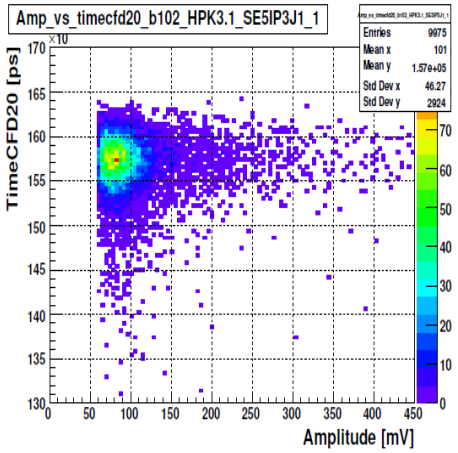

(a) Amplitude vs TimeCFD20 for HPK3.1SE5IP3J1

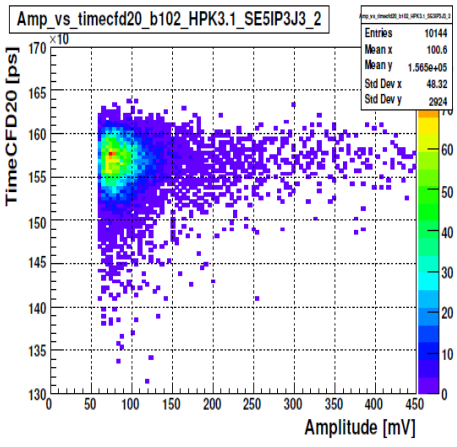

(b) Amplitude vs TimeCFD20 for HPK3.1SE5IP3J3

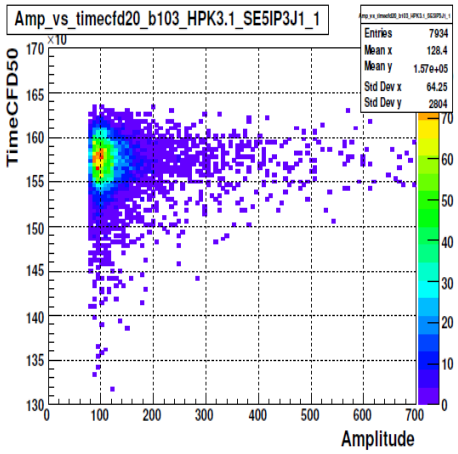

(c) Amplitude vs TimeCFD20 for HPK3.1SE5IP3J1

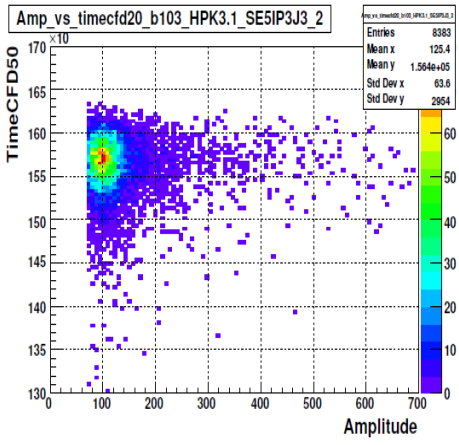

(d) Amplitude vs TimeCFD20 for HPK3.1SE5IP3J3

Figure E.1: TimeCFD20 vs amplitude plots for batch 102 and batch 103, un-irradiated HPK sensors utilized at channel 1 and channel 2.

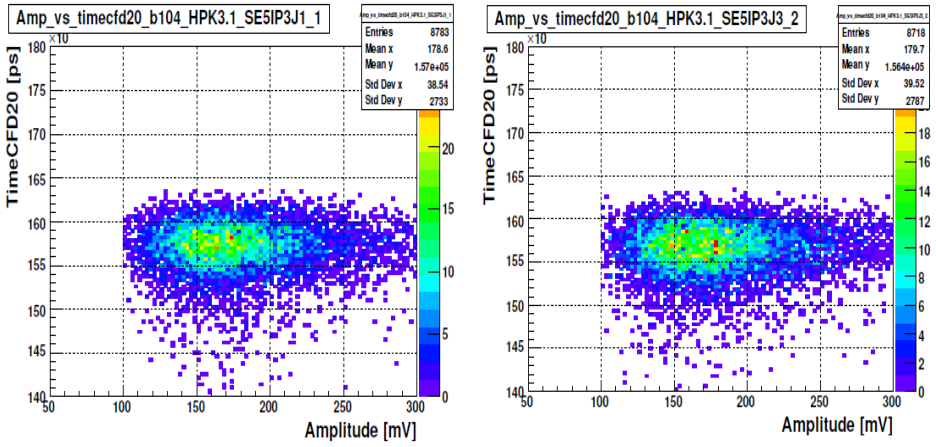

(a) Amplitude vs TimeCFD20 for HPK3.1SE5IP3J1

(b) Amplitude vs TimeCFD20 for HPK3.1SE5IP3J3

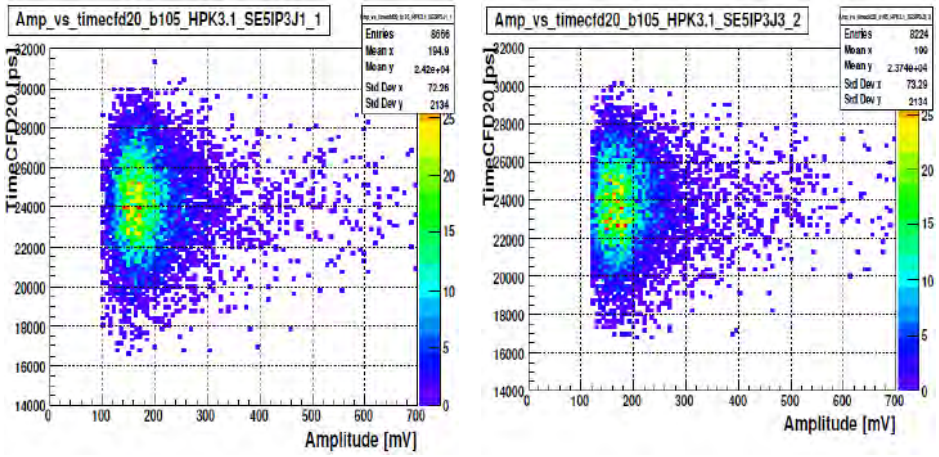

(c) Amplitude vs TimeCFD20 for HPK3.1SE5IP3J1

(d) Amplitude vs TimeCFD20 for HPK3.1SE5IP3J3

Figure E.2: TimeCFD20 vs amplitude plots for batch 104 and batch 105, un-irradiated HPK sensors utilized at channel 1 and channel 2.

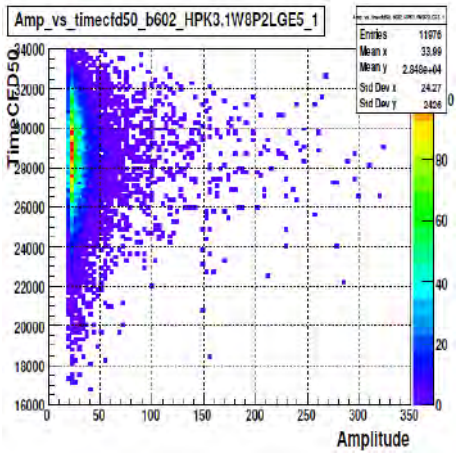

(a) Amplitude vs TimeCFD50 for HPK3.1W8P2LGE5

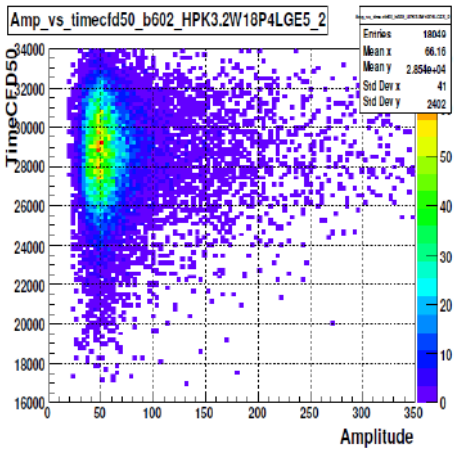

(b) Amplitude vs TimeCFD50 for HPK3.2W18P4LGE5

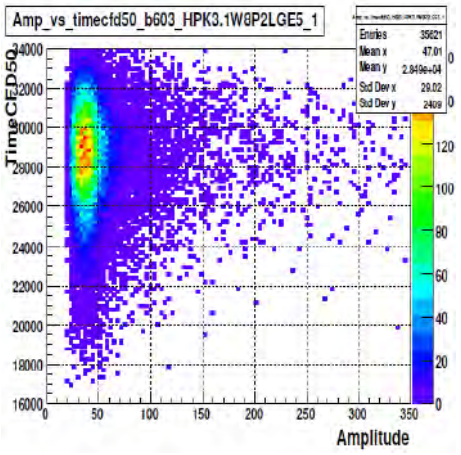

(c) Amplitude vs TimeCFD50 for HPK3.1W8P2LGE5

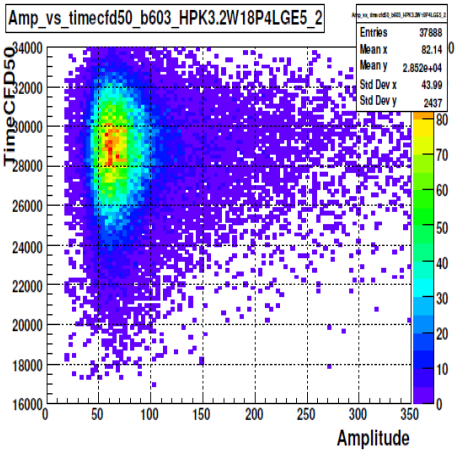

(d) Amplitude vs TimeCFD50 for HPK3.2W18P4LGE5

Figure E.3: TimeCFD50 vs amplitude plots for batch 602 and batch 603, irradiated HPK sensors utilized at channel 1 and channel 2.

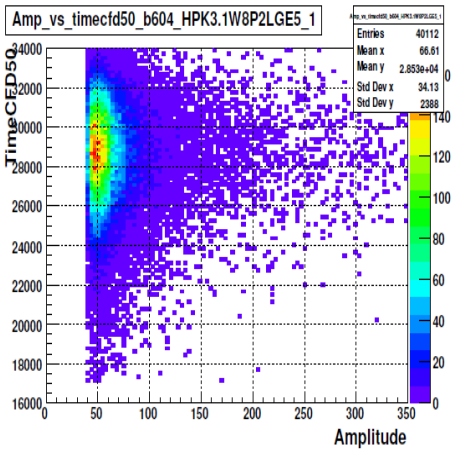

(a) Amplitude vs TimeCFD50 for HPK3.1W8P2LGE5

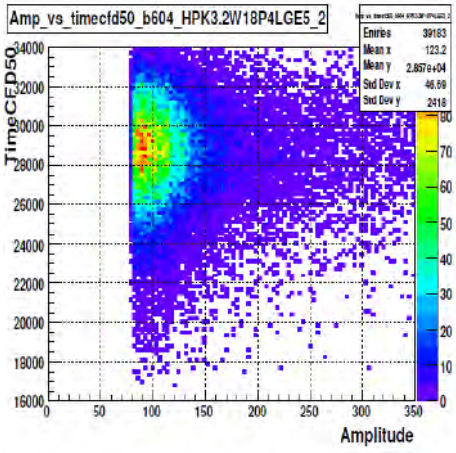

(b) Amplitude vs TimeCFD50 for HPK3.2W18P4LGE5

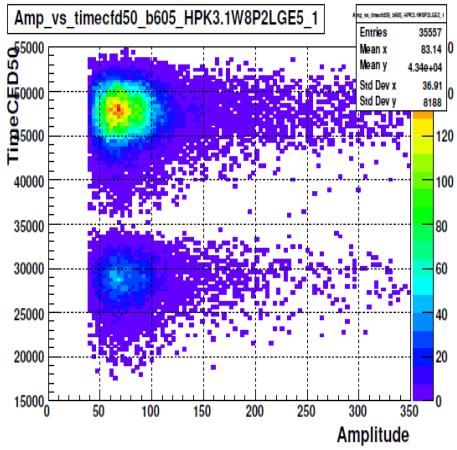

(c) Amplitude vs TimeCFD50 for HPK3.1W8P2LGE5

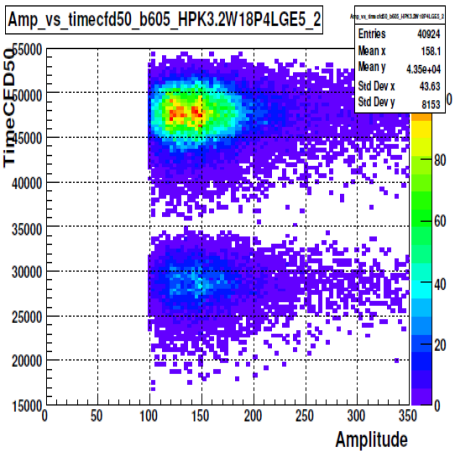

(d) Amplitude vs TimeCFD50 for HPK3.2W18P4LGE5

Figure E.4: TimeCFD50 vs amplitude plots for batch 604 and batch 605, irradiated HPK sensors utilized at channel 1 and channel 2.

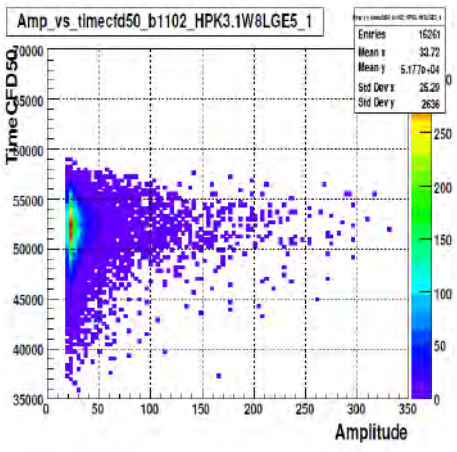

(a) Amplitude vs TimeCFD50 for HPK3.1W8LGE5

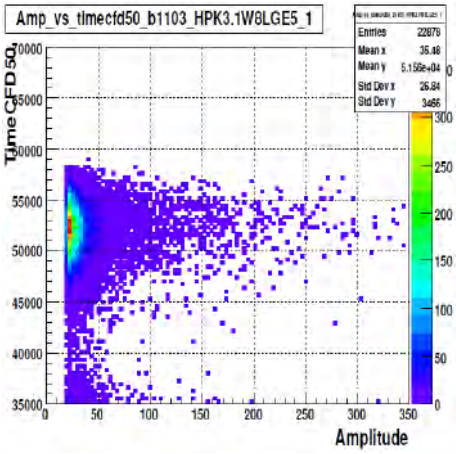

(b) Amplitude vs TimeCFD50 for HPK3.1W8LGE5

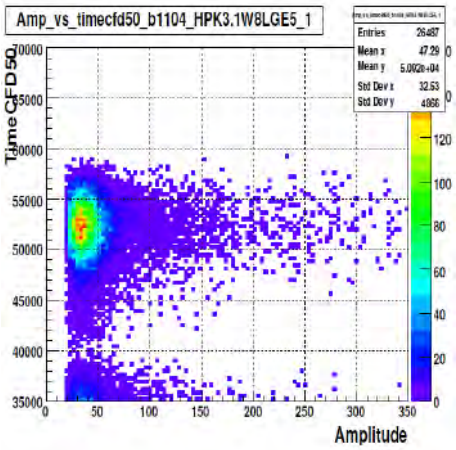

(c) Amplitude vs TimeCFD50 for HPK3.1W8LGE5

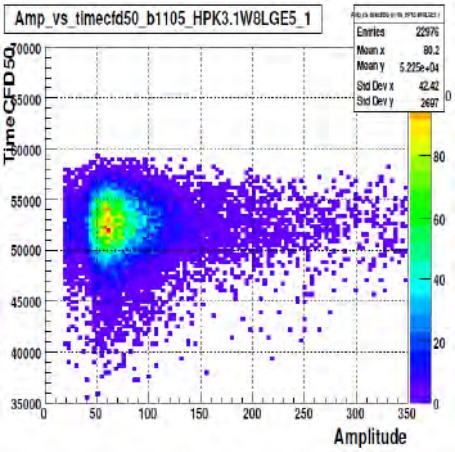

(d) Amplitude vs TimeCFD50 for HPK3.1W8LGE5

Figure E.5: TimeCFD50 vs amplitude plots for batch 1102 to batch 1105, irradiated HPK sensors utilized at channel 1.

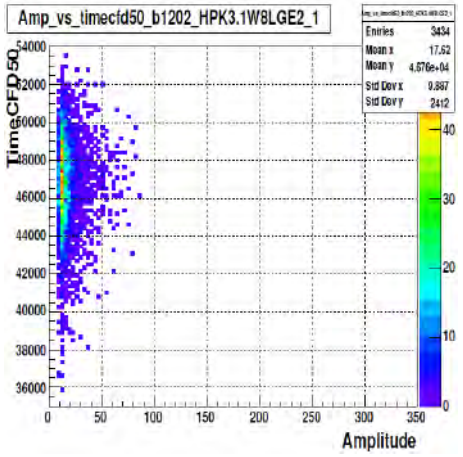

(a) Amplitude vs TimeCFD50 for HPK3.1W8LGE2

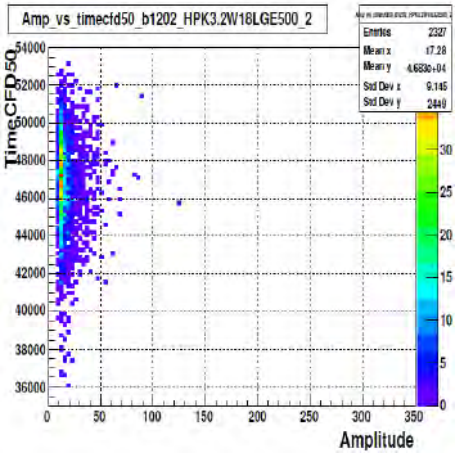

(b) Amplitude vs TimeCFD50 for HPK3.2W18LGE500

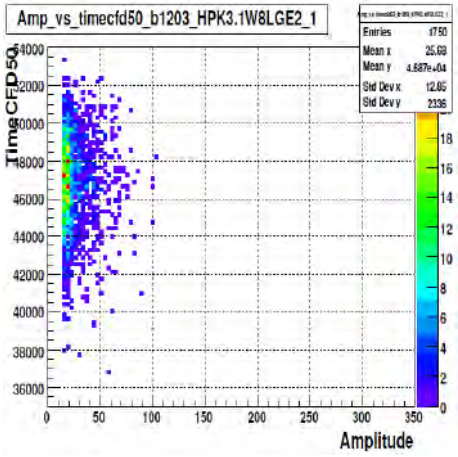

(c) Amplitude vs TimeCFD50 for HPK3.1W8LGE2

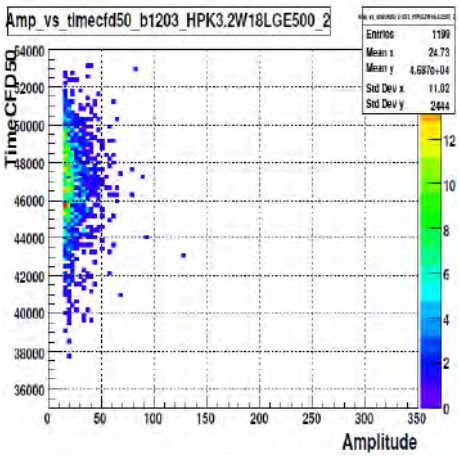

(d) Amplitude vs TimeCFD50 for HPK3.2W18LGE500

Figure E.6: TimeCFD50 vs amplitude plots for batch 1202 and batch 1203, irradiated HPK sensors utilized at channel 1 and channel 2.

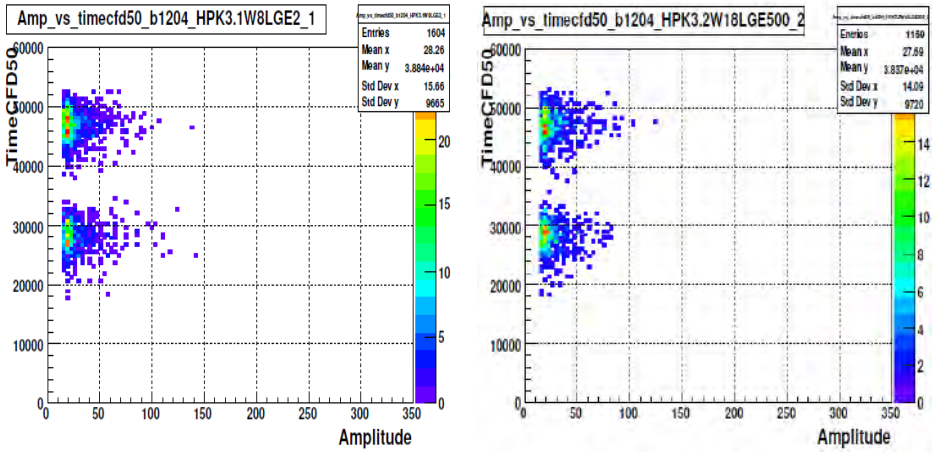

(a) Amplitude vs TimeCFD50 for HPK3.1W8LGE2

(b) Amplitude vs TimeCFD50 for HPK3.2W18LGE500

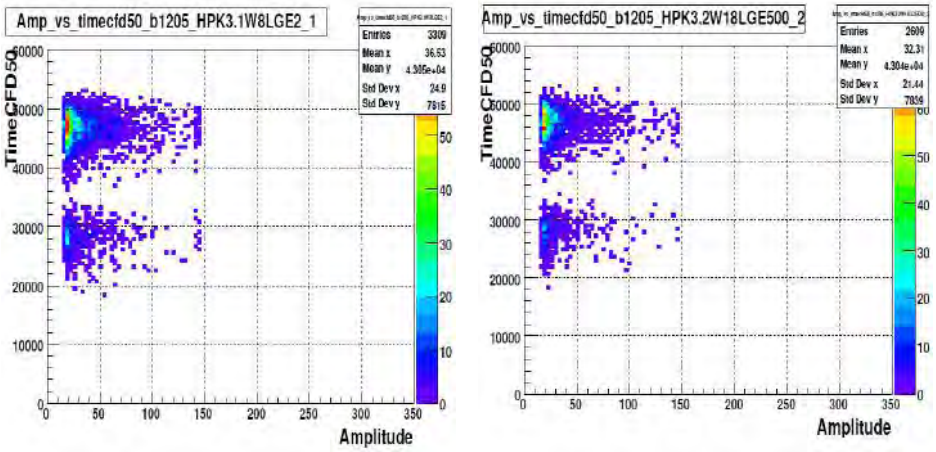

(c) Amplitude vs TimeCFD50 for HPK3.1W8LGE2

(d) Amplitude vs TimeCFD50 for HPK3.2W18LGE500

Figure E.7: TimeCFD50 vs amplitude plots for batch 1204 and batch 1205, irradiated HPK sensors utilized at channel 1 and channel 2.

Appendix F

Background Removing

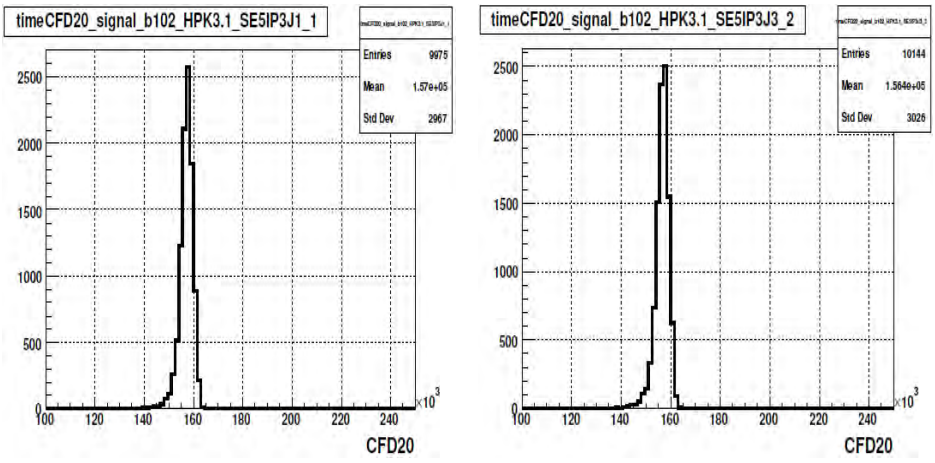

(a) HPK3.1SE5IP3J1 TimeCFD20 signal (b) HPK3.1SE5IP3J3 TimeCFD20 signal

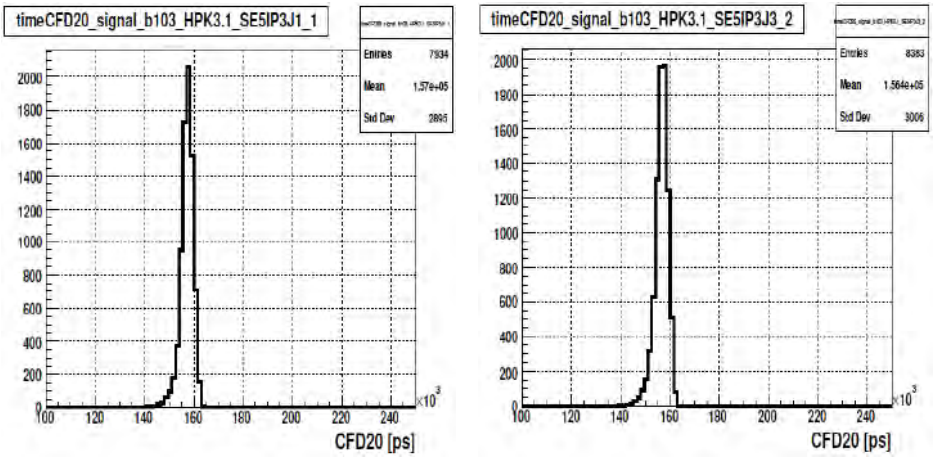

(c) HPK3.1SE5IP3J1 TimeCFD20 signal (d) HPK3.1SE5IP3J3 TimeCFD20 signal

Figure F.1: Signal contribution after removing background by applying cuts for batch 102 and batch 103, channel 1 and channel 2.

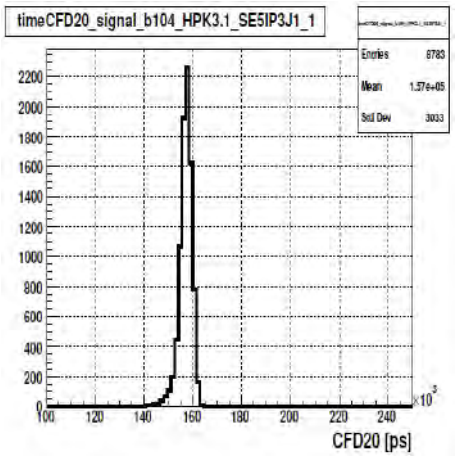

(a) HPK3.1SE5IP3J1 TimeCFD20 signal

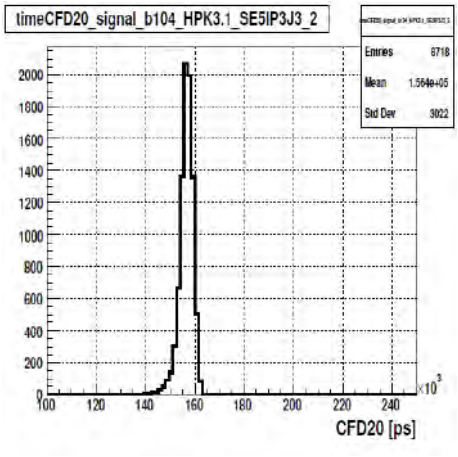

(b) HPK3.1SE5IP3J3 TimeCFD20 signal

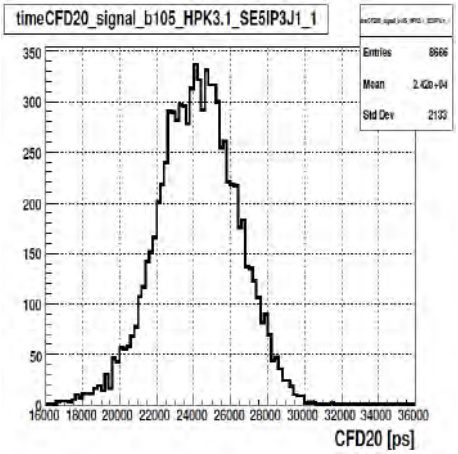

(c) HPK3.1SE5IP3J1 TimeCFD20 signal

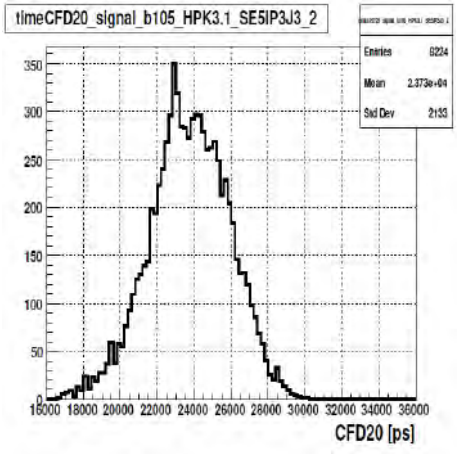

(d) HPK3.1SE5IP3J3 TimeCFD20 signal

Figure F.2: Signal contribution after removing background by applying cuts for batch 104 and batch 105, channel 1 and channel 2.

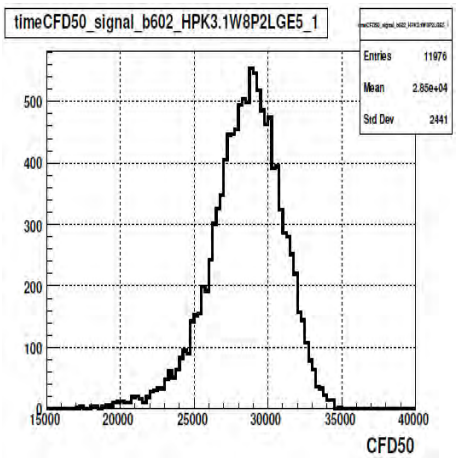

(a) HPK3.1W8P2LGE5 TimeCFD50 signal

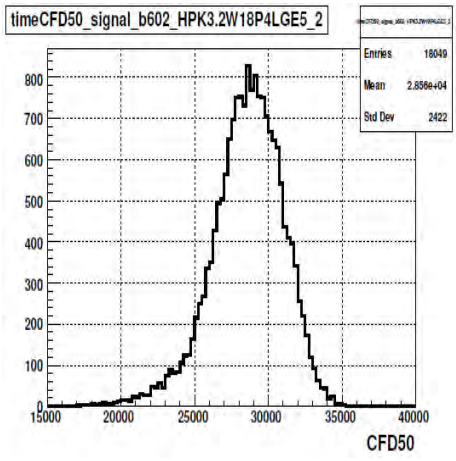

(b) HPK3.2W18P4LGE5 TimeCFD50 signal

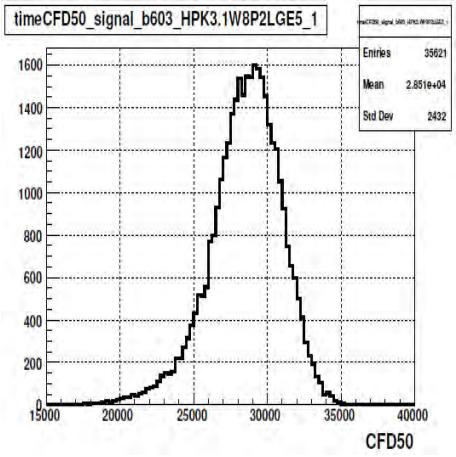

(c) HPK3.1W8P2LGE5 TimeCFD50 signal

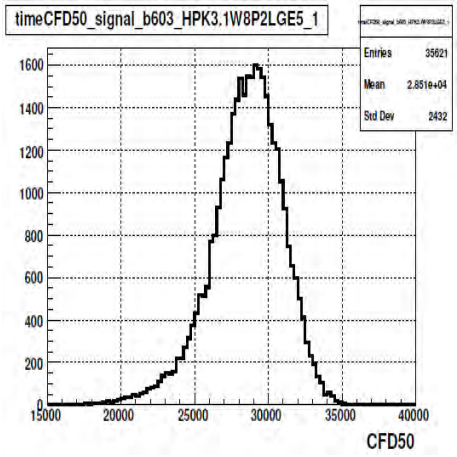

(d) HPK3.2W18P4LGE5 TimeCFD50 signal

Figure F.3: Signal contribution after removing background by applying cuts for batch 602 and batch 603, channel 1 and channel 2.

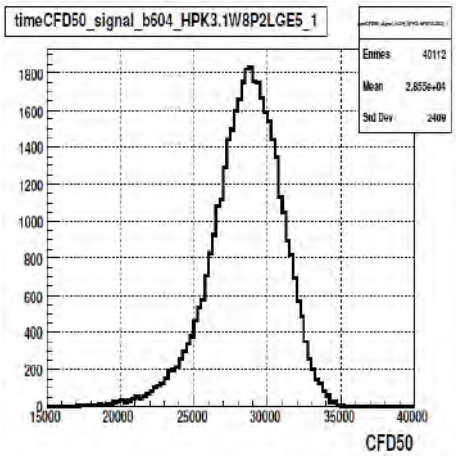

(a) HPK3.1W8P2LGE5 TimeCFD50 signal

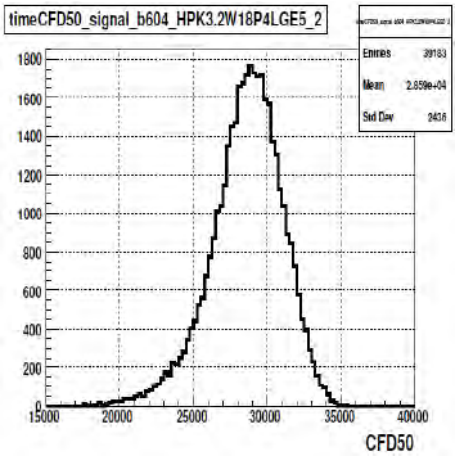

(b) HPK3.2W18P4LGE5 TimeCFD50 signal

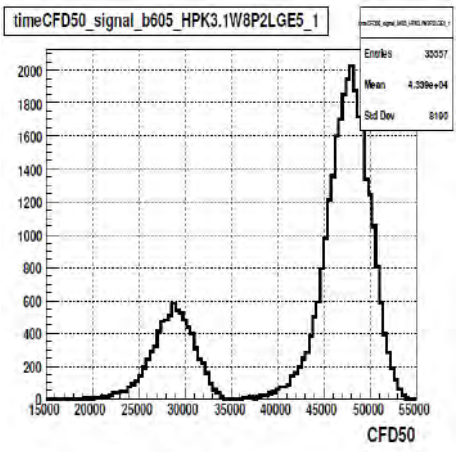

(c) HPK3.1W8P2LGE5 TimeCFD50 signal

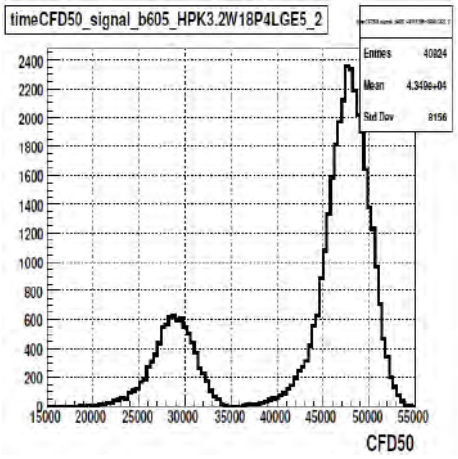

(d) HPK3.2W18P4LGE5 TimeCFD50 signal

Figure F.4: Signal contribution after removing background by applying cuts for batch 604 and batch 605, channel 1 and channel 2.

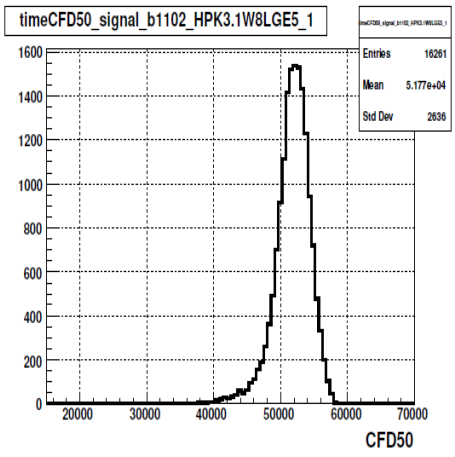

(a) HPK3.1W8LGE5 TimeCFD50 signal

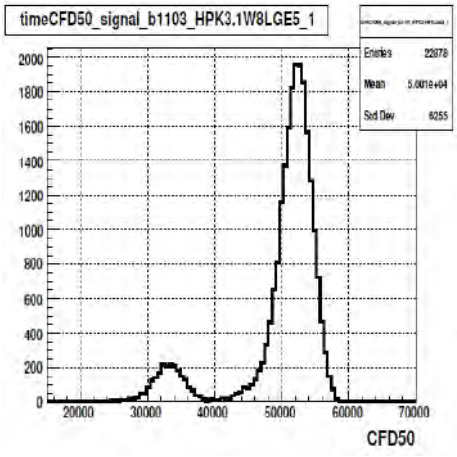

(b) HPK3.1W8LGE5 TimeCFD50 signal

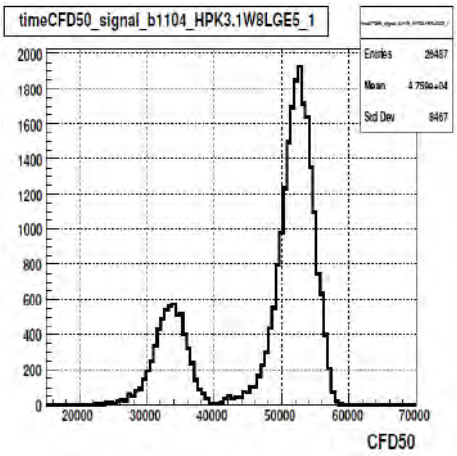

(c) HPK3.1W8LGE5 TimeCFD50 signal

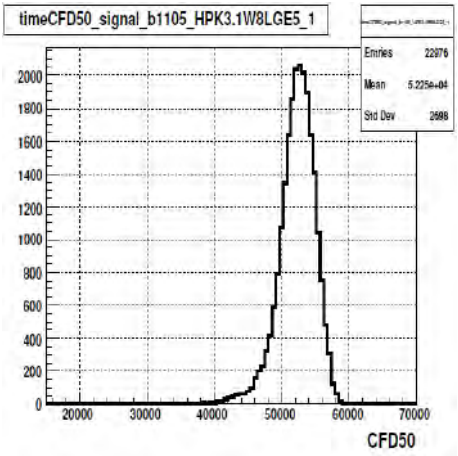

(d) HPK3.1W8LGE5 TimeCFD50 signal

Figure F.5: Signal contribution after removing background by applying cuts for batch 1102 to batch 1105 at channel 1.

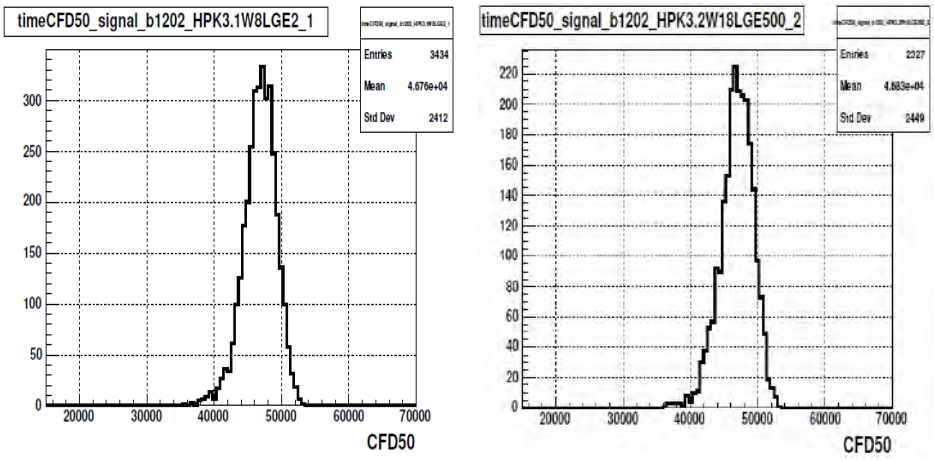

(a) HPK3.1W8LGE2 TimeCFD50 signal (b) HPK3.2W18LGE500 TimeCFD50 signal

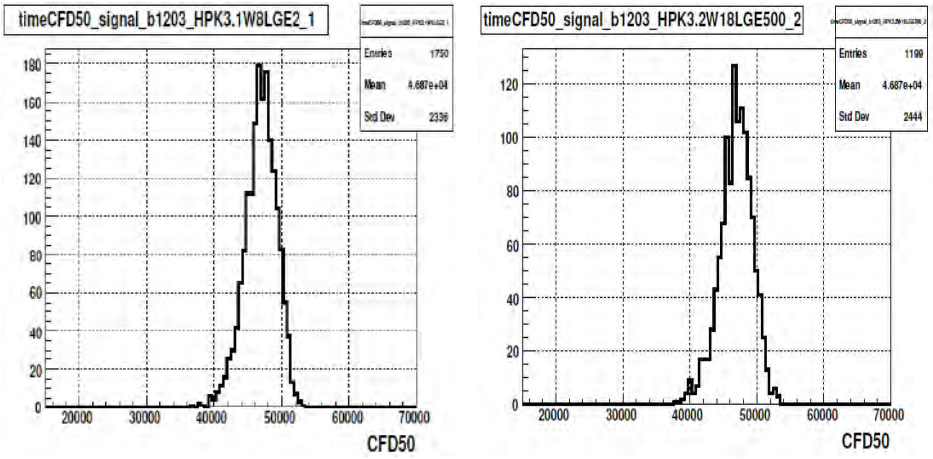

(c) HPK3.1W8LGE2 TimeCFD50 signal (d) HPK3.2W18LGE500 TimeCFD50 signal

Figure F.6: Signal contribution after removing background by applying cuts for batch 1202 to batch 1203 at channel 1 and channel 2.

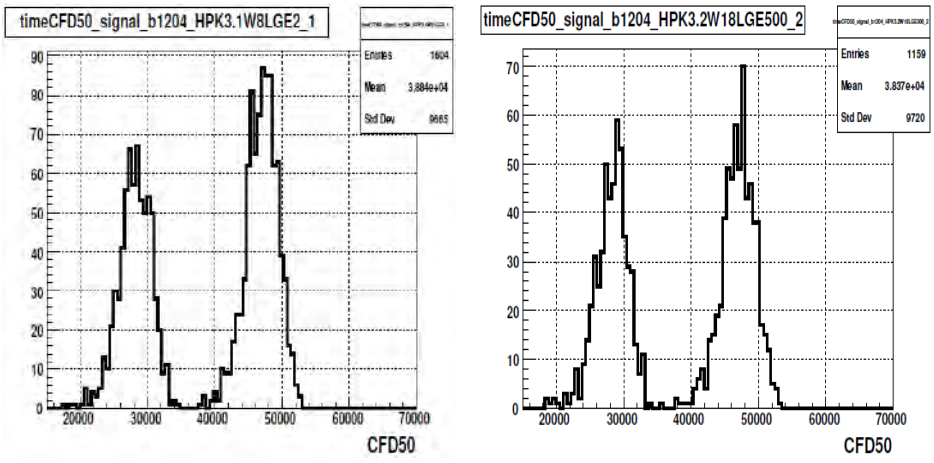

(a) HPK3.1W8LGE2 TimeCFD50 signal (b) HPK3.2W18LGE500 TimeCFD50 signal

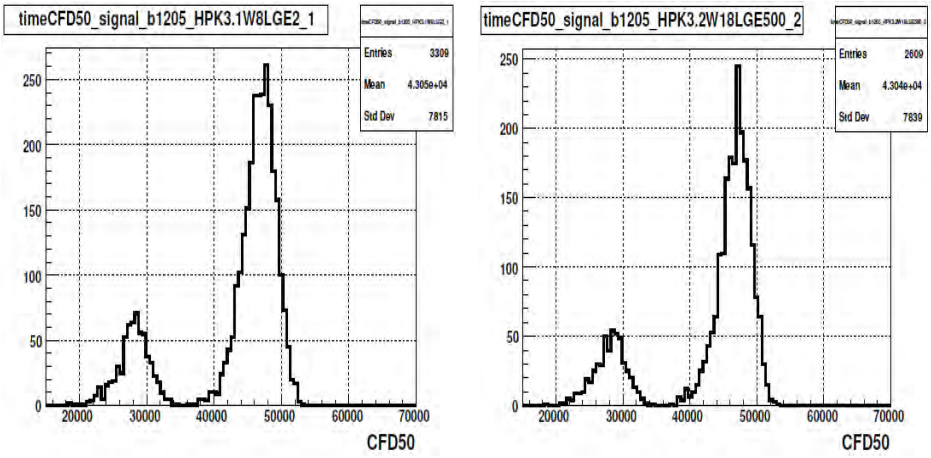

(c) HPK3.1W8LGE2 TimeCFD50 signal (d) HPK3.2W18LGE500 TimeCFD50 signal

Figure F.7: Signal contribution after removing background by applying cuts for batch 1204 to batch 1205 at channel 1 and channel 2

Appendix G

Time Resolution Fitting with Gaussian Function

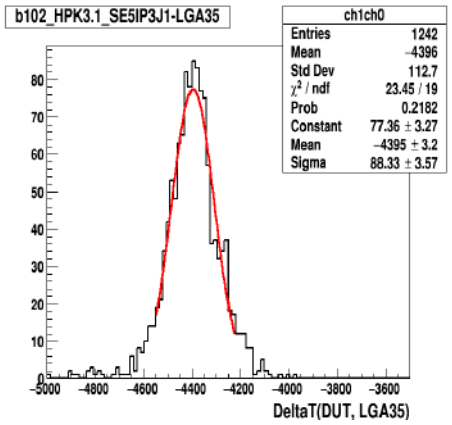

(a) Time difference of device DUT and LGA35

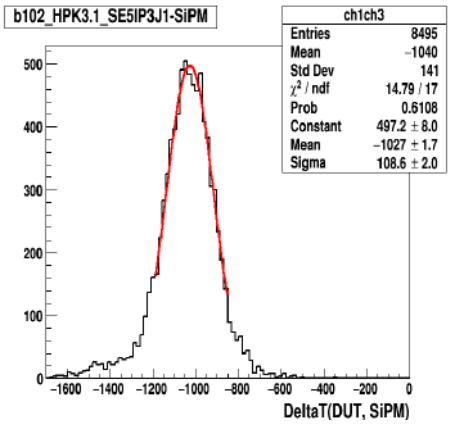

(b) Time difference of device DUT and SiPM

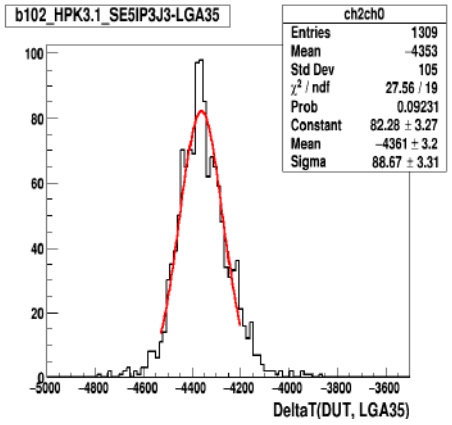

(c) Time difference of device DUT and LGA35

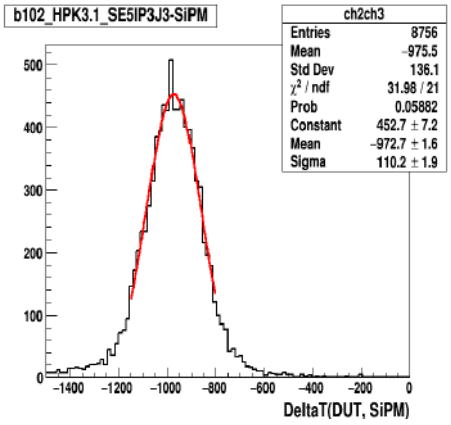

(d) Time difference of device DUT and SiPM

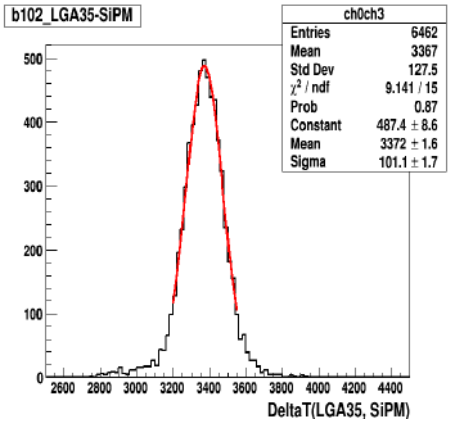

(e) Time difference of device DUT and SiPM

Figure G.1: Time difference of the devices fitted with gaussian function for batch 102, at different channels.

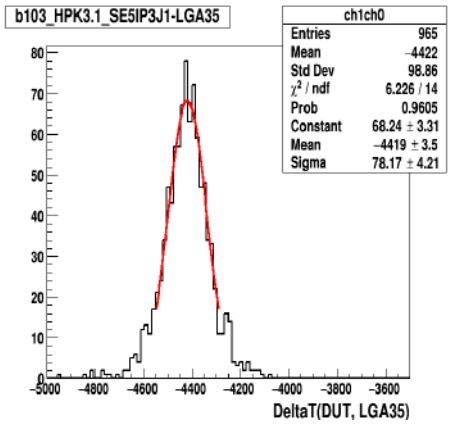

(a) Time difference of device DUT and LGA35

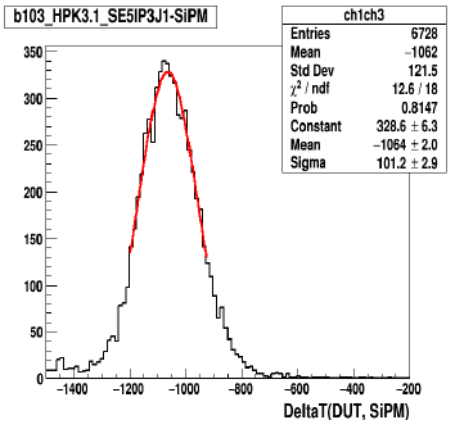

(b) Time difference of device DUT and SiPM

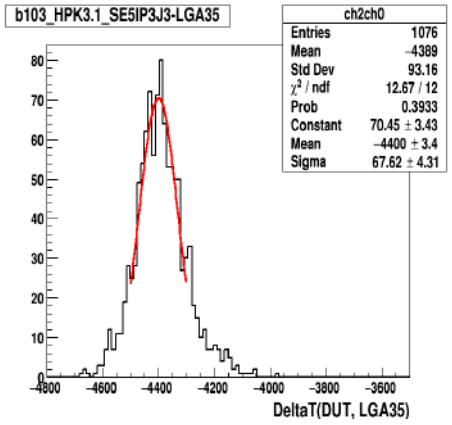

(c) Time difference of device DUT and LGA35

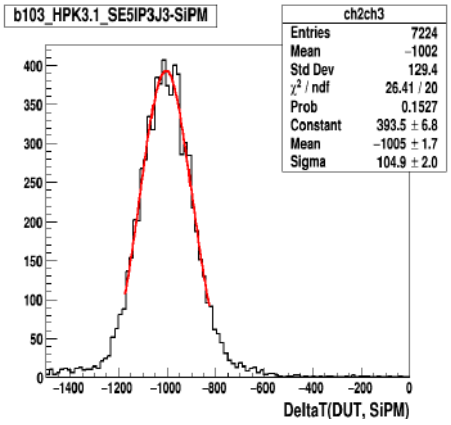

(d) Time difference of device DUT and SiPM

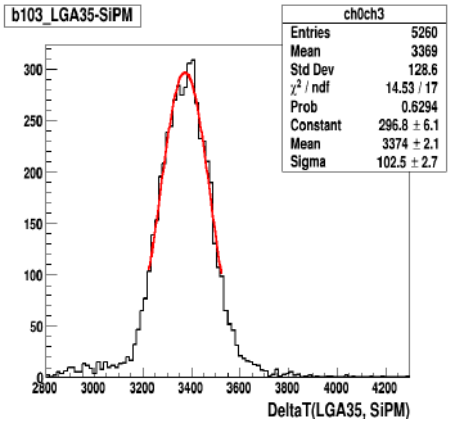

(e) Time difference of device LGA35 and SiPM

Figure G.2: Time difference of the devices fitted with gaussian function for batch 103, at different channels.

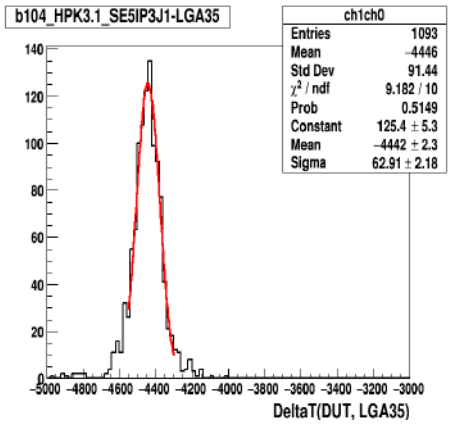

(a) Time difference of device DUT and LGA35

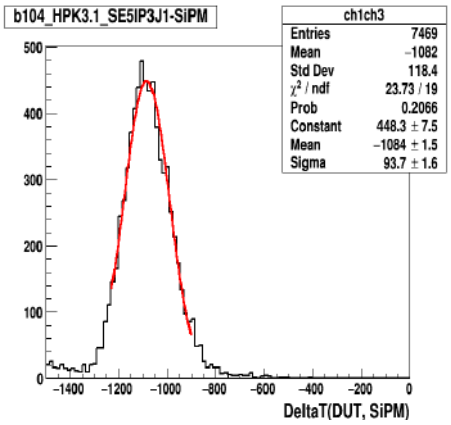

(b) Time difference of device DUT and SiPM

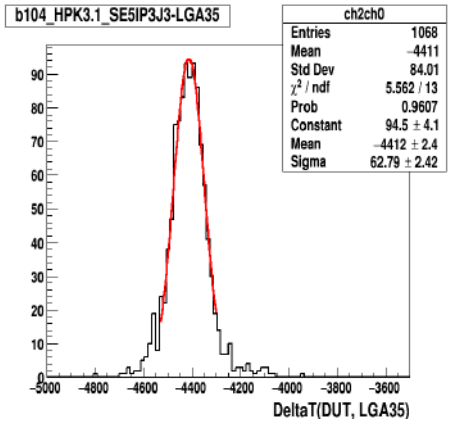

(c) Time difference of device DUT and LGA35

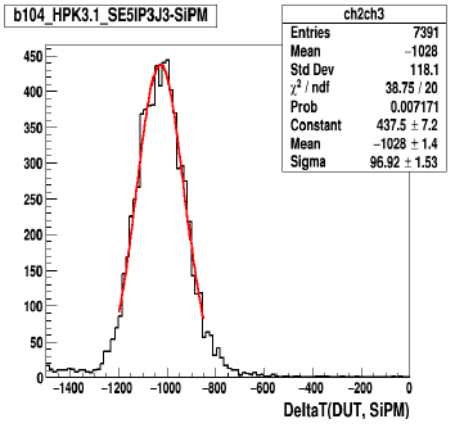

(d) Time difference of device DUT and SiPM

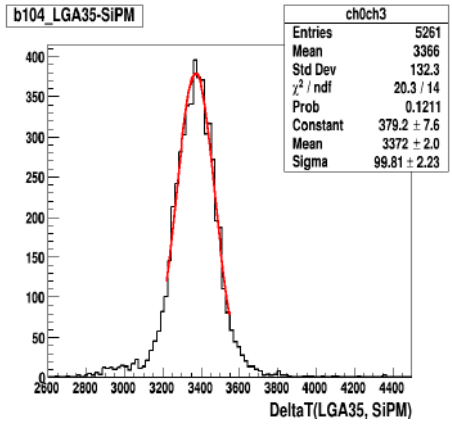

(e) Time difference of device LGA35 and SiPM

Figure G.3: Time difference of the devices fitted with gaussian function for batch 104, at different channels.

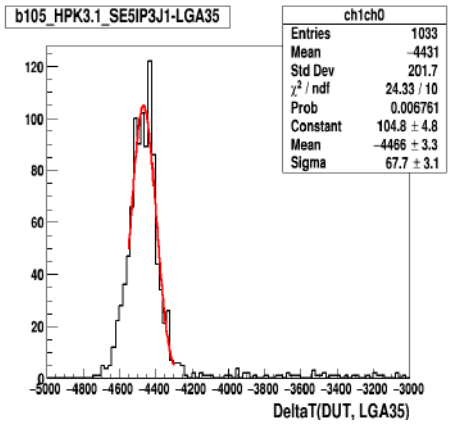

(a) Time difference of device DUT and LGA35

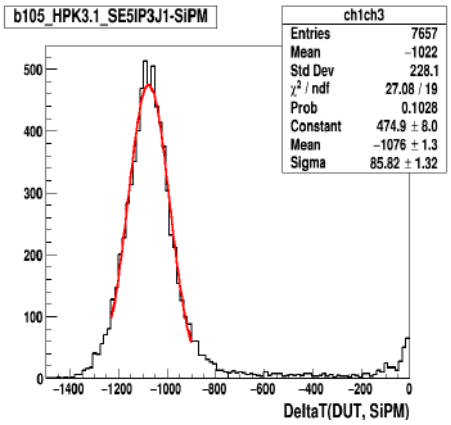

(b) Time difference of device DUT and SiPM

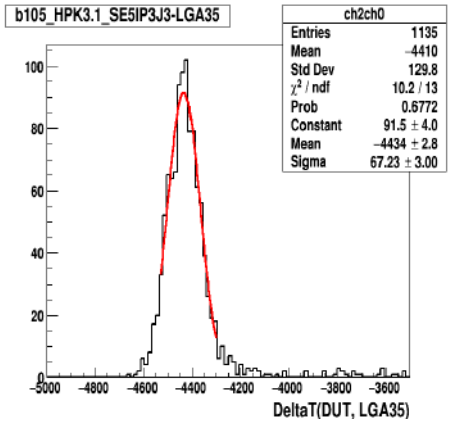

(c) Time difference of device DUT and LGA35

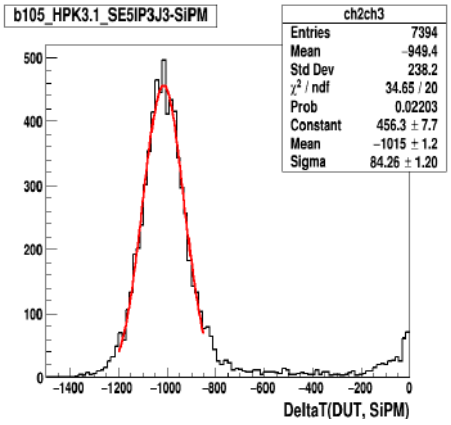

(d) Time difference of device DUT and SiPM

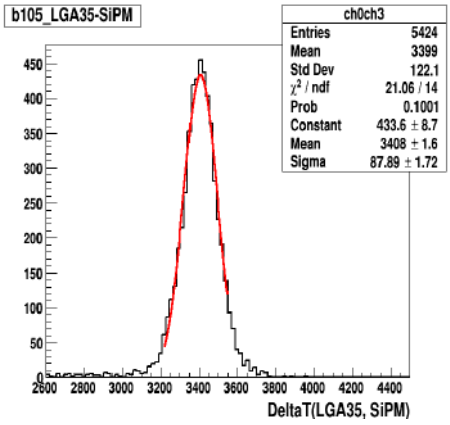

(e) Time difference of device LGA35 and SiPM

Figure G.4: Time difference of the devices fitted with gaussian function for batch 105, at different channels.

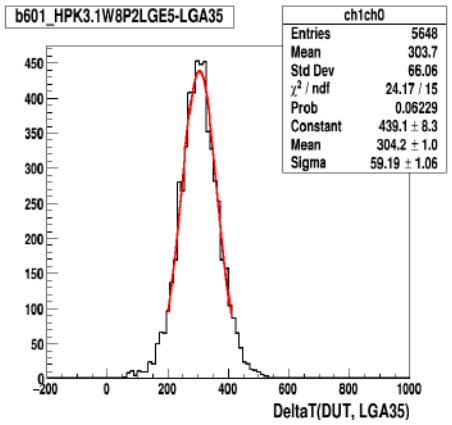

(a) Time difference of device DUT and LGA35

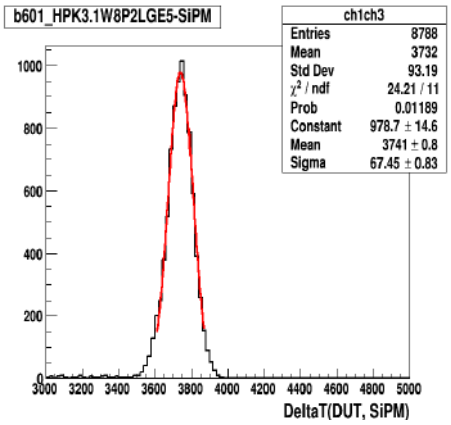

(b) Time difference of device DUT and SiPM

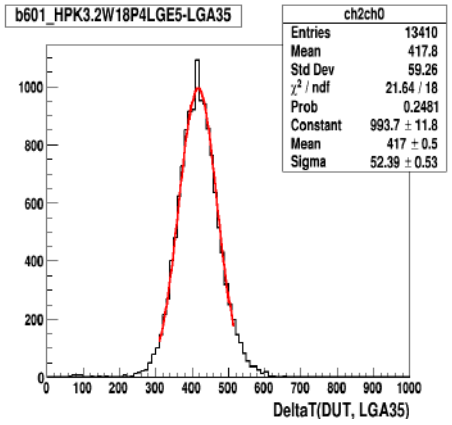

(c) Time difference of device DUT and LGA35

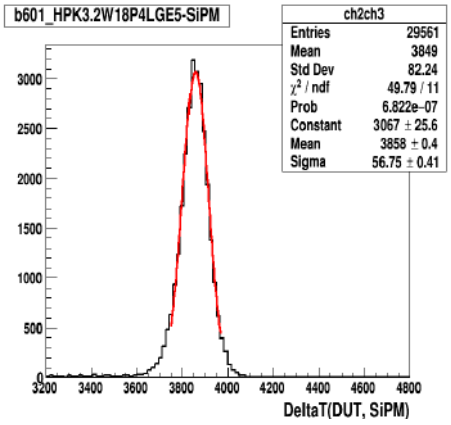

(d) Time difference of device DUT and SiPM

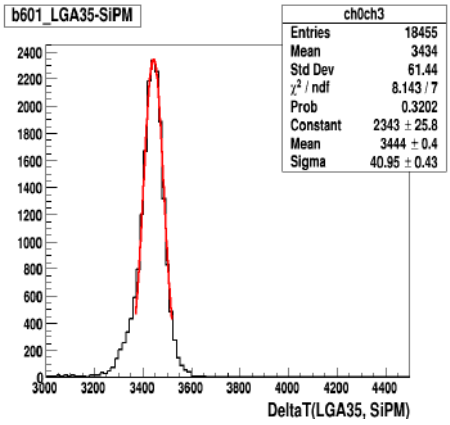

(e) Time difference of device LGA35 and SiPM

Figure G.5: Time difference of the devices fitted with gaussian function for batch 601, at different channels.

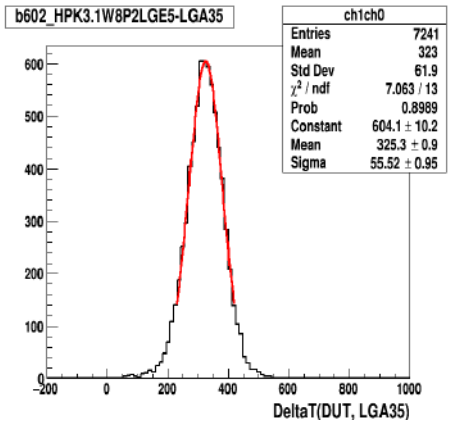

(a) Time difference of device DUT and LGA35

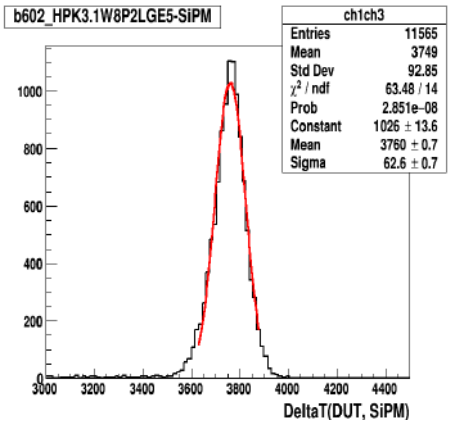

(b) Time difference of device DUT and SiPM

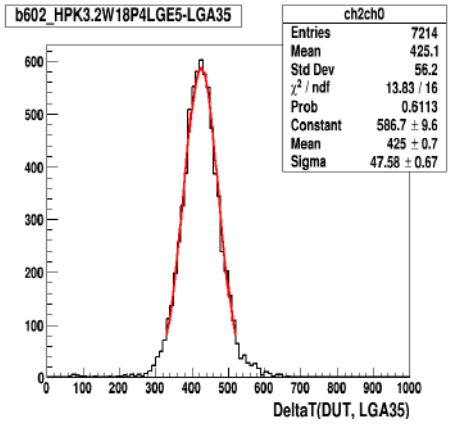

(c) Time difference of device DUT and LGA35

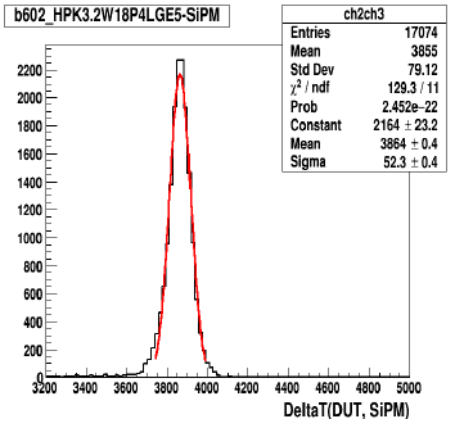

(d) Time difference of device DUT and SiPM

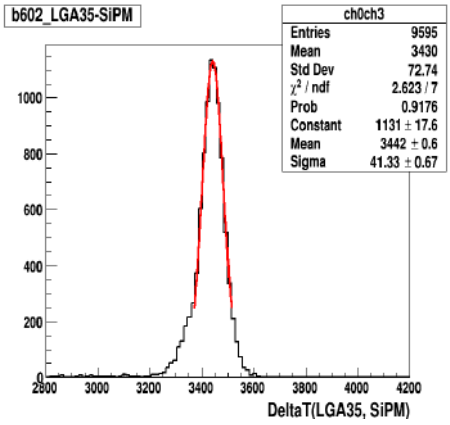

(e) Time difference of device LGA35 and SiPM

Figure G.6: Time difference of the devices fitted with gaussian function for batch 602, at different channels.

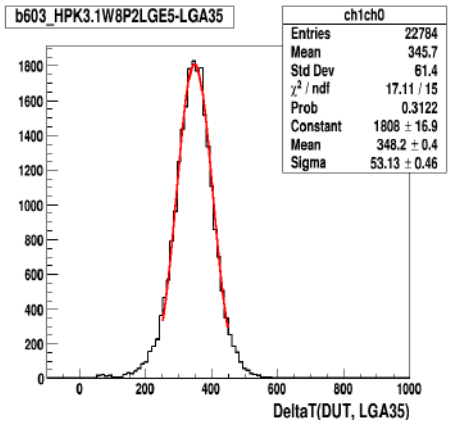

(a) Time difference of device DUT and LGA35

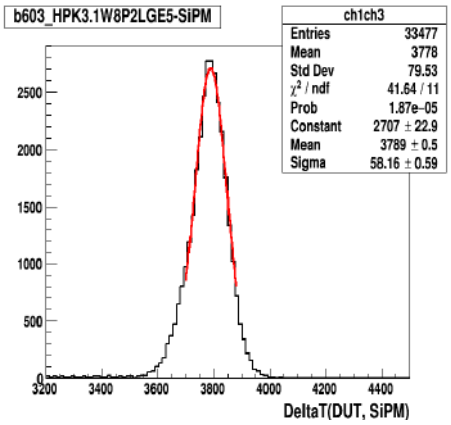

(b) Time difference of device DUT and SiPM

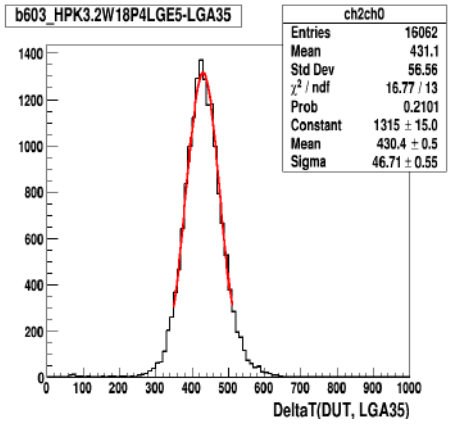

(c) Time difference of device DUT and LGA35

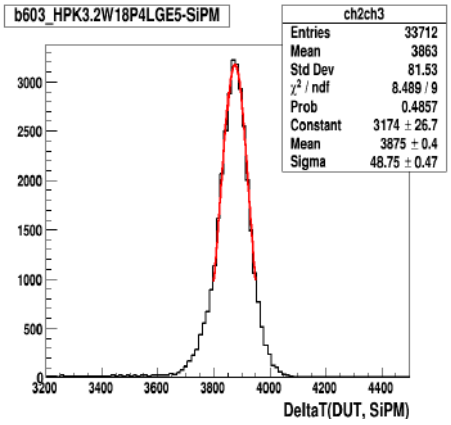

(d) Time difference of device DUT and SiPM

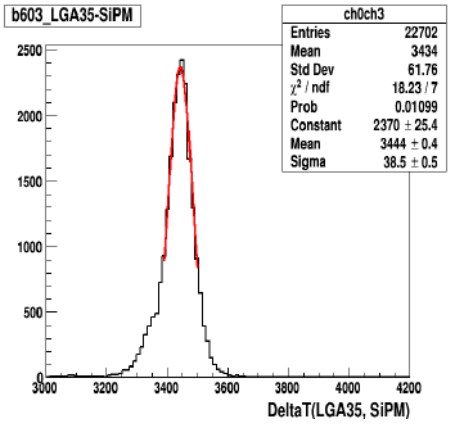

(e) Time difference of device LGA35 and SiPM

Figure G.7: Time difference of the devices fitted with gaussian function for batch 603, at different channels.

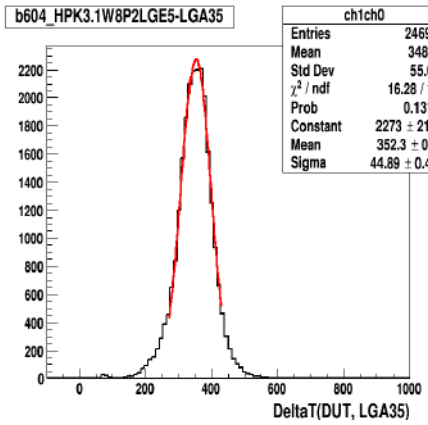

(a) Time difference of device DUT and LGA35

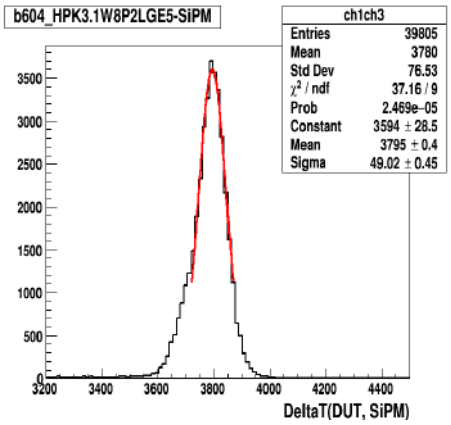

(b) Time difference of device DUT and SiPM

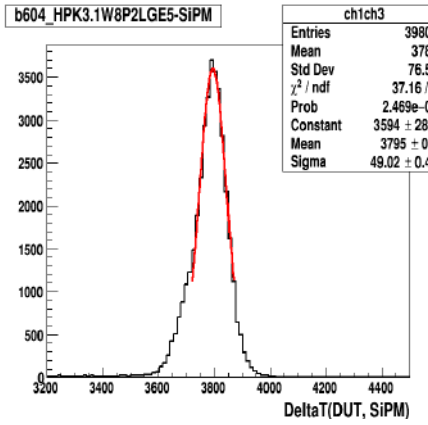

(c) Time difference of device DUT and SiPM

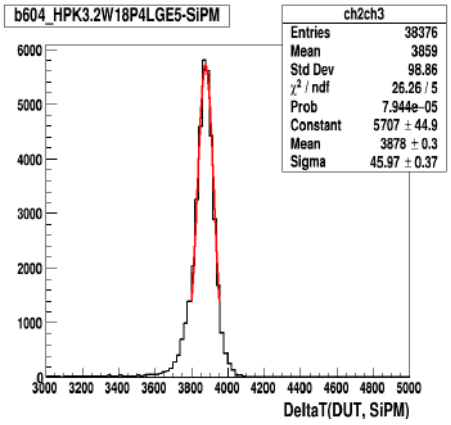

(d) Time difference of device DUT and SiPM

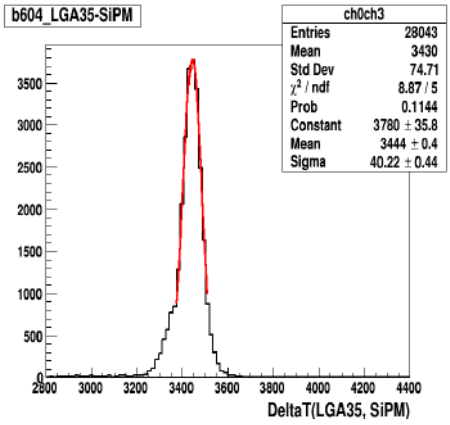

(e) Time difference of device LGA35 and SiPM

Figure G.8: Time difference of the devices fitted with gaussian function for batch 604, at different channels.

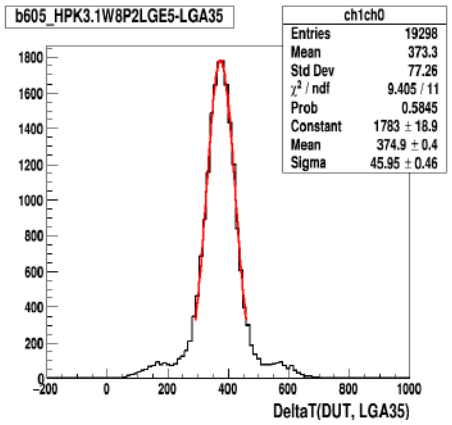

(a) Time difference of device DUT and LGA35

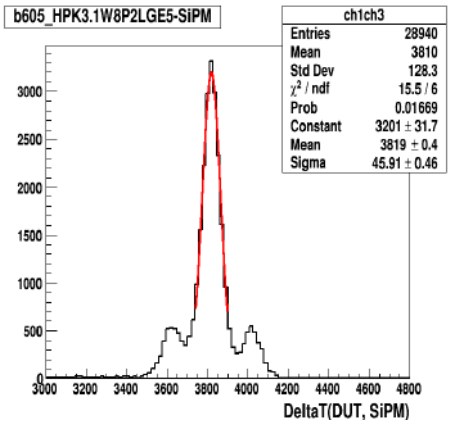

(b) Time difference of device DUT and SiPM

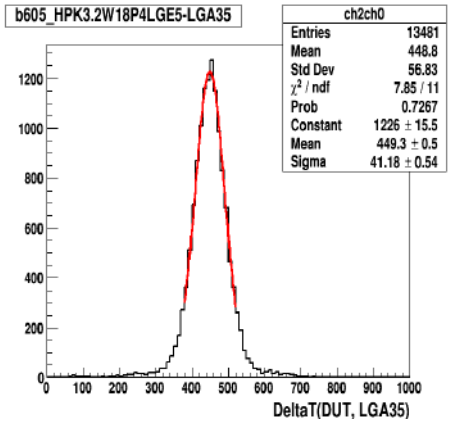

(c) Time difference of device DUT and LGA35

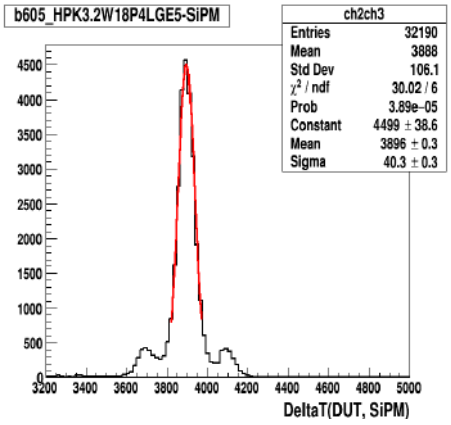

(d) Time difference of device DUT and SiPM

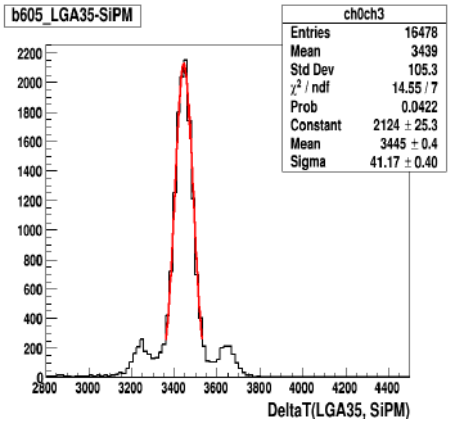

(e) Time difference of device LGA35 and SiPM

Figure G.9: Time difference of the devices fitted with gaussian function for batch 605, at different channels.

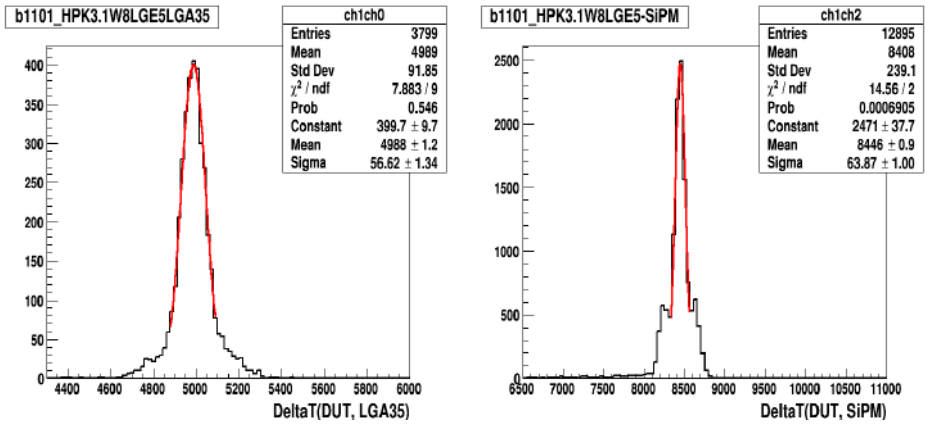

(a) Time difference of device DUT and LGA35

(b) Time difference of device DUT and SiPM

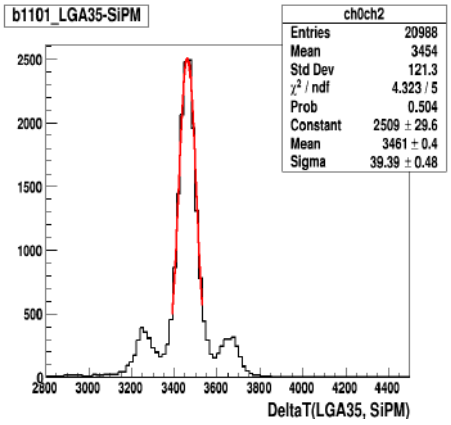

(c) Time difference of device LGA35 and SiPM

Figure G.10: Time difference of the devices fitted with gaussian function for batch 1101, at different channels.

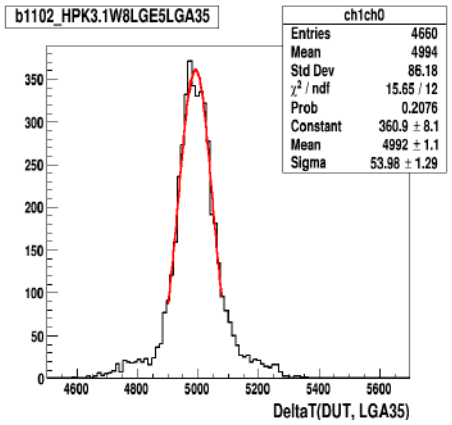

(a) Time difference of device DUT and LGA35

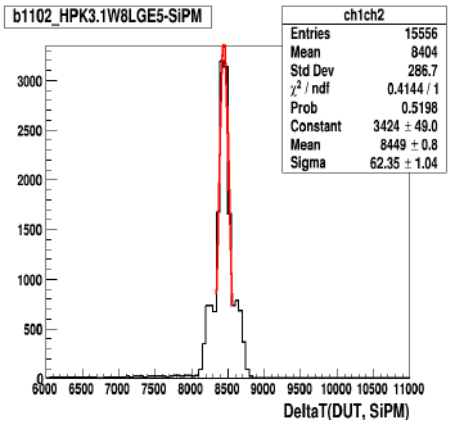

(b) Time difference of device DUT and SiPM

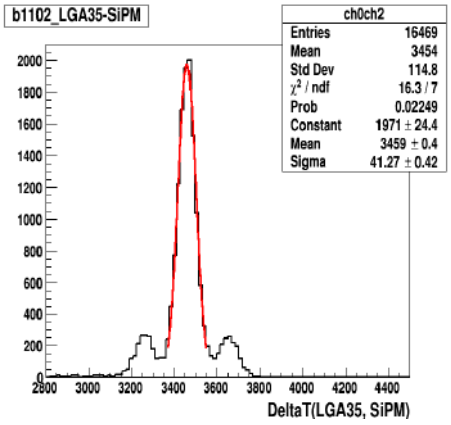

(c) Time difference of device LGA35 and SiPM

Figure G.11: Time difference of the devices fitted with gaussian function for batch 1102, at different channels.

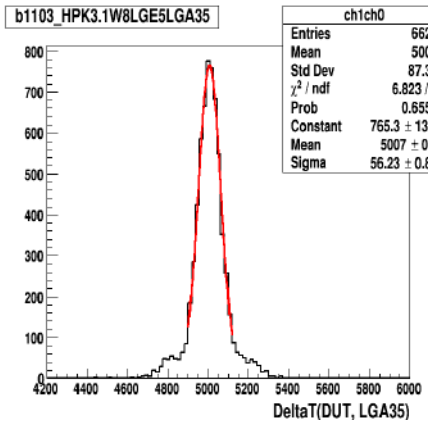

(a) Time difference of device DUT and LGA35

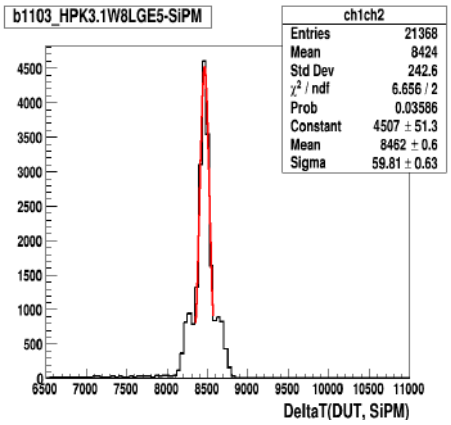

(b) Time difference of device DUT and SiPM

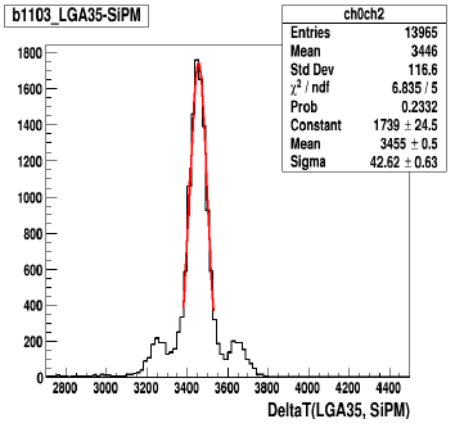

(c) Time difference of device LGA35 and SiPM

Figure G.12: Time difference of the devices fitted with gaussian function for batch 1103, at different channels.

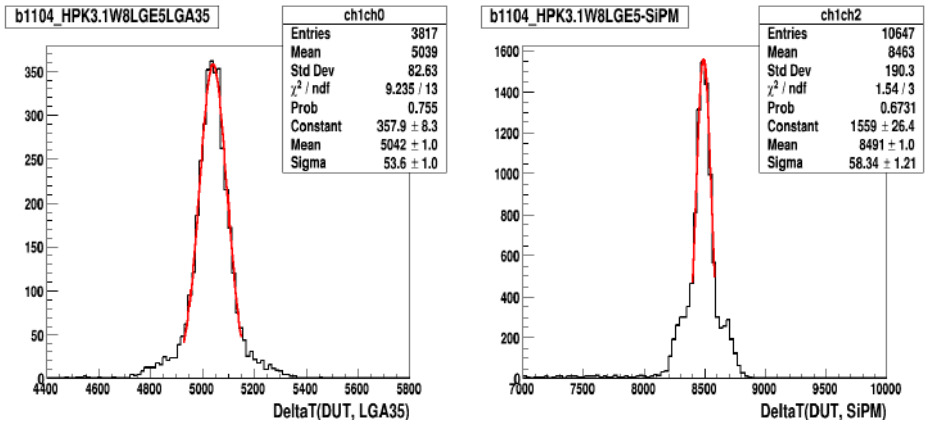

(a) Time difference of device DUT and LGA35

(b) Time difference of device DUT and SiPM

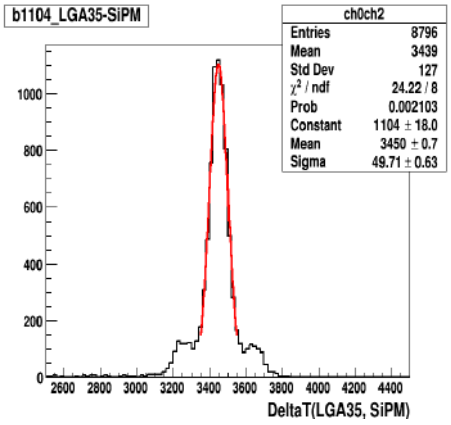

(c) Time difference of device LGA35 and SiPM

Figure G.13: Time difference of the devices fitted with gaussian function for batch 1104, at different channels.

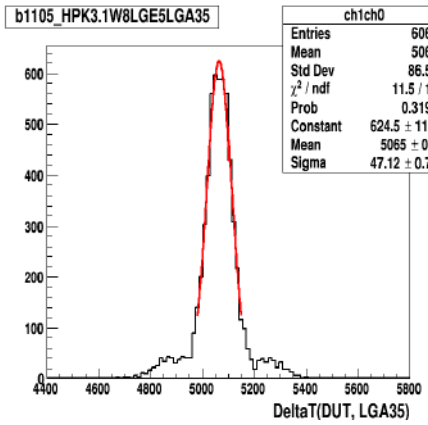

(a) Time difference of device DUT and LGA35

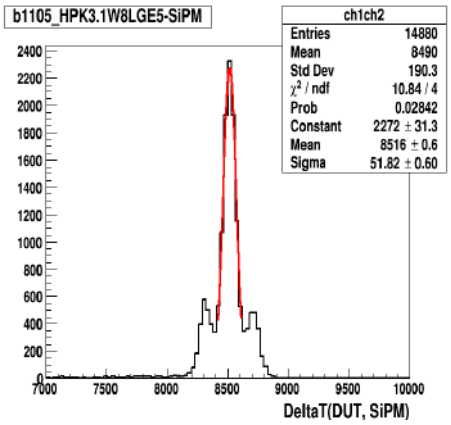

(b) Time difference of device DUT and SiPM

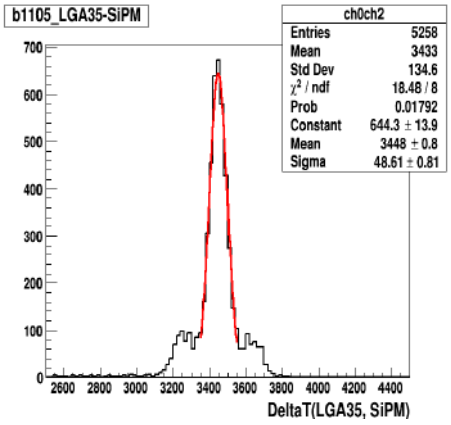

(c) Time difference of device LGA35 and SiPM

Figure G.14: Time difference of the devices fitted with gaussian function for batch 1105, at different channels.

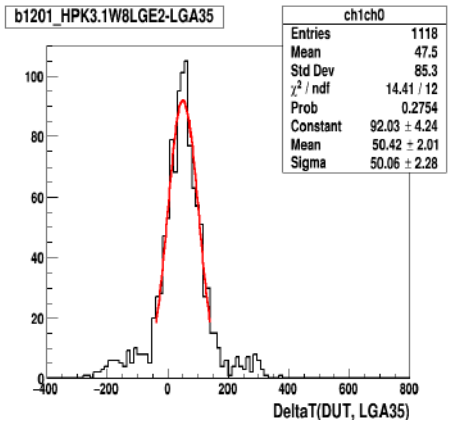

(a) Time difference of device DUT and LGA35

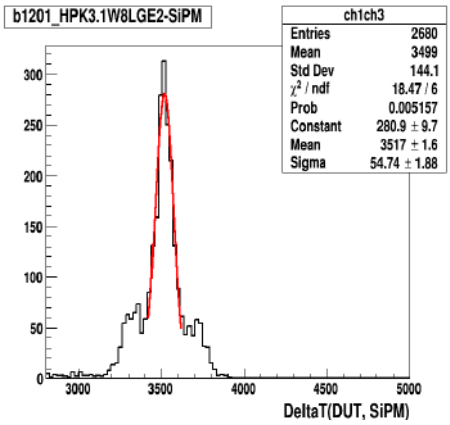

(b) Time difference of device DUT and SiPM

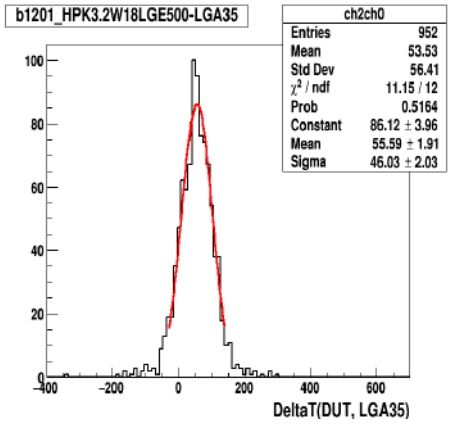

(c) Time difference of device DUT and LGA35

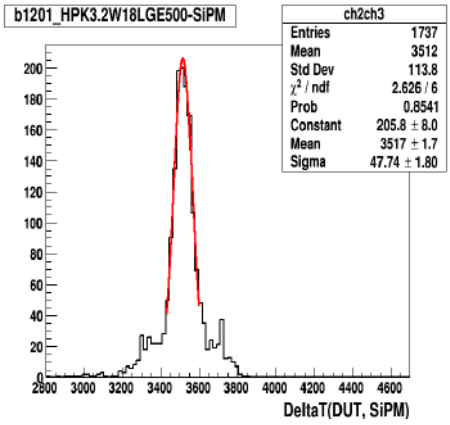

(d) Time difference of device DUT and SiPM

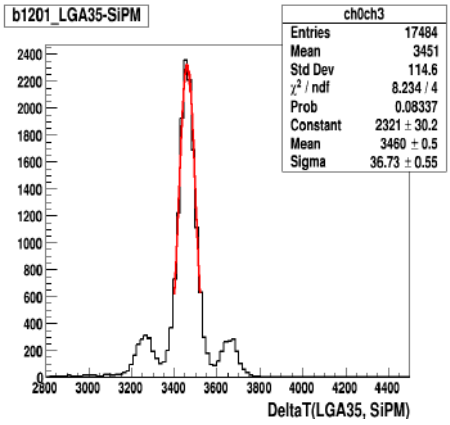

(e) Time difference of device LGA35 and SiPM

Figure G.15: Time difference of the devices fitted with gaussian function for batch 1201, at different channels.

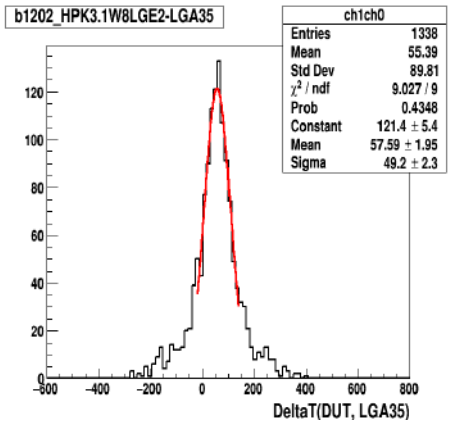

(a) Time difference of device DUT and LGA35

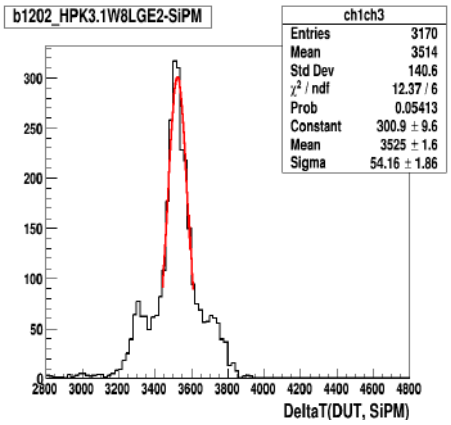

(b) Time difference of device DUT and SiPM

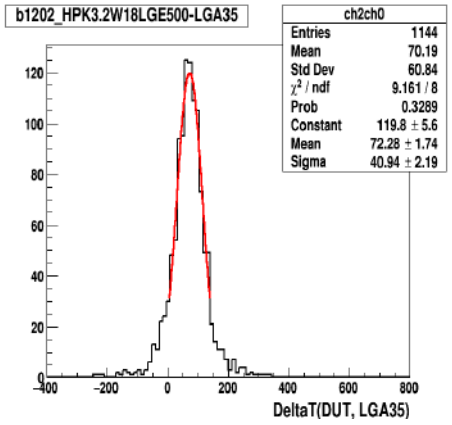

(c) Time difference of device DUT and LGA35

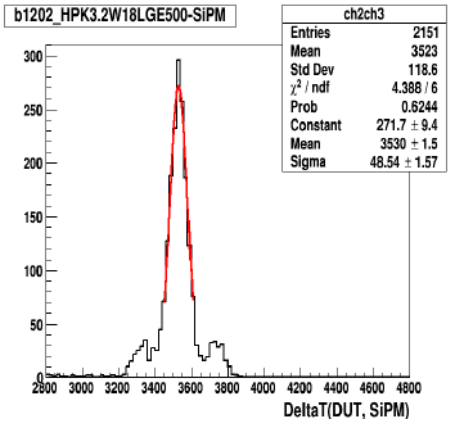

(d) Time difference of device DUT and SiPM

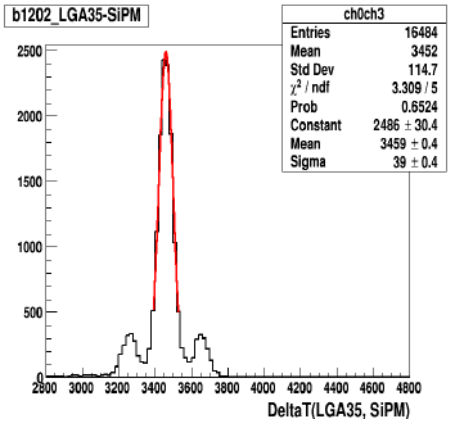

(e) Time difference of device LGA35 and SiPM

Figure G.16: Time difference of the devices fitted with gaussian function for batch 1202, at different channels.

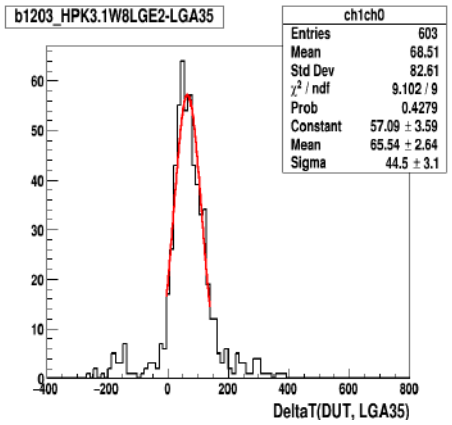

(a) Time difference of device DUT and LGA35

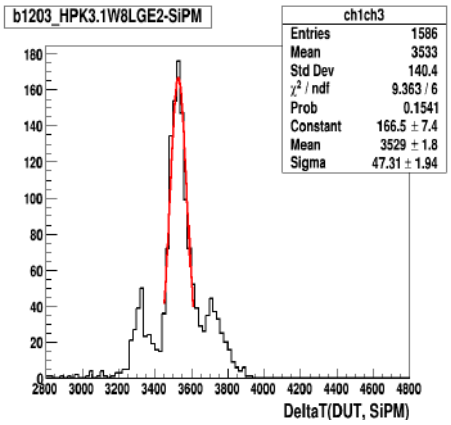

(b) Time difference of device DUT and SiPM

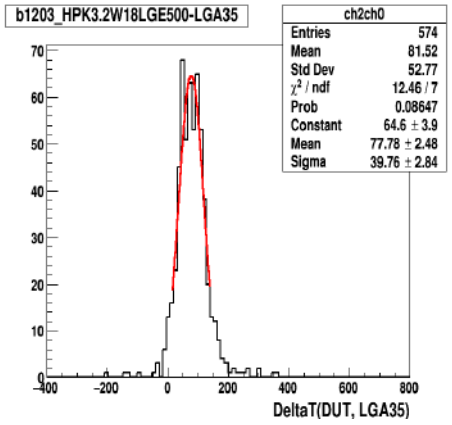

(c) Time difference of device DUT and LGA35

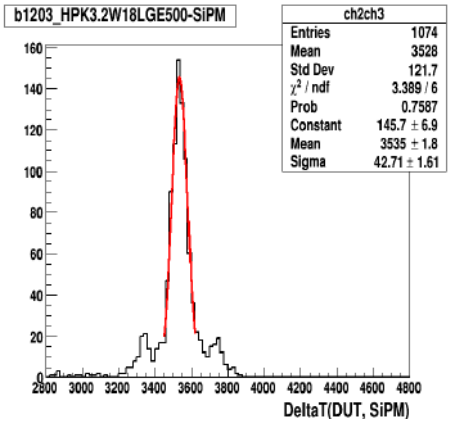

(d) Time difference of device DUT and SiPM

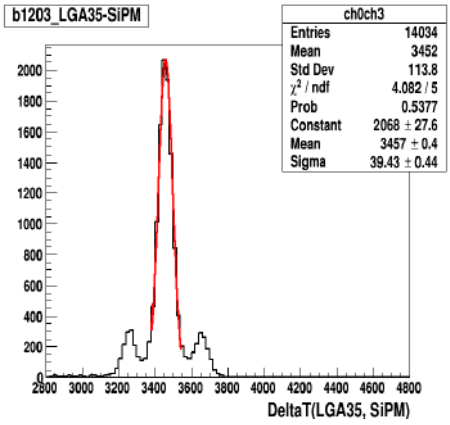

(e) Time difference of device LGA35 and SiPM

Figure G.17: Time difference of the devices fitted with gaussian function for batch 1203, at different channels.

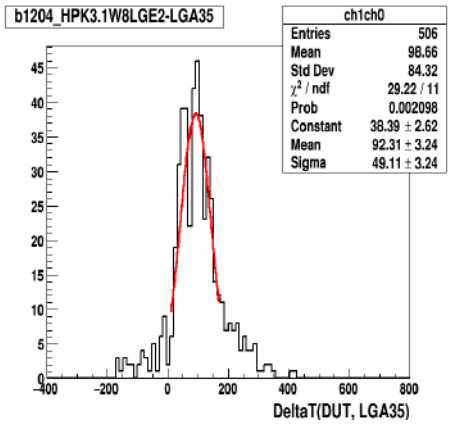

(a) Time difference of device DUT and LGA35

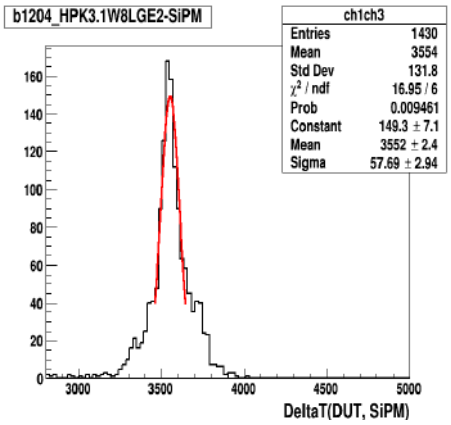

(b) Time difference of device DUT and SiPM

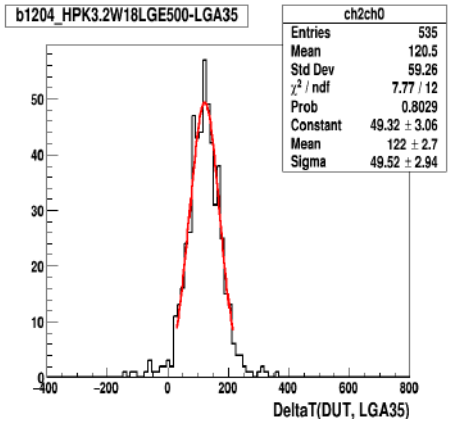

(c) Time difference of device DUT and LGA35

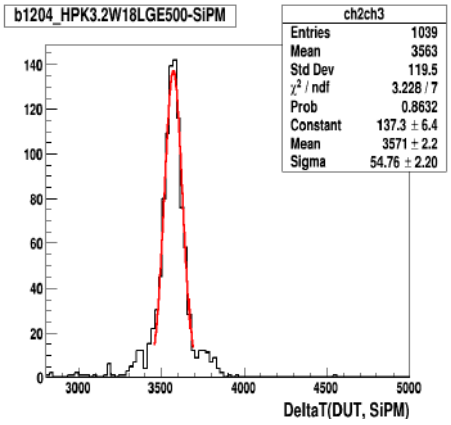

(d) Time difference of device DUT and SiPM

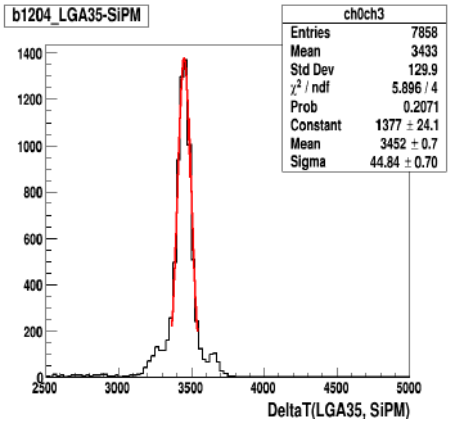

(e) Time difference of device LGA35 and SiPM

Figure G.18: Time difference of the devices fitted with gaussian function for batch 1204, at different channels.

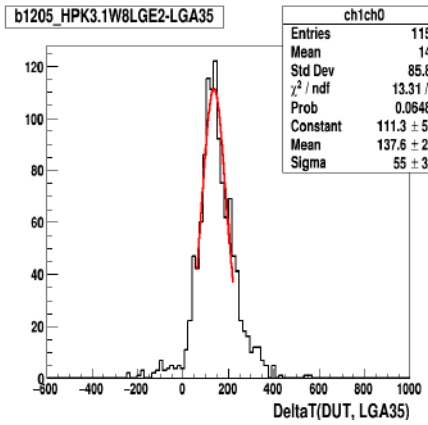

(a) Time difference of device DUT and LGA35

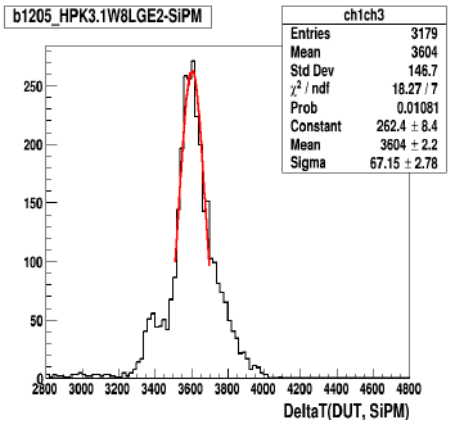

(b) Time difference of device DUT and SiPM

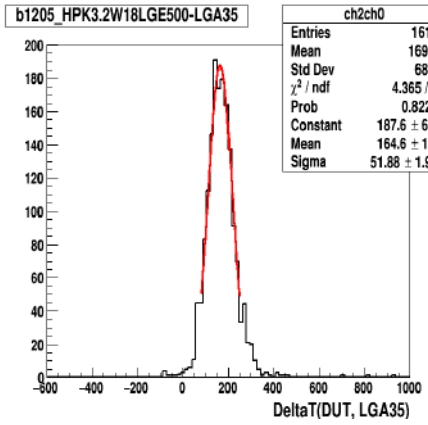

(c) Time difference of device DUT and LGA35

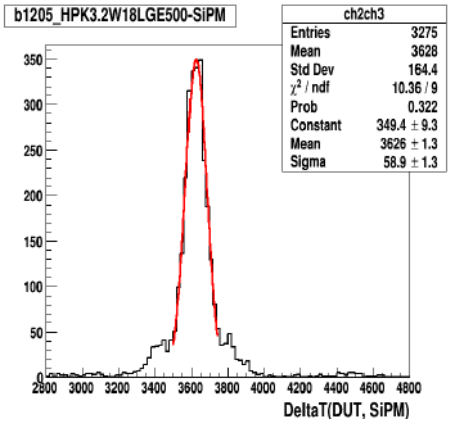

(d) Time difference of device DUT and SiPM

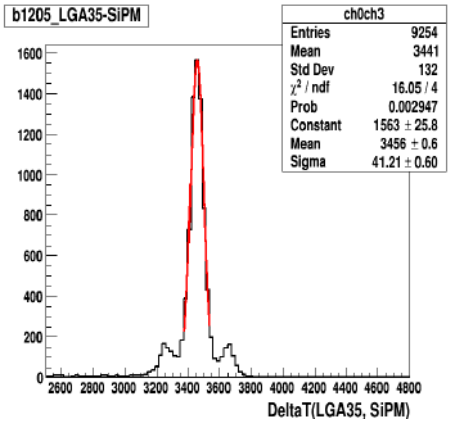

(e) Time difference of device LGA35 and SiPM

Figure G.19: Time difference of the devices fitted with gaussian function for batch 1205, at different channels.

Bibliography

[1] ATLAS Collaboration. Technical proposal: A high-granularity timing detector for the atlas phase-ii upgrade. Technical report, **2018**.

[2] Tom WB Kibble. The standard model of particle physics. arXiv preprint arXiv:1412.4094, **2014**.

[3] Federico Roncarolo. Accuracy of the transverse emittance measurements of the CERN Large Hadron Collider. PhD thesis, Milan Polytechnic, **2005**.

[4] R Alemany, C Burrage, H Bartosik, J Bernhard, J Boyd, M Brugger, M Calviani, C Carli, N Charitonidis, D Curtin, et al. Summary report of physics beyond colliders at cern. arXiv preprint arXiv:1902.00260, 2019.

[5] Robert Graham Reed et al. The upgrade of the atlas tile calorimeter readout electronics for phase ii. In Journal of Physics: Conference Series, volume 623, page 012024. IOP Publishing, **2015**.

[6] ATLAS Collaboration. Technical design report for the phase-ii upgrade of the atlas tdaq system. Technical report, **2017**.

[7] Giorgio Apollinari, I Béjar Alonso, Oliver Brüning, M Lamont, and Lucio Rossi. High-luminosity large hadron collider (hl-lhc): Preliminary design report. Technical report, Fermi National Accelerator Lab.(FNAL), Batavia, IL (United States), **2015**.

[8] C Nellist. Achievements of the atlas upgrade planar pixel sensors r&d project. Journal of Instrumentation, 10(01):C01027, **2015**.

[9] M Carulla et al. First 50 μm thick lgad fabrication at cnm. In 28th RD50 Workshop, Torino, June 7th, **2016**.

[10] Brian R Martin and Graham Shaw. Nuclear and particle physics: an introduction. John Wiley & Sons, **2019**.

[11] Georges Aad, JM Butterworth, J Thion, U Bratzler, PN Ratoff, RB Nickerson, JM Seixas, I Grabowska-Bold, F Meisel, S Lokwitz, et al. The atlas experiment at the cern large hadron collider. Jinst, 3:S08003, **2008**.

[12] François Englert and Peter W Higgs. The nobel prize in physics 2013. In spin, volume 1, page 2, **2013**.

[13] Giorgio Apollinari, O Brüning, Tatsushi Nakamoto, and Lucio Rossi. High luminosity large hadron collider hl-lhc. arXiv preprint arXiv:1705.08830, **2017**.

[14] Morad Aaboud, Georges Aad, Brad Abbott, Jalal Abdallah, B Abeloos, SH Abidi, OS AbouZeid, NL Abraham, H Abramowicz, H Abreu, et al. Identification and rejection of pile-up jets at high pseudorapidity with the atlas detector. The European Physical Journal C, 77(9):580, **2017**.

[15] Hartmut FW Sadrozinski, Abraham Seiden, Nicolò Cartiglia, J Weingarten, S Altenheiner, and M Beimforde. Beam test measurements of low gain avalanche detector single pads and arrays for the atlas high granularity timing detector.

[16] Kei-Ichi Kondo. Gauge-independent brout–englert–higgs mechanism and yang–mills theory with a gauge-invariant gluon mass term. The European Physical Journal C, 78(7):577, **2018**.

[17] Szymon Gadomski. Atlas inner detector performance. Nuclear Instruments and Methods in Physics Research Section A: Accelerators, Spectrometers, Detectors and Associated Equipment, 462(1-2):285–290, **2001**.

[18] Krisztian Peters. Higgs boson production at the lhc. Technical report, ATL-COM-PHYS-2015-1248, **2015**.

[19] Corentin Allaire et al. A high-granularity timing detector in atlas: Performance at the hl-lhc. Nuclear Instruments and Methods in Physics Research Section A: Accelerators, Spectrometers, Detectors and Associated Equipment, 924:355–359, **2019**.

[20] ATLAS Collaboration et al. G. aad, et al., the atlas experiment at the cern large hadron collider. Journal of Instrumentation, **3**(08):S08003.

[21] Serguei Chatrchyan, G Hmayakyan, V Khachatryan, CMS Collaboration, et al. The cms experiment at the cern lhc. Journal of instrumentation, 3(8):S08004, **2008**.

[22] A Augusto Alves Jr, LM Andrade Filho, AF Barbosa, I Bediaga, G Cernicchiaro, G Guerrer, HP Lima Jr, AA Machado, J Magnin, F Marujo, et al. The lhcb detector at the lhc. Journal of instrumentation, 3(08):S08005, **2008**.

[23] Kenneth Aamodt, A Abrahantes Quintana, R Achenbach, S Acounis, D Adamová, C Adler, M Aggarwal, F Agnese, G Aglieri Rinella, Z Ahammed, et al. The alice experiment at the cern lhc. Journal of Instrumentation, 3(08):S08002, **2008**.

[24] LHCf Collaboration. O. adriani et al. the lhcf detector at the cern large hadron collider. jinst, 3 (s08006), 2008.

[25] Giuseppe Latino. The totem experiment at lhc. arXiv preprint arXiv:0805.3968, **2008**.

[26] Bobby Acharya, J Alexandre, J Bernabéu, M Campbell, S Cecchini, J Chwastowski, M De Montigny, D Derendarz, A De Roeck, JR Ellis, et al. The physics programme of the moedal experiment at the lhc. International Journal of Modern Physics A, 29(23):1430050, **2014**.

[27] Georges Aad, B Abbott, J Abdallah, AA Abdelalim, Abdelmalek Abdesselam, B Abi, M Abolins, H Abramowicz, H Abreu, BS Acharya, et al. The atlas inner detector commissioning and calibration. The European Physical Journal C, 70(3):787–821, **2010**.

[28] M Capeans, T Flick, R Vuillermet, G Darbo, H Pernegger, K Einsweiller, M Garcia-Sciveres, M Elsing, O Rohne, and C Gemme. Atlas insertable b-layer technical design report. Technical report, ATLAS-TDR-019, **2010**.

[29] M Aharrouche, J Colas, L Di Ciaccio, M El Kacimi, O Gaumer, M Gouanere, D Goujdami, R Lafaye, S Laplace, C Le Maner, et al. Response uniformity of the atlas liquid argon electromagnetic calorimeter. Nuclear Instruments and Methods in Physics Research Section A: Accelerators, Spectrometers, Detectors and Associated Equipment, 582(2):429–455, **2007**.

[30] Atlas Collaboration et al. ATLAS tile calorimeter: Technical design report. CERN, **1996**.

[31] Georges Aad et al. Atlas muon spectrometer: Technical design report. Technical Design Report ATLAS, CERN, Geneva, **1997**.

[32] HJ Herman. The superconducting magnet system for the atlas detector at cern. IEEE transactions on applied superconductivity, 10(1):347–352, **2000**.

[33] Rende Steerenberg. Lhc report: Protons: mission accomplished. **2018**.

[34] Stéphane Fartoukh. Pile up management at the high-luminosity lhc and introduction to the crab-kissing concept. Physical Review Special Topics-Accelerators and Beams, 17(11):111001, **2014**.

[35] Corentin Allaire. A high-granularity timing detector (hgtd) in atlas: Performance at the hl-lhc. Technical report, ATL-COM-LARG-2018-003, **2018**.

[36] C Allaire, J Benitez, M Bomben, G Calderini, M Carulla, E Cavallaro, A Falou, D Flores, P Freeman, Z Galloway, et al. Beam test measurements of low gain avalanche detector single pads and arrays for the atlas high granularity timing detector. Journal of Instrumentation, 13(06):P06017, **2018**.

[37] Charles Kittel, Paul McEuen, and Paul McEuen. Introduction to solid state physics, volume 8. Wiley New York, **1996**.

[38] Hartmut FW Sadrozinski, Abraham Seiden, and Nicolò Cartiglia. 4d tracking with ultra-fast silicon detectors. Reports on Progress in Physics, 81(2):026101, **2017**.

[39] G Kramberger, M Carulla, E Cavallaro, V Cindro, D Flores, Z Galloway, S Grinstein, S Hidalgo, V Fadeyev, J Lange, et al. Radiation hardness of thin low gain avalanche detectors. Nuclear Instruments and Methods in Physics Research Section A: Accelerators, Spectrometers, Detectors and Associated Equipment, 891:68–77, **2018**.

[40] Mei-Li Holmberg. Studies of low gain avalanche detector prototype sensors for the atlas high-granularity timing detector, **2019**.

[41] Ralf Diener, Jan Dreyling-Eschweiler, Heiko Ehrlichmann, Ingrid-Maria Gregor, Ulrich Kötz, Uwe Krämer, Norbert Meyners, Natalia Potylitsina-Kube, Anne Schütz, Paul Schütze, et al. The desy ii test beam facility. Nuclear Instruments and Methods in Physics Research Section A: Accelerators, Spectrometers, Detectors and Associated Equipment, 922:265–286, **2019**.

[42] Erika Garutti. Silicon photomultipliers for high energy physics detectors. Journal of Instrumentation, 6(10):C10003, **2011**.

[43] M Carulla, A Doblas, D Flores, Z Galloway, S Hidalgo, G Kramberger, Z Luce, I Mandic, S Mazza, A Merlos, et al. 50μm thin low gain avalanche detectors (lgad) for timing applications. Nuclear Instruments and Methods in Physics Research Section A: Accelerators,

Spectrometers, Detectors and Associated Equipment, 924:373–379, **2019**.

[44] S Xiao, S Alderweireldt, S Ali, C Allaire, C Agapopoulou, N Atanov, MK Ayoub, G Barone, D Benchekroun, A Buzatu, et al. Beam test results of ihep-ndl low gain avalanche detectors (lgad). arXiv preprint arXiv:2005.07323, **2020**.